EVALUATION OF NONINVASIVE GEOPHYSICAL TECHNIQUES TO IMAGE THE PORTUGUESE BEND LANDSLIDE IN RANCHO PALOS VERDES, CALIFORNIA

A Thesis

Presented to the

Faculty of

California State Polytechnic University, Pomona

In Partial Fulfillment

Of the Requirements for the Degree

Master of Science

In

Geology

By

Steven G. Moody

2021

SIGNATURE PAGE

THESIS: EVALUATION OF NONINVASIVE GEOPHYSICAL TECHNIQUES TO IMAGE THE PORTUGUESE BEND LANDSLIDE IN RANCHO PALOS VERDES, CALIFORNIA

AUTHOR: Steven G. Moody

DATE SUBMITTED: Spring 2021

Department of Geological Sciences

Dr. Jascha Polet
Thesis Committee Chair
Geological Sciences

Dr. Jonathan A. Nourse
Geological Sciences

Dr. Stephen G. Osborn
Geological Sciences

ACKNOWLEDGMENTS

This project would not have been possible without the input, advice, and support from a substantial number of excellent individuals. Firstly, I would like to thank Dr. Jascha Polet for her guidance, assistance, and seemingly endless patience in dealing with my idiosyncrasies and long duration on this project. I'd like to thank both my grandmothers, one of whom was unable to see this undertaking completed, for their love, patience, and the offering of their hospitality to me while I was away from home. I'd like to thank my friends and family for pushing me to continue this to completion. Specifically, I want to thank my mother and father for their eternal support and willingness to jump into the mix, assist me with field excursions, and help with anything else related to this project. Without their help, this project would have not been possible.

Special thanks also to Samuel Badillo, Jennifer Pfau, Peter Flores, Charles Dang, and Jacob Palmer for assisting with the first wave of equipment deployments and strategy planning. Thank you to the Spring 2019 Advanced Subsurface Geophysics class for their assistance with data collection and total station deployment. Thanks to Anisha Tyagi for her tips on organizing and processing the H/V data in Geopsy and Excel. Thanks to all of the other graduate and undergraduate students with whom I was able to discuss my material. The time spent with all of you has been a bright point in my life and will remain so for as long as I live.

ABSTRACT

The Portuguese Bend Landslide (PBL) is examined with multiple noninvasive geophysical experiments. Gravity, Ground Penetrating Radar (GPR), ground based magnetometry, and Horizontal/Vertical Spectral Ratio (HVSR) surveys were carried out on the slide to image the internal structure of the slide and potentially determine the geometry of and depth to the sliding surface, as well as seasonal fluctuations in the presence of groundwater. Prior work on this site has shown that the sliding surface is found within the Altamira Shale unit of the Monterey Formation and is coated by a layer of bentonite clay derived from tuffaceous volcanic material forming a zone with significant hydrologic impermeability. Depths to the sliding surface are determined from HVSR peak frequency measurements and were found to range between 2.7 and 53.1 meters. Peak frequencies recorded after rainfall were typically higher than those recorded during the dry season potentially as a result of ponding water on the sliding surface. The sliding surface geometry, as estimated from the HVSR peak frequencies, was found to be highly undulatory. Gravity profiles showed variation across the field site with a 27 milligal range along Palos Verdes Drive South and a 1.6 milligal range to the north, at the top of the active slide. The southern line detected the western edge of the slide. Measured total magnetic intensity varied significantly across all individual surveys and across the field site as a whole and appears to be correlative to slide thickness. GPR profiles surveyed with a 400 MHz antenna did not reveal significant features of interest and its usefulness on this field site is likely limited due to high soil water content and difficulty in consistently coupling the unit uniformly with the ground. This study illustrates the potential of gravity, magnetometry, and especially HVSR methods to image landslides in ecologically delicate areas.

TABLE OF CONTENTS

LIST OF TABLES

LIST OF FIGURES

1. INTRODUCTION:

In this thesis we show the results of a pilot study of multiple noninvasive geophysical approaches at the Portuguese Bend Landslide (PBL). The following research objectives were addressed: determine the suitability of the various methods at this site, locate the slide boundaries, determine the sliding interface depth, locate possible subsurface igneous bodies, determine the character of the sliding surface geometry, determine the location and influence of subsurface water and how this varies depending on seasonal rainfall.

Along the coastline of California, numerous landslides impact communities by damaging homes and other property, disrupting travel and commerce by undermining or destroying infrastructure, and causing loss of life during rapid mass movement events. A map of the Palos Verdes Peninsula relative to the rest of California is displayed in Figure 1.1. Geophysical methods can be utilized to image these landslides and provide valuable

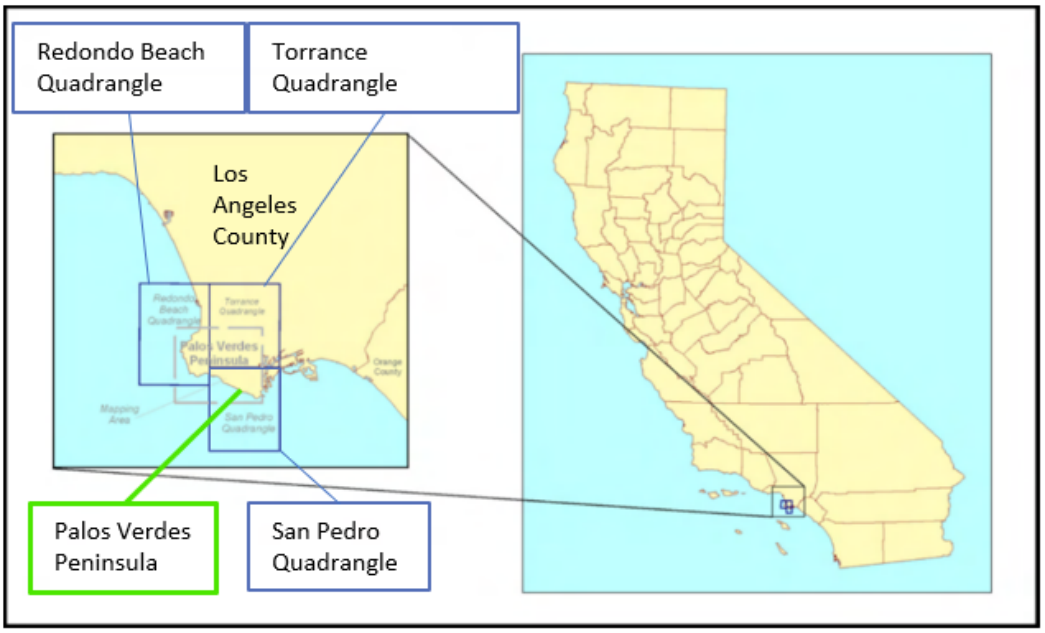

Figure 1.1. Geographic overview map displaying the location of the Palos Verdes Peninsula relative to the rest of California. The Portuguese Bend Landslide is located within the San Pedro Quadrangle as is shown in the left section of the figure. Modified from Haydon 2007.

insight into their physical properties. Such results can then be applied by engineers and public agencies to mitigate the hazard presented by these phenomena. The Portuguese Bend Landslide located in Rancho Palos Verdes has already impacted the community in many of the aforementioned ways. Since geophysical methods have not been applied on this field site in the past, this work is a pilot study on this slide. The landslide's divisions and its current extent as mapped by the California Geological Society are illustrated in Figure 1.2.

1.1. Geologic History and Tectonic Setting:

The development of the Palos Verdes Hills was initiated following the termination of subduction and the subsequent shift to transform motion along generally north-south trending faults, such as the San Andreas Fault, approximately 20 million years ago

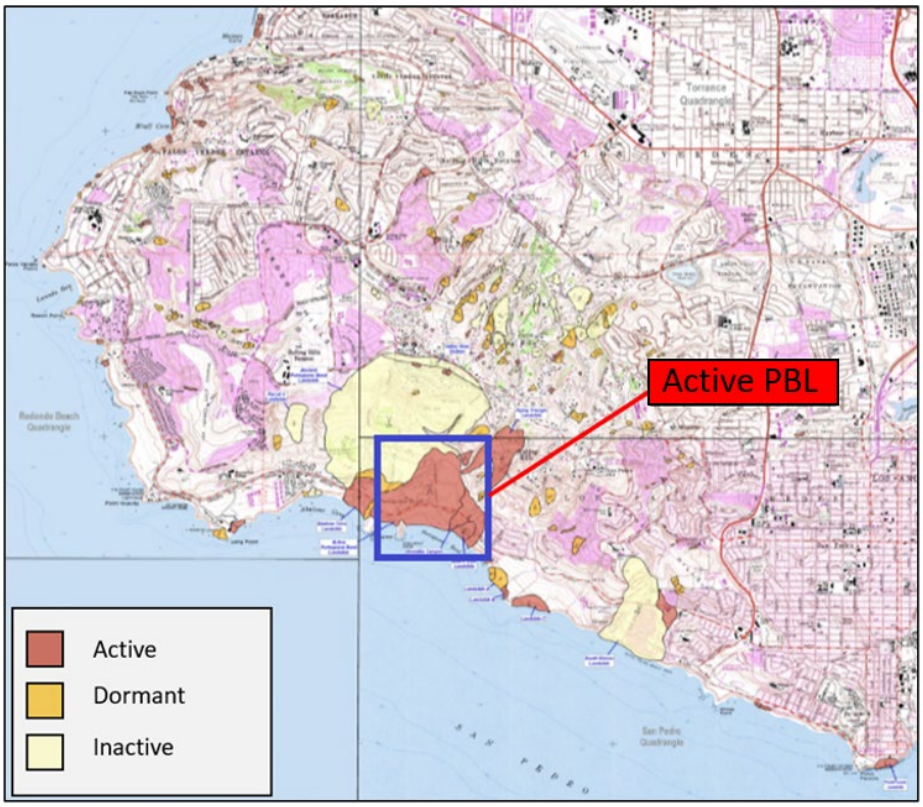

Figure 1.2. Extent of the PBL complex and other landslide complexes. The blue rectangle encompasses the active PBL and field site in addition to the Klondike Canyon and Beach Club Landslides that were not studied in this project. Active landslides are colored red, dormant sections are orange, and inactive sections are cream-colored. Adapted from Haydon 2007.

(Atwater 1970). Newly activated faulting driven by the shift in tectonic regime led to a variety of new features that would later determine the location and behavior of landslides in the Palos Verdes Hills and on the Palos Verdes Peninsula. Crustal extension provides a likely mechanism by which the Catalina schist was brought to the surface and into contact with the submarine material that would form the Altamira Shale during the Middle Miocene, possibly as a result of faulting action. The Newport-Inglewood, Cabrillo, and Palos Verdes Reverse Faults in this area likely contributed to the uplift and shape of the Palos Verdes Hills (Bryant 1987). Additionally, the PBL is contained within a seaward-dipping syncline, a structure that is part of a larger anticline complex built primarily by fault action along the Palos Verdes Fault (Bryant 1987). Although certain sections of the Catalina Schist were fully unroofed and provided material for some thin beds of sandstone, the majority of the schist underlies the Monterey Formation. Stratigraphic columns are displayed in Figure 1.3 and more generalized stratigraphic columns and rock descriptions are shown in Figure 1.4. A geologic map illustrating these units is shown in Figure 1.5. Following the deposition of the Altamira Shale during a period of subaqueous volcanism 16-14 million years ago, a period of relative depositional quiescence followed. A higher resolution map of the geologic units on the Palos Verdes Peninsula as mapped by Ehlig are displayed in Figure 1.6. This period is marked by the placement of the Valmonte Diatomite. Minimal nonbiogenic sediment exists in this section (Conrad and Ehlig 1987). Approximated structural relationships at this location between units are exhibited on ageologic map and in cross section form in Figure 1.7. The last sequential section of interest in this area is the Malaga Mudstone, which is composed of inorganic muds and gravel lenses. Deposition of these units ended approximately 4 million years ago (Conrad and

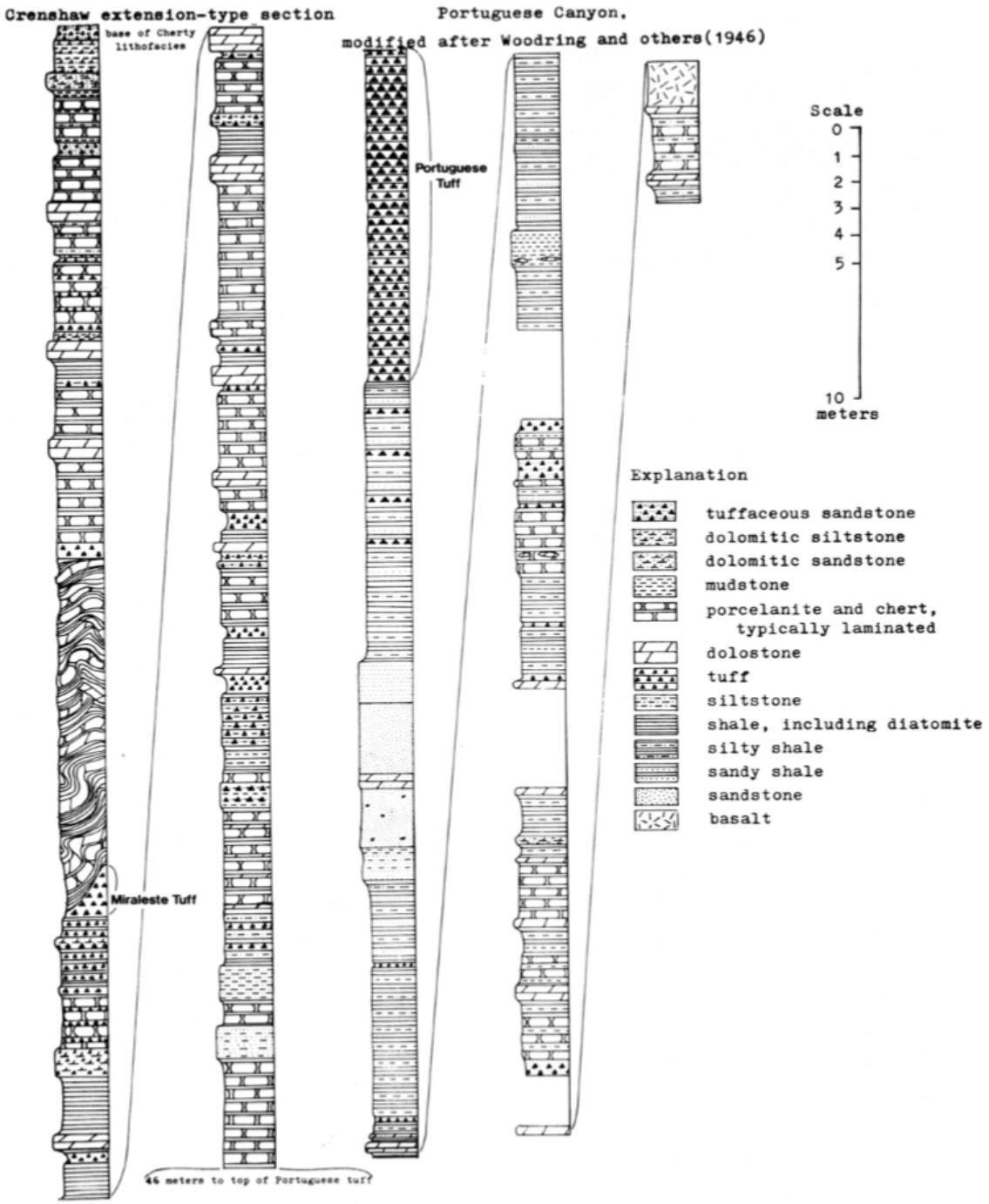

Figure 1.3. Lithographic sections showing the varied units found nearby and on the field site. The sections exhibited primarily include sedimentary rocks with uncommon basalt. Adapted from Conrad and Ehlig 1987.

Ehlig 1987). Of these component sections, the Altamira Shale and the Valmonte Diatomite are common in the study area, and sliding occurs as a result of the fissility and weakness

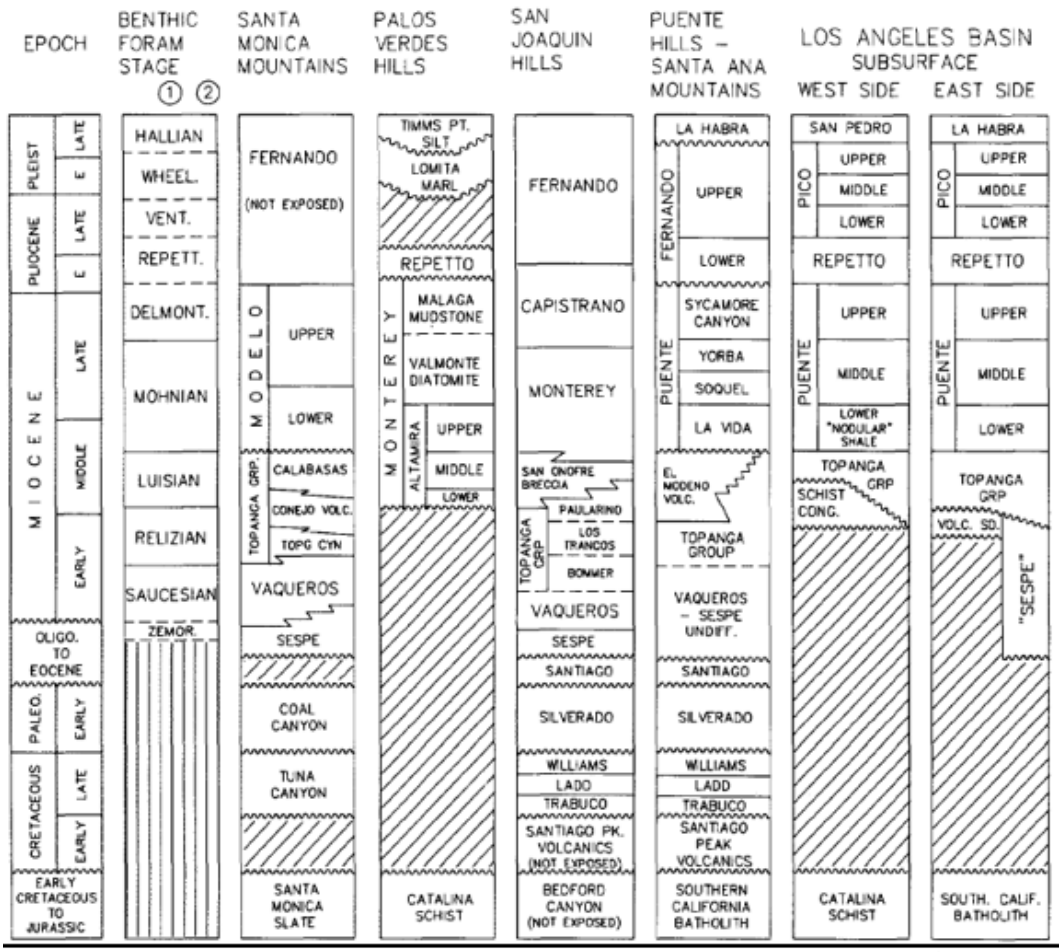

PALOS VERDES HILLS

Formation			Age	Thickness	Lithology	Environment
Timms Pt Silt			Late Pleistocene	120 ft (37 m)	Massive sandy silt and silty sand	Inner neritic
Lomita Marl			Late Pleistocene	100 ft (31 m)	Unconsolidated calcareous sand and marl	Outer neritic
Repetto Siltstone			Late to early Pliocene (Repettian Stage)	150 ft (46 m)	Massive, glauconitic foraminiferal siltstone with minor amounts of schist breccia and sandstone lenses	Lower bathyal
Monterey	Malaga Mudstone Member		Early Pliocene to late Miocene ("Delmontian" Stage)	330 ft (100 m)	Dark brown radiolarian mudstone and fine-grained siltstone with minor amounts of dolomite, diatomaceous shale, and laminated diatomite	Middle bathyal
	Valmonte Diatomite Member		Late Miocene (Mohnian Stage)	500 ft (152 m)	Laminated diatomite and phosphatic diatomaceous shale with minor amounts of porcelanite, chert, and dolomite	Upper to middle bathyal
	Altamira Shale Member	Upper	Late to middle Miocene (Mohnian Stage)	1400 ft (415 m)	Dominated by phosphatic shale and organic-rich shale; minor intervals of porcelaneous shale, limestone, and calcareous sandstone; interval of thick, blue glaucophane schist conglomerate sandstone and brecciated shale	Upper to middle bathyal
		Middle	Middle Miocene (Luisian Stage)		Porcelaneous shale and minor amounts of diatomaceous rocks; lesser amounts of tuffs, calcareous phosphatic siltstone, and calcareous mudstones	Upper to middle bathyal
		Lower	Middle Miocene (Luisian Stage)		Silty and sandy shales with lesser amounts of silty porcelaneous shale, porcelaneous mudstone, and tuffs	Upper to middle bathyal
Catalina Schist			Early Cretaceous to Late Jurassic	Unknown	Extensively metamorphosed schist derived from greywacke, chert, volcanics, and gabbro	Unknown

Figure 1.4. Stratigraphic sections for Los Angeles and proximal areas. Note the Palos Verdes Hills (PVH) section. The PVH section is cloned in the bottom section alongside the rock descriptions correspondent to the section. Modified from Bryant 1987.

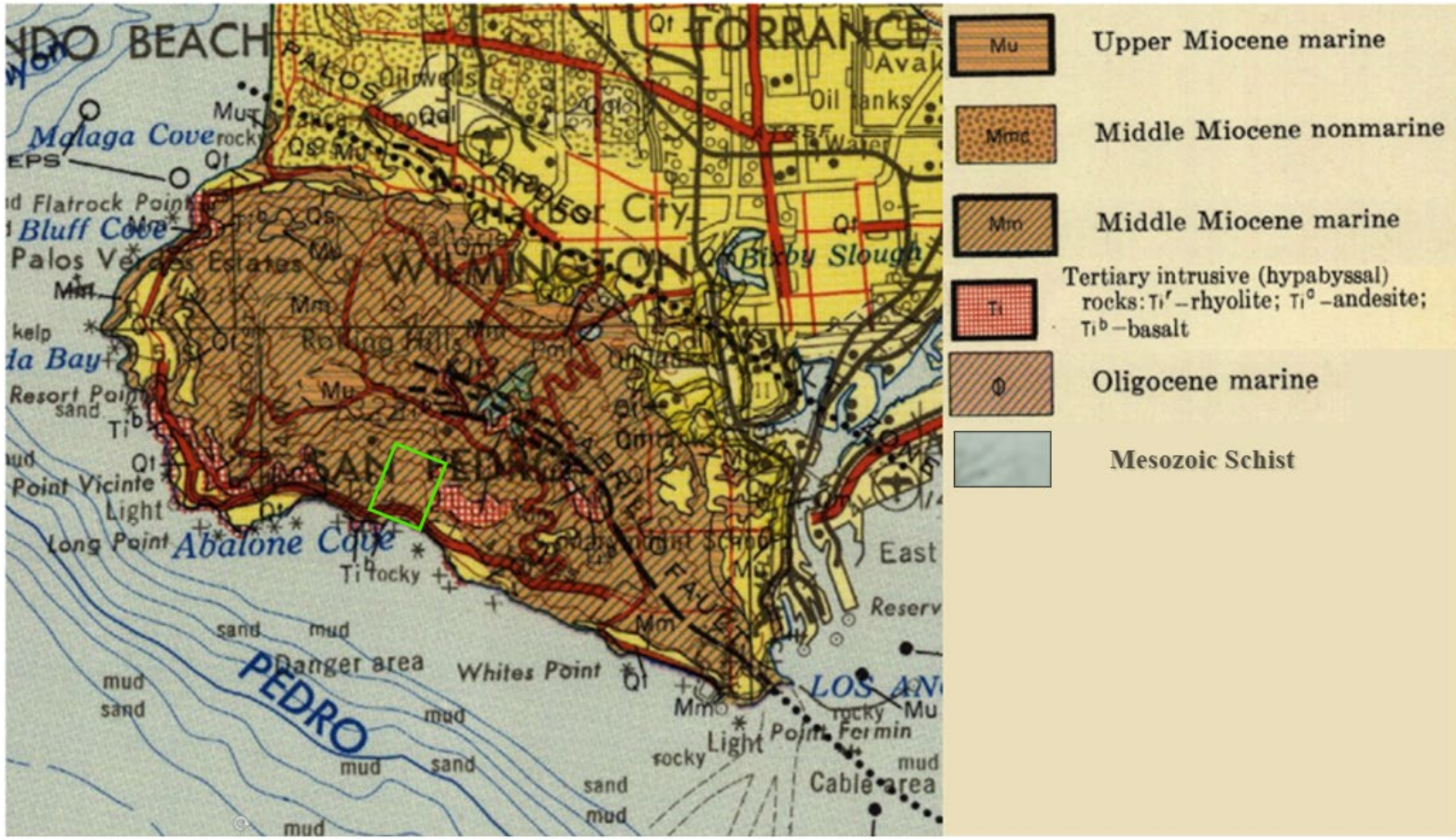

Figure 1.5. Zoomed geologic map of the San Pedro Quadrangle. The map is zoomed to focus on the Palos Verdes Peninsula. Majority of the rocks are marine sediments with some exposed schist and basalt. Basalt is closely proximal to the field area, but not mapped on the field site. The study area is contained within the green box. Modified from Jennings 1962.

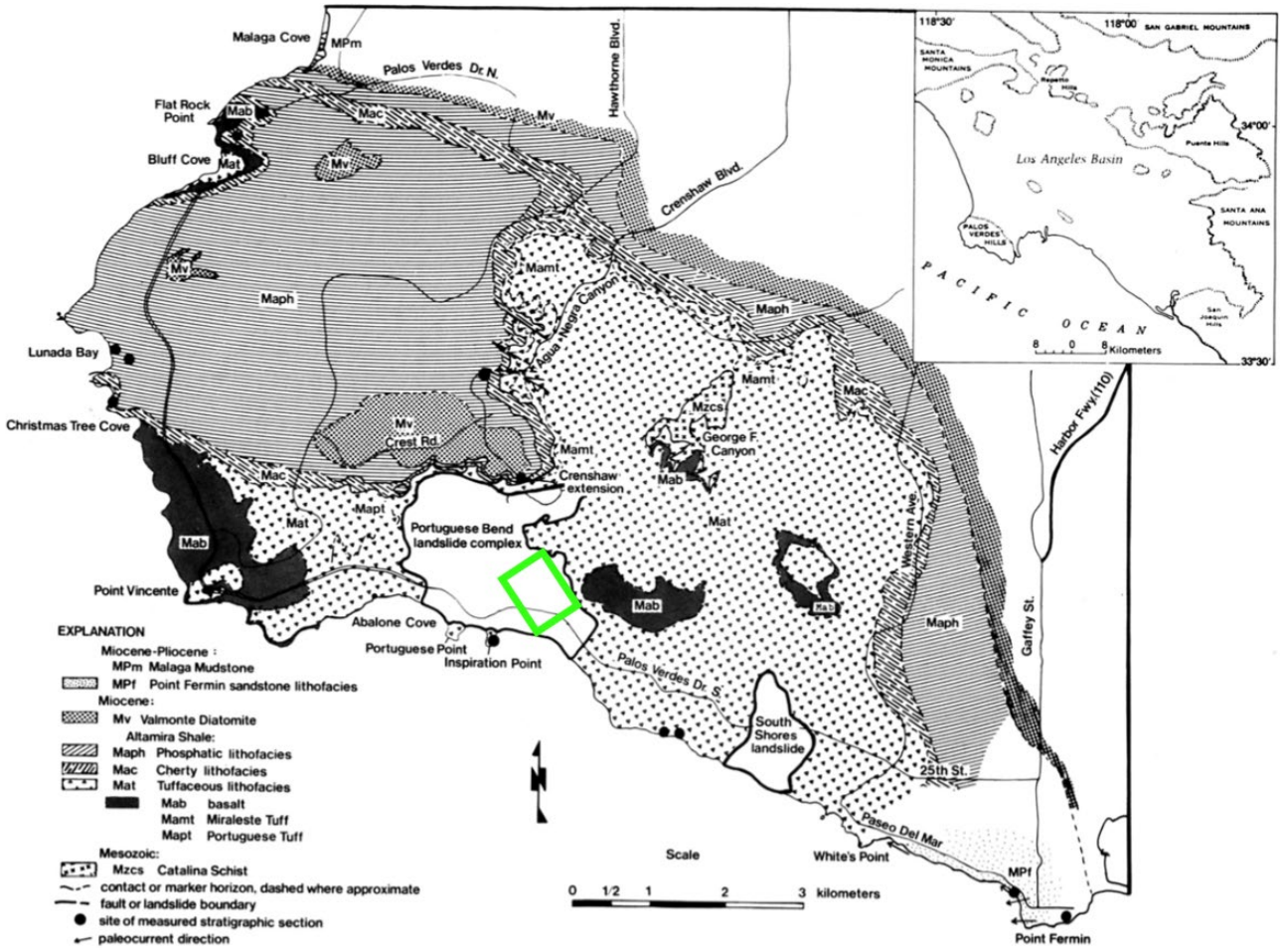

Figure 1.6. Geologic unit and lithofacies sketch map produced for the Palos Verdes Peninsula. Most units are sedimentary or tuffaceous volcanic derivatives. The field area is marked by a green rectangle. Some basalt volcanic units were mapped but not in the field area. Modified from Conrad and Ehlig 1987.

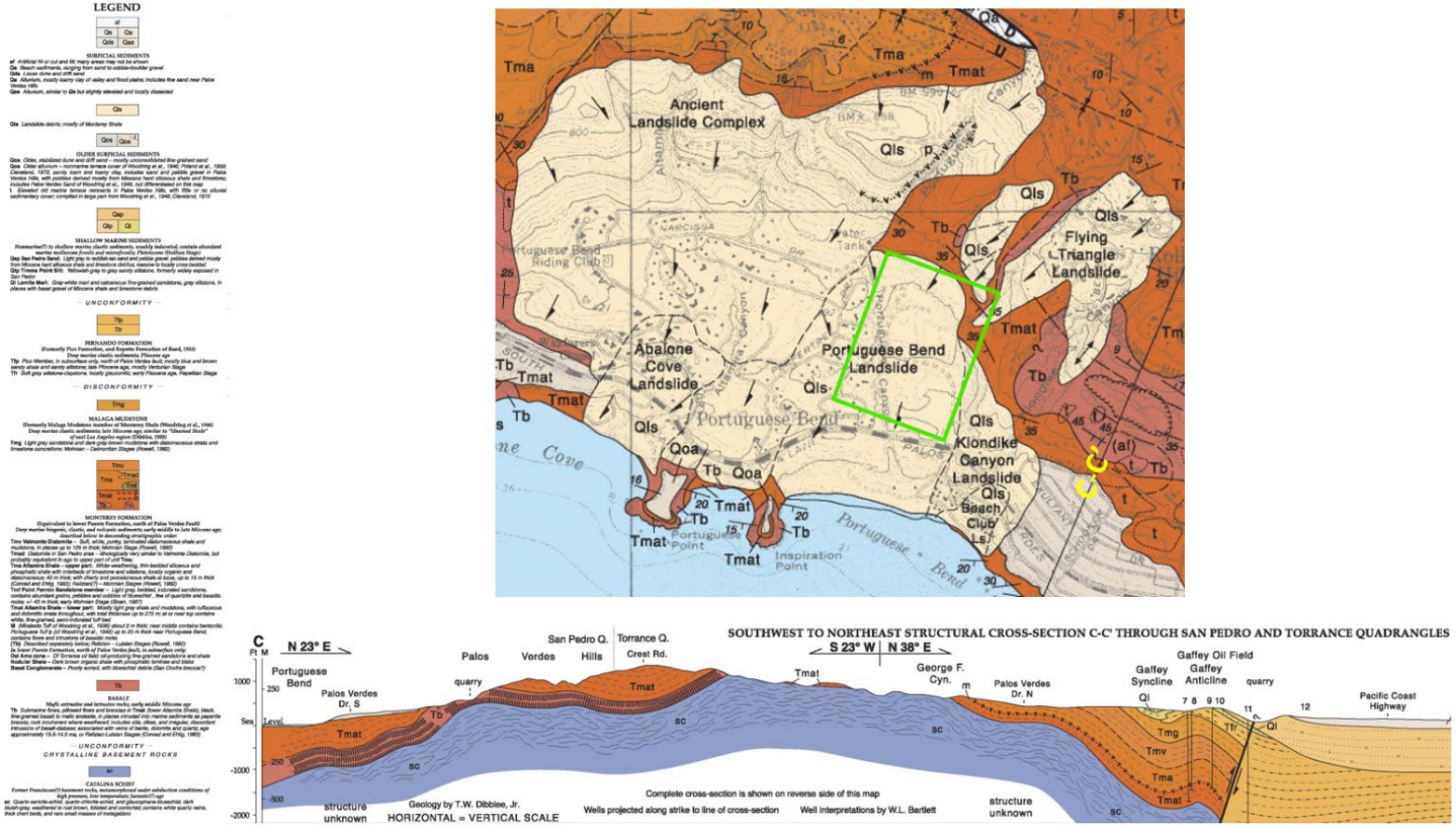

Figure 1.7. Zoomed section of a geologic map of the San Pedro, Redondo Beach, and Torrance quadrangles. A portion of the C-C' cross section detailing the potential structural relationships is shown below and the legend corresponding to the map is displayed on the left. The field area is marked with a green box and the C-C' cross section line is also marked. Modified from Dibblee 2011.

of the Altamira Shale member (Merriam 1960). Despite the geologic susceptibility at this site, the primary triggering mechanism for earth movement on this site is increased water table height. Although seismic hazard such as those presented by the Palos Verdes and Newport-Inglewood faults can have an effect on the slide action, they are typically not the catalysts for earth displacement on the PBL (Ehlig 1987). The PBL is a slump formed from a mixture of Cenozoic volcanic and sedimentary rocks, most notably Monterey Formation shale. The shale materials are highly fissile and are more vulnerable to slope failure.

1.2. Site Background:

Landslides are commonly occurring geomorphological phenomena. In many instances these features present substantial risk and hazard to communities, capital assets, and the people living within or nearby. The PBL is a rotational slump and an excellent example of the interaction between a populated human community with substantial financial investment in property and the destruction of that property through geomorphological forces. Hazard to humans and their property is very high on the PBL since it is located in the Palos Verdes Hills, a high-income community on the coast of the Palos Verdes Peninsula. Development of this community is directly linked to the movement and subsequent landslide hazard in this area. The 1956 construction of the Crenshaw Boulevard extension resulted in the activation of a previously dormant section of landslide. The originally planned extension would connect Crenshaw Boulevard at the top of the Palos Verdes Hills to Palos Verdes Drive South (Ehlig 1987). During the construction of an embankment for the road, the water runoff from the construction site introduced significant weight to the loose sediment, lubricated a zone of weakness in the

underlying Altamira Shale, and prompted mass movement in the weakened material during the next month (Watry and Ehlig 1995). Initially the sliding material moved at a maximum speed of approximately 10 centimeters a day. Over the period of the next few months the area of slope failure continued to widen until reaching its modern extent in the spring of 1957 (Watry and Ehlig 1995). A map and cross sections of the slide interpolated from borehole data are shown in Figures 1.8 and 1.9. This initial activation resulted in the displacement of 104 hectares of material with continued movement of approximately one centimeter per day up until 1972 (Linden 1989). The activation of the slide also resulted in approximately 10 million dollars in damage during the initial episode of movement (Merriam 1960). Continual movement through the present day presents an engineering quandary for the Palos Verdes community. Damage to roads and the continued potential risk to homes, either from the current active body or from dormant sections, provide significant motivation for the characterization of the PBL's subsurface properties. The approximate route of the extension can be viewed in Figure 1.10.

1.3. Portuguese Bend Landslide Mechanics:

A notable fraction of the PBL complex has existed for approximately 126 thousand years and most of its ancient extent is historically stable. Much of the ancient landslide has not experienced notable movement in the recent past (Ehlig 1987). This has also been confirmed through interferometric synthetic aperture radar (InSAR) work performed on the PBL as a whole (Calabro 2010). The location of the cross sections C-C' and D-D' relative to the boundaries of the study area are shown in Figure 1.11. Depths to the sliding

surface shown in the cross sections were determined through borings and interpolated from a combination of borehole observations, outcrops, and structural features (Watry and Ehlig

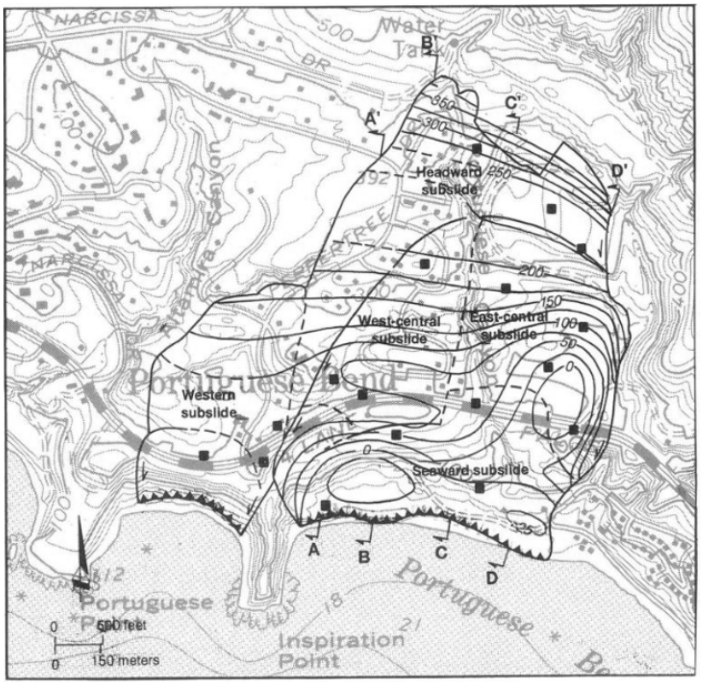

Figure 1.8. Map illustrating sampling locations for bentonite remolding in addition to cross section profile lines. Bentonite remolding is done in a lab to determine the shear strength and other physical properties of the clay. Cross section lines cross the field site from north to south and are key in constraining the subsurface geometry. Measurements were collected at the square points. Contours show slide plane elevation in feet above sea level and were interpolated from borehole data and outcrop examination. Adapted from Watry and Ehlig 1995.

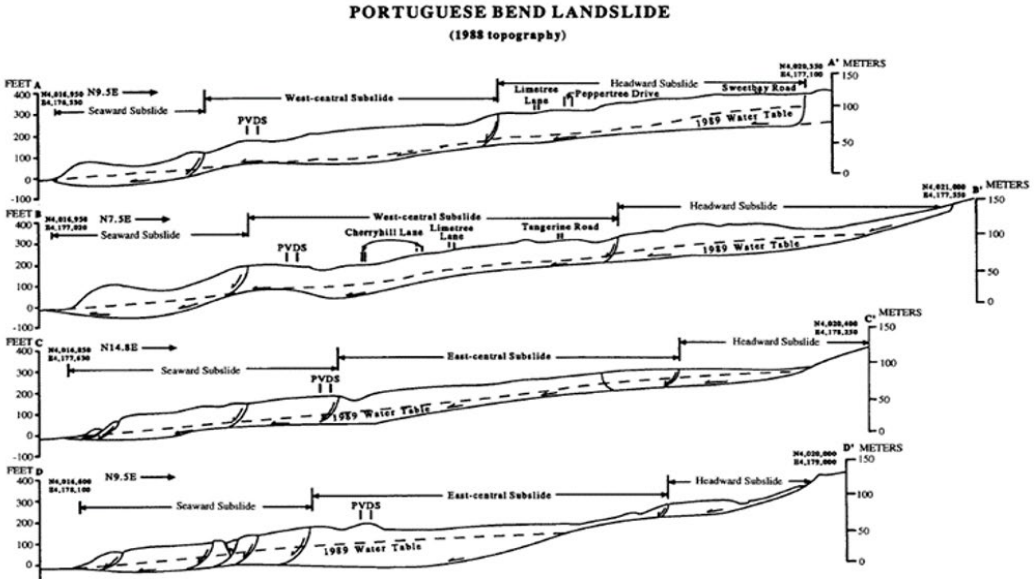

Figure 1.9. Four cross sections generated from trenching and borehole data are shown. Elevations of slide plane and sliding material above and below sea level in meters and feet can be determined from the adjoined rulers. Modified from Watry and Ehlig 1987.

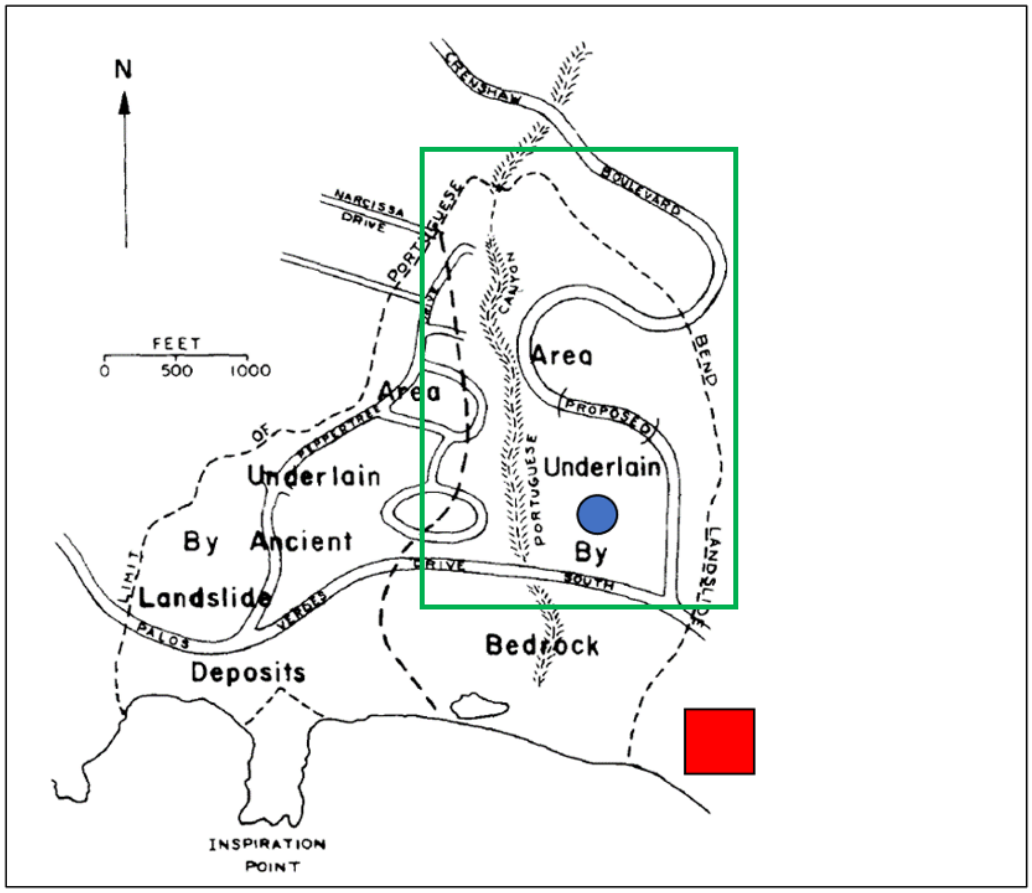

Figure 1.10. Rough sketch map delineating the proposed route for the Crenshaw extension to Palos Verdes Drive South. Construction of the extension was terminated following the initiation of earth movement, sliding, and serious damage to property. The field site is marked with the green rectangle. The approximate location of the western extent of the Portuguese Bend Club, a private housing community at risk from the sliding, is marked with a red square. The supposed location for Ishibashi Lake according to local testimony is marked by a blue circle. Modified from Linden 1989.

1995). In the past, sliding on the PBL complex was typically trigggered by a combination of seismic activity on the Palos Verdes Fault and rising height of the water table (Bryant 1987). A significant factor that contributes to the sliding in these events is the breakdown of the tuff in the middle and lower members of the Altamira Shale into bentonite clay (Brooke 1990). The overlying material is typically clay rich material derived from shale and mudstone units, meaning that it is relatively impermable. The graben and the tension fractures in the overlying material provide a passage for water to infiltrate to the sliding surface, thus allowing for lubrication of the interface between the bentonite and overlying

material (Reiter 1984). In 2010, the majority of the Palos Verdes Peninsula showed negligible movement, but the active section of the PBL exhibited velocities ranging from 0.5 to 2 meters per year (Calabro 2010). More recent InSAR observations constrain the range of velocities further and also revealed that the landslide velocities vary across the

Figure 1.11. The field area Is displayed with two of the four lines Ehlig used to create his cross sections. Sections A-A' and B-B' fall outside of the surveyed area. The rough extent of the field area is enclosed in the green rectangle. PVDS is Palos Verdes Drive South.

slide expanse, as well as corroborate claims that seasonal fluctuations as a result of rainfall play a role in velocity variance (Bouali 2019). The highest magnitude velocities were

detected in the toe of the slide, ranging from 1.6 meters per year to 0.2 meters per year over the course of approximately eight years (Bouali 2019). Deformation on the slide was observed to be cyclical and although seasonal rainfall appeared to contribute to localized changes in velocity, the general trend observed showed a much longer period between events of fast movement and significantly decreased activity (Bouali 2019). The relative velocity of the active PBL relative to the rest of the sections is displayed in Figure 1.12. The active zone exhibits consistent movement seaward to the south west. This section, which constitutes less than half of the entire PBL complex, was reactivated in August of 1956 during the construction of a proposed extension to Crenshaw Boulevard. During the construction of an embankment for the road, the water runoff from the construction site introduced significant weight to the loose sediment, lubricated a zone of weakness in the underlying Altamira Shale, and prompted mass movement in the weakened material during

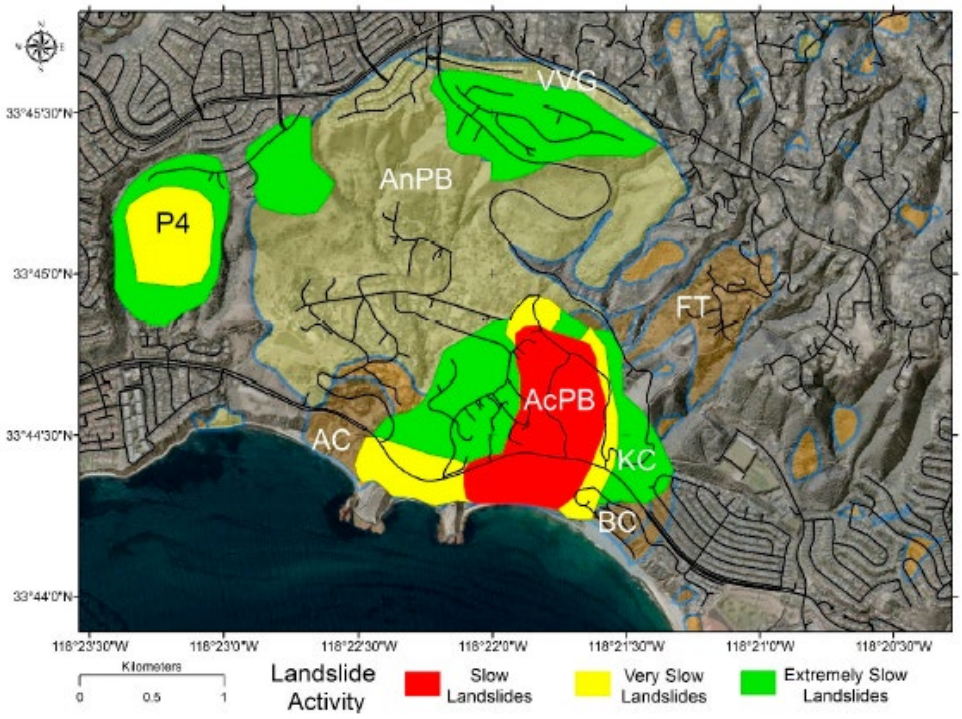

Figure 1.12. Relative velocity map for the Portuguese Bend Landslide. The field area falls with the AcPB which exhibits the most activity and highest relative velocities of the other sections. Adapted from Bouali 2019.

the next month (Watry and Ehlig 1995). Initially the sliding material moved at a maximum speed of approximately 10 centimeters a day. Over the period of the next few months the area of slope failure continued to widen until reaching its modern extent in the spring of 1957 (Watry and Ehlig 1995). Although work on the extension was terminated soon after activation, the majority of homes inside the slide were destroyed. A small number of homes escaped severe damage and still other structures were transferred onto new foundations outside the boundaries of the sliding area (Watry and Ehlig 1995). Despite slowing to a significantly slower rate of displacement, the reactivated section of the landslide continued to move and place other properties in close proximity to the slide at risk, prompting the city of Rancho Palos Verdes to hire engineers to stabilize, halt, or at the least change the direction of the moving earth away from the Portuguese Bend Club (PBC) to the south (Ehlig 1987). Stabilization work commenced and was quickly found to be insufficient in halting the steady seaward progress of the material. As a contingency, the engineers piled loose earth, owned by the PBC, on the southeast proximal of the landslide toe with the intent of changing the direction of the moving earth. This proved successful in diverting the movement of the earth away from the PBC and changed the slide's vector to a more westerly direction. Earth was also moved to fill in Ishibashi Lake. Long term residents of the area claimed that Ishibashi Lake was inundated with earth collected from the Portuguese Bend Club by engineers (Ehlig 1987). This lake is still fed via groundwater flow. Additionally, pylons, dewatering wells, and earthworks were used in conjunction with the implementation of artificial controls for water drainage towards the northwest edge. Ultimately, all of these methods failed to stop the progression of the landslide, but the direction of the slide movement appears to have been altered slightly, although

continued maintenance of earthworks and installed piping will likely need to continue (Ehlig 1987). Interpolated contours for the elevation of the slide plane above sea level are displayed in Figure 1.8. Ehlig's research suggests that the slide plane generally undulates between 5 to 50 meters at depth with some localized near-surface exposure in some areas and a small number of locations exhibiting depths greater than 50 meters (Ehlig 1987). The existing topography and subterranean canyons still drain naturally despite the construction of motion-impeding earthworks and drainage infrastructure as is evidenced by surface runoff and the continuance of unmanaged drainage in the form of large gullies that form and trend towards the southwest edge of the slide. The gullies are open roughly perpendicular to the landslide scarp and tension troughs that span the slide from the east to west (Ehlig 1987). Tension troughs provide rapid passage for water to reach the slide plane. With the introduction of water to the Altamira Shale and tuffaceous units, the cemented volcanic ash breaks down into bentonite clay which lubricates the weak fissile shale. Bentonite clays typically exhibit high liquid limits, low plastic limits, and large plasticity indices. The high magnitude water retention capacity and low plasticity index of bentonite allow for the slide to move with the introduction of small amounts of water, while retaining that moisture for a greater duration than most landslides. Significant bentonite quantities at the slide plane cause the PBL to dewater at a rate ten times slower than expected (Ehlig 1987). Bentonite is known for substantial water retention capacity and general impermeability. As a clay, it also has significant porosity with small pore size and high tortuosity which in turn results in lower magnitude Darcy flux. Since the weathering of units in the Crenshaw extensions stratigraphic section typically produces bentonite, and since the slip plane for the slide is contained within the Altamira Shale unit found in the

Crenshaw extension section, these factors could help to explain the slow dewatering rates present on the slide, while also partially contributing to continued sliding (Watry and Ehlig 1995). Borehole data and soil analysis also indicate that the material at the sliding surface is bentonite clay (Watry and Ehlig 1995). As such, the slow dewatering rate at the PBL is likely due in part to material at the sliding surface as well as the overlying slide material.

1.4. Landslide Imaging Methods:

Data collection methods for subsurface studies can be loosely divided into invasive and noninvasive methods, where invasive methods are potentially expensive and usually disruptive to the flora and fauna in the area. Invasive geophysical methods include, but are not limited to, borehole drilling and trenching. The PVPLC also deemed active source seismic reflection and refraction, electrical resistivity, and underground seismometer deployment to be potentially disruptive to flora and fauna, while also presenting a safety hazard to the pedestrians traveling on the site, despite these methods generally being considered to be noninvasive. Noninvasive methods also include, but are not limited to, magnetometry, gravity, ground penetrating radar, and H/V spectral ratio methods. The primary method utilized during this experiment is H/V spectral ratio. The execution of this method involves the deployment of seismometers above ground at selected points during which time passive ambient noise data is collected over the duration of the deployment. The data is processed such that the ratio of the horizontal and vertical amplitudes of the ground of motion of the passive ambient noise data can be plotted as a function of frequency. The resulting curves may display a peak frequency, which is an important site response characteristic used to derive parameters such as the potential depth to a strong acoustic boundary. The curve itself can be used to analyze directionality of the passive

noise, and the structural integrity of acoustic boundaries (Del Gaudio 2013). H/V spectral ratio surveys executed in this manner are noninvasive, which made this particular experimental procedure a prime choice for this study. Seismic reflection and refraction surveys would likely be useful in characterizing this field site, but were restricted due to the permitting process involved with active seismic sources. Seismic refraction or reflection surveying would be very useful when combined with H/V spectral ratio surveying, because it facilitates determining the S-wave velocity of the surface layer, in addition to providing data that can be readily applied in determining the shape of underground geometry. Deploying seismometers underground enables long term data collection periods that includes sampling during evening hours. However, the permitting restrictions forbade digging holes or any soil disruption. For this experiment, ground based magnetometry was utilized, because it was not invasive and because it could detect mafic intrusions if present, and possibly map the thickness of the overlying slide material or the depth to the basement rocks. The susceptibility contrast between basement rocks and overlying material is typically large enough to determine sediment thickness (Nabighian 2005). In this case, the bedrock is not crystalline igneous rock, so the susceptibility contrast between bedrock and overlying material is most likely small. Ground penetrating radar is typically used to find linear subsurface features such as pipes, buried walls, or objects. However, it can also be deployed to detect subsurface boundaries if there exists a great enough contrast in dielectric permittivity at the boundary. Because it was noninvasive, ground penetrating radar units were utilized with the intent of detecting the PBL sliding surface. GPR was shown to be effective in imaging facies changes and shearing surfaces, such as the sliding interface, on the Quesnel Forks Landslide (QFL) (Bichler 2004). The

QFL, like the PBL, has significant clay content in the overlying sliding material. Gravity traverses have been utilized to great effect on other landslides to identify zones of increased stratum thickness, material boundary contrasts, and isolated subsurface pockets of locally anomalous density. For this field site gravity was used largely because it presented another noninvasive data acquisition option that could be used alongside the other methods. Gravity traverses were executed on the Guinsaugon landslide in the Phillipine fault zone to model the basement shape as well as identify the boundaries of the landslide (Makino 2007). Although electrical resistivity could not be used at this site due to permitting conditions, it has been utilized by numerous researchers to determine the physical and geometric properties of landslides. Although these surveys are often able to detect the sliding surface below the landslide material, the primary purpose of resistivity surveys resides in the reliable detection of subsurface water and ultimately the characterization of flow direction and/or storage of water on top of the sliding surface. Work on the Kualangzi landslide located in the Sichuan Basin in China accomplished this task by correlating surface geomorphological indicators with the subsurface readings collected along the resistivity profile (Ling 2016). The data indicated that subterranean water would generally enter the slide through tension troughs. Water movement through tension troughs is rapid until it comes into contact with the slide plane. At this point drainage is largely lateral and follows the dip of the sliding surface towards the toe (Ling 2016). Figure 1.13 a cross section and a resistivity tomography plot collected at the Kualiangzi landslide. Resistivity experiments were not executed on the PBL field site, but the subsurface morphology that was delineated by Ling and others allows for some assumptions to be made concerning the subsurface characteristics of the PBL. Water gathers in the concave sections of the sliding surface if

the plane is non-uniform or undulatory, but the composition of the landslide material will control the height of the water in the soil column given the soil composition, porosity, and other physical parameters. Note the presence of the shale units relative to the tuffaceous units. The ideal conditions for bentonite lubrication of the weak material prevail during the rainy season. Although the slow dewatering was at first attributed to slow percolation rates, work at the Kualiangzi landslide has shown that water retention is longest on the sliding surface, which in turn helps to explain the increased ground movement or susceptibility to movement for long periods following rainfall. Beyond the fact that slow dewatering

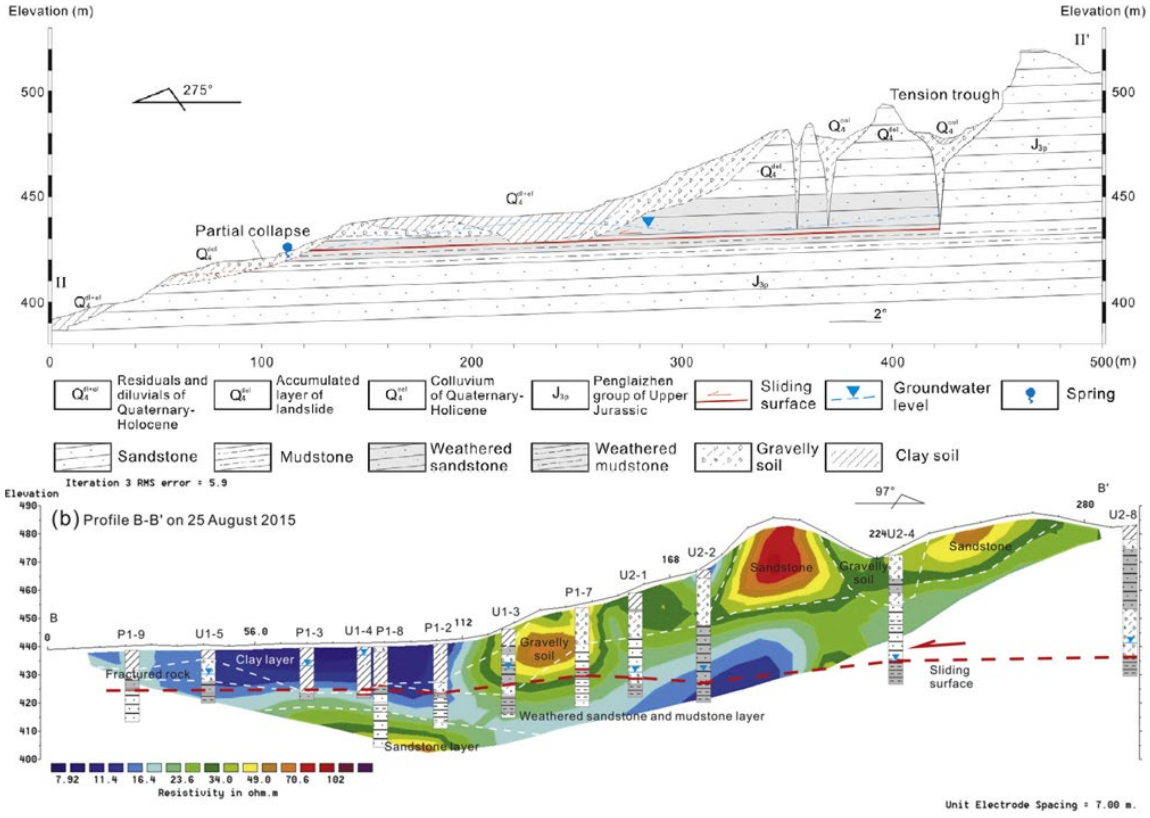

Figure 1.13. The cross section II-II' and the resistivity profile line B-B' is displayed as well. Profile II-II' is roughly parallel to B-B' Tension spreading zones provide a potential route for rapid infiltration of rainwater into the water table. This mechanism provides a potential mechanism by which water would infiltrate to the water table on the PBL as well. Modified from Ling 2016.

rates are linked to longer sliding durations, and rapid initiation of movement after water introduction through either rainfall or anthropogenic runoff, slow dewatering rates also

have a marked effect on subsurface parameters. For example, determining depths to the sliding surface with H/V spectral ratio methods is much more difficult if water has been recently introduced into the system, but determining depth to subsurface water after rainfall has finished percolating to a relatively impermeable boundary is much easier (Del Gaudio 2013). Groundwater flow is slow since the bentonite's substantial water retention disallows for rapid evacuation of subterranean fluid. This means that assumed values for seismic velocity are more reliable when the soil is dry and are not after precipitation occurs. This in turn complicates the determination of depth to the sliding surface or the subsurface water after rainfall events. Our main initial goal is therefore to determine whether any significant changes to the HVSR curves occur after rainfall.

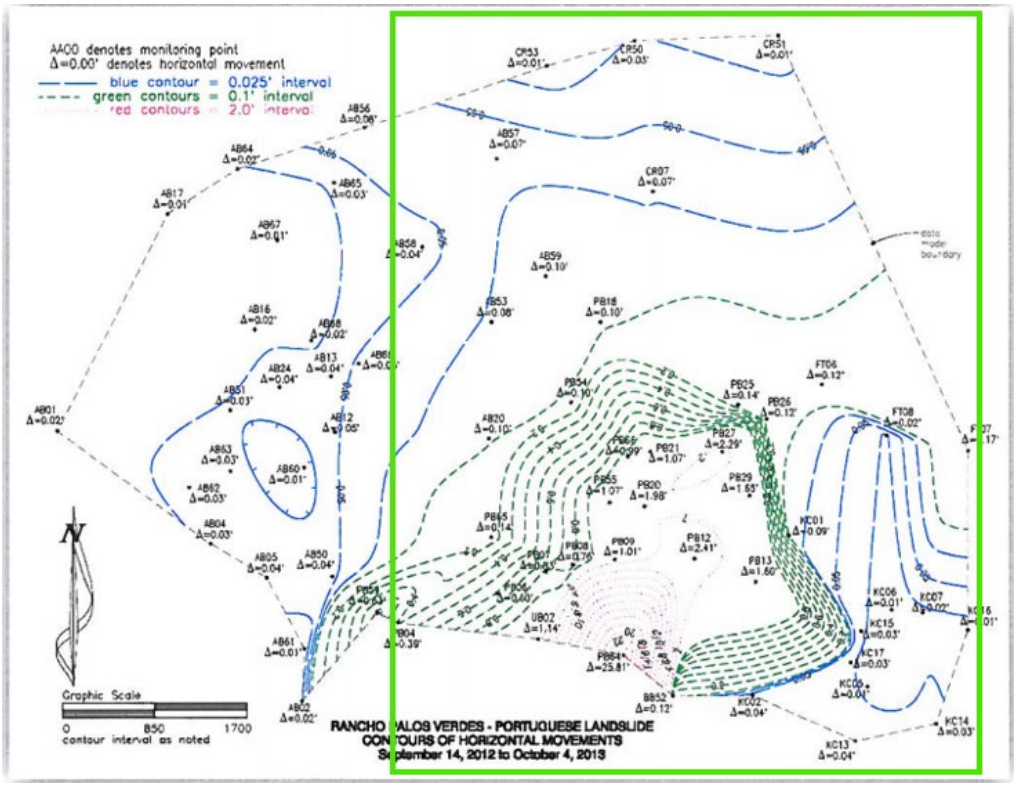

Figure 1.14. GPS vector contour map illustrating material displacement over a period of three years. The outer bounds are extremely slow-moving and material moving in the center of the slide continues to move more rapidly. Field Area is contained in the green rectangle. Adapted from McGee 2013.

1.5. Other Work on PBL:

The principal data-collection method in the past has typically been restricted to borehole data and soil cores, but other methods have been utilized. Figure 1.14 illustrates displacement contours derived from GPS data. GPS landslide vector analysis tells us that material more proximal to the slide toe was displaced at a rate of two or more feet from 2010 to 2013 (McGee 2013).

The rest of the landslide material traveled at a rate of less than a foot over the past three years. Ehlig's earthwork berm, an engineered barrier constructed with relocated soil material, installed on the southeast section of the PBL has successfully changed the direction of material motion to a more westerly vector. Continual wave action eroding the

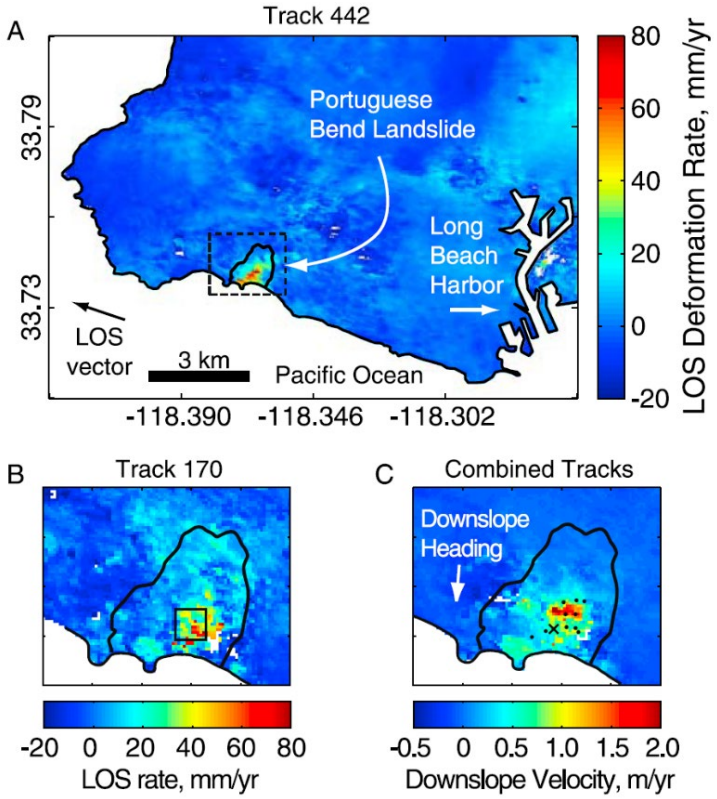

Figure 1.15. Line of sight deformation rates for two separate satellite tracks are shown. Both were taken during the summer season during a five-year span. Combined tracks were used to produce a downslope velocity and vector heading. Adapted from Calabro 2010.

toe of the landslide keeps the weight distribution of material on the slope unstable, thus allowing for continual failure of the slope with southward movement (Ehlig 1987).

Additionally, the PBL has been examined through the lens of InSAR. Seasonal deformation patterns were observed by stacking interferograms produced from 5 years of data (Calabro 2010). Figures 1.15 and 1.16 illustrate the stacked interferogram results. Rapid deformation rates necessitated the adoption of a less conventional analytical technique. By examining the degree of phase decorrelation present in produced interferograms alongside GPS motion data, a strong association between rain events and increased deformation could be drawn (Calabro 2010). The seasonal flux could not only be observed, but also be used to estimate lag time, the time between the initiation of precipitation and the acceleration of the sliding material, using approximated infiltration rates. Ultimately a strong correlation between seasons and increased movement was determined with increased movement from January through May after the rainy season begins in December (Calabro 2010).

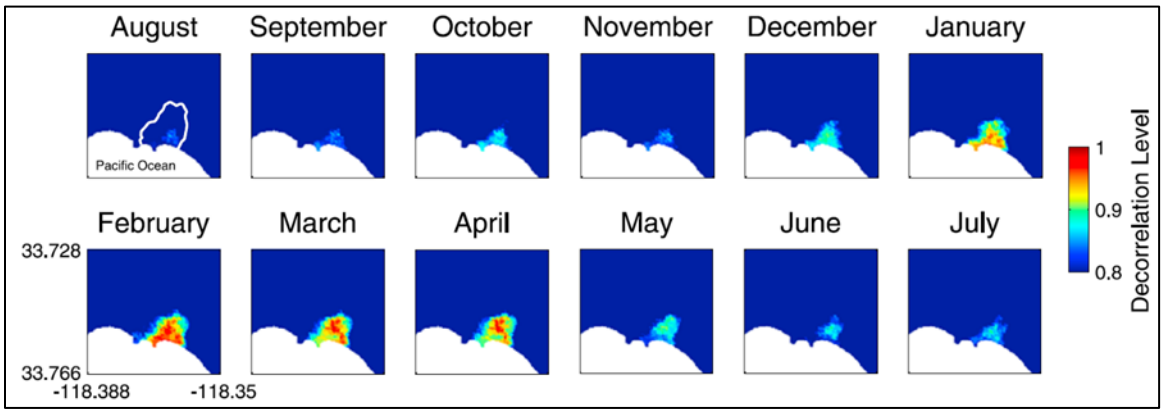

Figure 1.16. Five years of interferograms separated by month. High phase decorrelation is shown in warmer colors and low phase decorrelation is shown in cooler colors. The rainy season typically starts in December and ends in April. Spikes in phase decorrelation occur starting in January and persist through May. Adapted from Calabro 2010.

Previous studies were limited by a variety of factors. Most of the experiments carried out on the slide were focused entirely on surficial geomorphological analysis, including GPS vector analysis, and field mapping of rock outcrops and landslide morphological features. Although the outcrop analyses performed by researchers such as Ehlig are useful components in borehole inquiries and soil investigations, much of the work determining slide plane geometry has been done with limited borehole examinations and correlation to surface structural data. Geophysical investigations have not been performed on the slide using more modern methods. H/V spectral ratio methods were only first pioneered during the 1980s, during which time Ehlig, the principal authority on the PBL, was carrying out the majority of his field excursions and experiments. InSAR examination revealed that seasonal precipitation signals combine with longer period geomorphic signals, producing periods of significantly pronounced motion underscored by periods of substantially reduced activity (Bouali 2019). These signals reveal that the combination of proper seasonal timing along with the erosion and destabilizing of the slide toe through weathering processes can produce conditions conducive to substantial and much more rapid earth movement, but the desynchronizing of seasonal precipitation and slide destabilization through weathering manifest in periods of very slow movement (Bouali 2019). As such, GPS and InSAR monitoring of the site can be combined with meteorological data to predict the onset of cycles or higher velocity earth displacement. Combining multiple other modern methods can provide perspective on the subsurface characteristics that previous studies could not provide due to limited technological development or cost restrictions.

2. METHODOLOGY:

Four methods were utilized during this study: seismic spectral ratio analysis, gravity, ground-based magnetometry, and ground penetrating radar (GPR). The H/V Spectral Ratio (HVSR) method was the primary experimental method, while the other three methods were supplementary. Method application was usually limited to the trails present on the field site, limiting the geographical coverage of some methods, such as magnetometry and GPR. Data processing was performed with method-specific software and spreadsheet tabulation.

2.1. Spectral Ratio Methodology:

Site condition characterization carries substantial significance in the fields of engineering and seismology. One of the key methods used for site characterization is HVSR, during the application of which ambient local noise is collected by a seismometer. Spectral ratio methods are used to examine the frequency-dependent relationship between the horizontal and vertical amplitude of, in this case, the ambient noise ground motion at a site of interest. Deriving a peak frequency or spectral peak of the spectral ratio curve can provide the examiner with important site characteristics such as soil column resonance, which can be used under certain assumptions to derive depth to strong material contrasts, such as the slide plane. HVSR experiments were carried out on the eastern, seaward, and headward subslide sections of the PBL. Precedent for the application of the HVSR method on landslides has been set by numerous previous studies. For example, Meric and associates carried out two HVSR experiments on landslides in the Southern French Alps. In both cases the landslides surveyed were composed of a relatively homogenous clay overlying weak, fissile bedrock (Meric 2007). Cross sections and a field map of the Super-

Sauze mudslide located in the Southern French Alps are depicted in Figure 2.1. Of significant relevance however is the coastal setting of the PBL. Microseismic signals recorded in the 0.1 to 0.4 Hz range may be generated by ocean wave action (Del Gaudio 2013). This presents a problem only if peak frequencies sampled fall within the 0.1 to 0.4 Hz range and only if directionality of the data is not omnidirectional. Del Gaudio examined the landslides on the Caramanico hillslopes using the spectral ratio method. The Quaternary colluvium overlying the clay rich Pliocene sedimentary rocks exhibited characteristics very

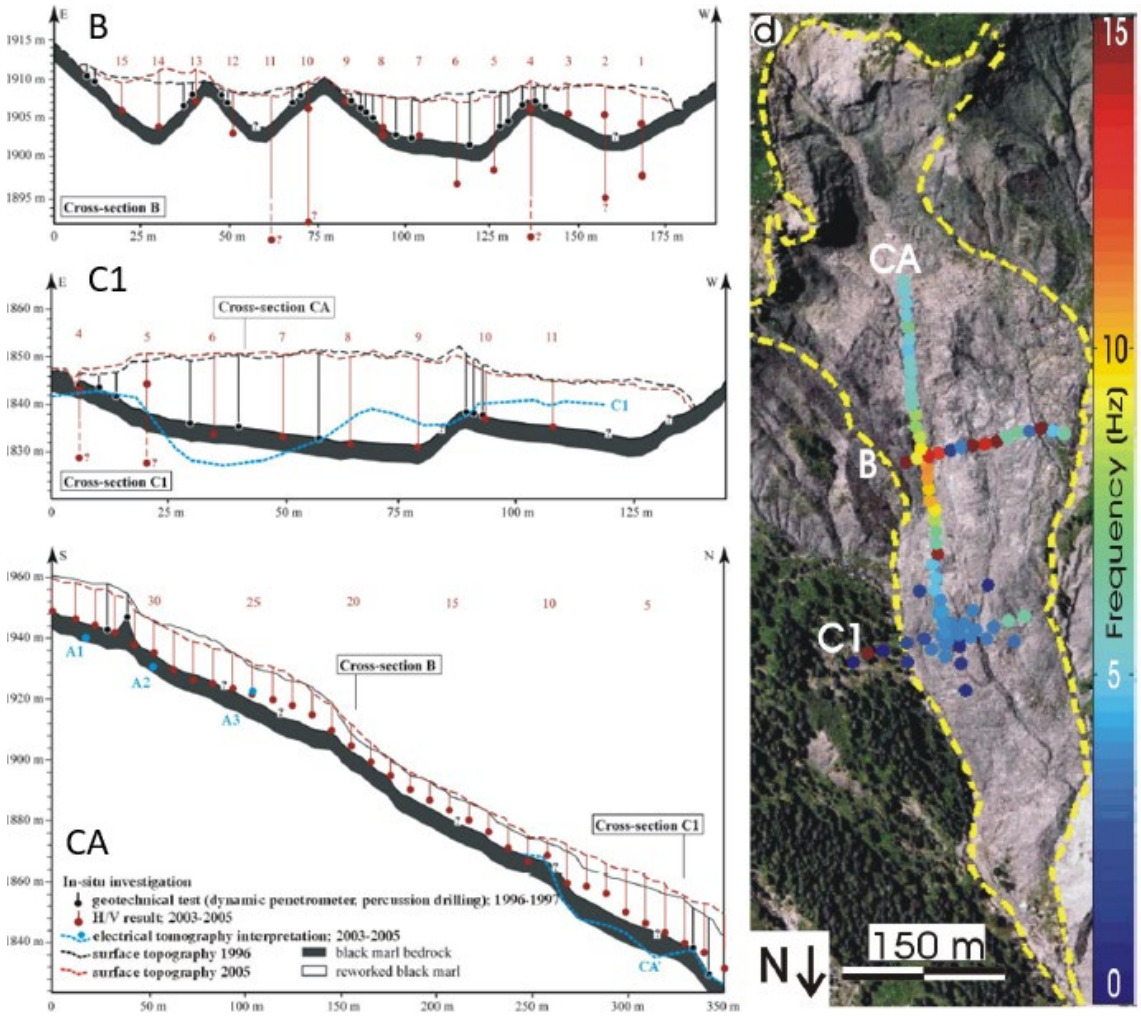

Figure 2.1. Field map of the H/V network at the Super-Sauze mudslide. Cross sections of the HVSR profile lines are shown on the left. Peak frequencies are displayed on the field map with the colors corresponding to the rightmost scale. Modified from Meric 2007.

similar to the PBL. Seismometers were deployed in the same locations before and after rainfall (Del Gaudio 2013). Figure 2.2 exhibits the Caramanico landslide and directional seismic spectral ratio results. Many researchers utilized a quarter wavelength function to

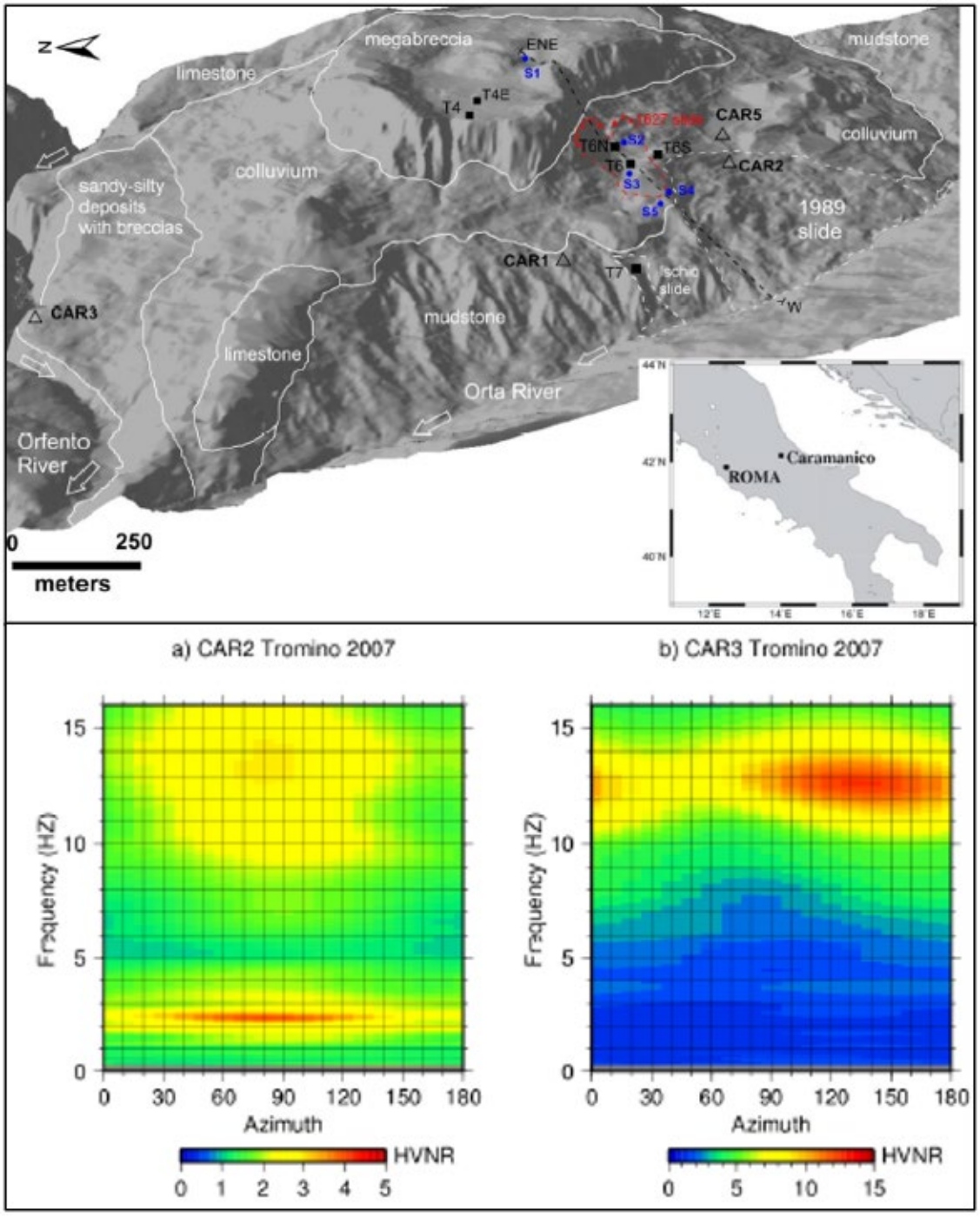

Figure 2.2. Shown is a 3D representation of the Caramanico hillslope and the Caramanico landslide. Sedimentary unit types are overlaid on the image. Azimuthal H/V data is shown below the map for two points. Directionality of passive seismic data is shown. Modified from Del Gaudio 2013.

determine depth from peak frequency. This approach will be explained in more detail later in this section. Although utilizing the wavelength function to determine depth is simple, using it properly requires the satisfaction of a certain conditions. Firstly, the function assumes 1D wave propagation. This means that it ignores 3D site effects, so environments where surface layers are more heterogenous cannot be reliably characterized using the function (Meric 2007). Instead, field sites that can be assumed to have or are shown to possess surface stratum with homogenous compositions can be potentially analyzed with the 1D model. Secondly, the 1D model assumes that there exists a significant S-wave velocity contrast between the first, soft surface layer and the more rigid underlying layer (Meric 2007). It has been suggested that the ideal 1D conditions for depth determination are not common in landslide areas, as the slides stratums and structures are too complex to be assumed as homogenous (Del Gaudio 2013). Additionally, the data acquired from the H/V method can potentially be used to infer directionality of passive noise as a site response characteristic, such as the influence of the dip direction of an acoustic boundary and its impact on the peak frequency and recorded azimuths of the seismic data (Del Gaudio 2013). Despite this, some examiners choose to use the basic function and perform additional surveys to determine the range of normal peak frequencies at each sampling location. The averaged peak of interest is then used in the quarter wavelength function and the result is sometimes verified against seismic refraction and/or reflection surveys (Meric 2007). Imposa also employed HVSR methods on the Tripi landslide in Italy. This slide has physical characteristics similar to the PBL, and Imposa employed both the standard derivation of the quarter wavelength function and a modified variant that accounted for other variables. The quarter wavelength function or a modified variant of the function was

used to derive depths to the sliding surface from the peak frequency values recorded at each sampling location (Imposa 2016). Unlike my experiment on the PBL however, Imposa carried out a multi-channel analysis of surface waves survey in addition to performing an HVSR survey. This method is particularly useful when coupled with HVSR surveys, because it can be used to determine the velocity of shear waves in the layers of interest (Imposa 2016). Figure 2.3 shows the general location of the Tripi landslide and the seismic spectral ratio curves corresponding to the profiles collected during one day. For my site, a Guralp CMG seismometer was deployed at each location for data collection lasting for approximately two hours and fifteen minutes at each sampling site. Locations were tested during dry periods long after the most recent rainfall, and the same or close approximate locations were tested two days after significant rainfall. Data were then flushed from the seismometer to an external hard drive in the field as seismic analysis code (SAC) files, which were then stored on a permanent storage disk. Data were extracted using GCF Extract. Spectral ratio analysis was then carried out on each SAC file using Geopsy, a free geophysics data viewing and processing software (Wathelet 2020). Using the built-in tools in Geopsy for H/V spectral ratio curve building, the data were processed with multiple conditions. Frequencies were sampled within a range from 0.5 to 20 Hz with anti-triggering on raw signal. Window selection on the SAC files was generally run at a duration of 25 to 60 seconds per window with some run at durations greater than 60 seconds per window. Windows were automatically selected using the software's selection algorithm, and in some cases, windows were manually deselected. Data were also run through the Geopsy H/V Rotate tool to determine whether or not the curves indicated multi-directional ambient noise, or if nearby energy sources such as the nearby road, wind, vegetation, foot

traffic, ocean waves, or other directionally specific energy sources were overly represented. An initial curve was generated from the SAC data collected at each location. From this, additional filtering of windows was applied through human selection. Windows that appeared to encompass periods of seismometer equilibration instead of passive ambient noise were deselected to better constrain the peak frequency, reduce error, and increase

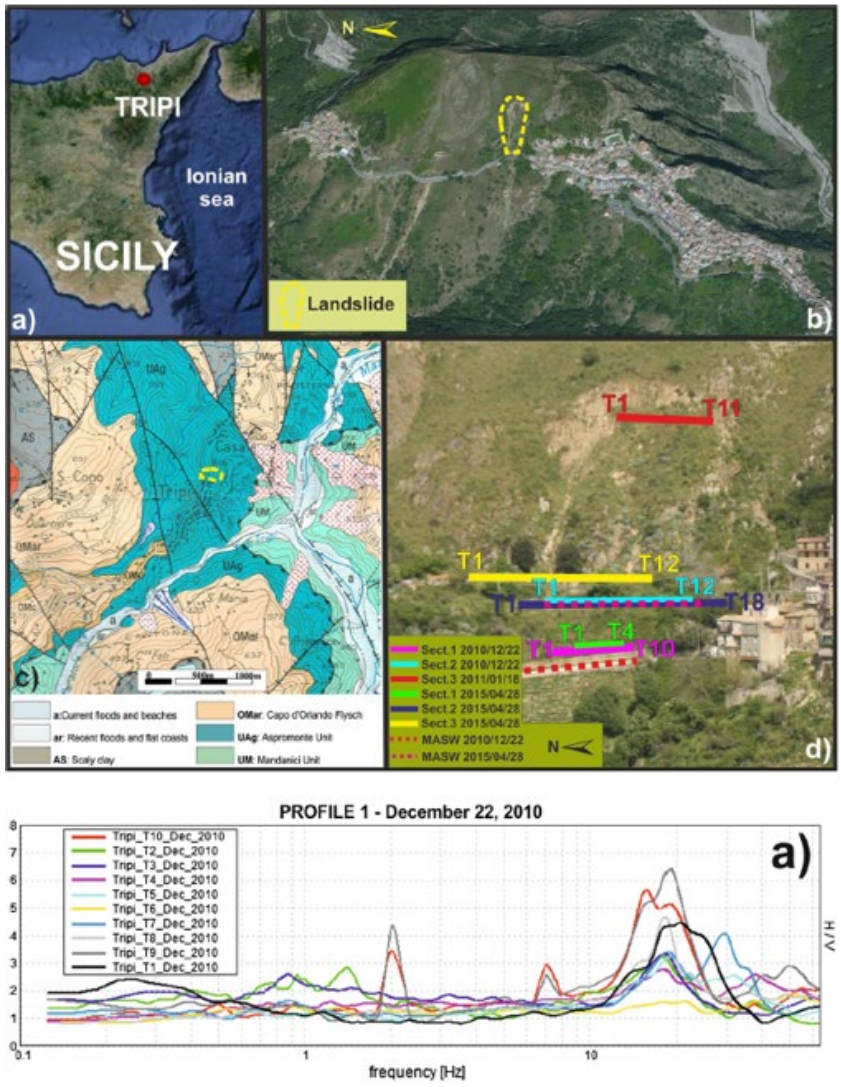

Figure 2.3. Map displaying the general location of Tripi and closely proximal unnamed landslide. HVSR profiles are shown for particular deployment locations along each profile line. Modified from Imposa 2016.

visual clarity of the curve. After final selections were made and the curves were calculated to the level of least observable error, a number of numerical and statistical attributes of the

curves were checked against criteria to determine whether or not they were satisfactory for further analysis. Since the peak frequencies derived from the spectral ratio curves represent resonance of S-waves in the soil column, peak frequency data from reliable curves was then used in a quarter wavelength function of the following form:

1) $$f_0^{\frac{H}{V}} = \frac{V_s}{4 \cdot h}.$$

where h is the depth to the material discontinuity, V_s is the S-wave velocity in soil similar to the surficial soil at the field site, and f_0 is the peak frequency. Depths thus determined were compared against borehole data and general estimates developed by other researchers. V_s was assumed to be approximately 145 meters per second (Xia 1999). This value was selected because it represents a likely value for uncompressed, low-density, churned surface material.

2.1.1. SESAME Criteria:

The Site EffectS Assessment using Ambient Excitations (SESAME) criteria provide a foundational standard for judging the adequacy and quality of the collected data (EC-RGD 2004). Figure 2.4 displays the SESAME peak clarity and peak reliability criteria recommended for H/V spectral ratio surveys. To help with experiment design and data analysis, SESAME guidelines were employed to help gauge the effectiveness of data collection, provide constraints for analysis, and were also used to determine whether the collected information was statistically sufficiently relevant to draw conclusions about the subterranean geometry of the landslide. If a curve is generated from data with window durations that are too short relative to the peak frequency, or if too few windows can be selected and used to generate the curve, or if

the standard deviation of the amplitude of the peak frequency is too large, then the spectral ratio curve is unreliable and should not be used in interpretations about the sampling location. In this case, the curve might be statistically unreliable despite showing a clear peak at a particular frequency. On the other hand, a curve may be deemed reliable, but will not exhibit a clear peak frequency within the frequency range of interest. In this case, interpretations can be drawn from it regarding the site's response characteristics, but no simple strong subsurface material contrast is detected. This could also indicate that a resonant boundary exists very close to the surface of soft stratum, the resonant boundary could be fractured, or the resonant boundary could be very steeply dipping. Unreliable curves have very little, if any, value. Processing parameters for sampled locations can be adapted on a curve-to-curve basis if criteria are not adequately satisfied with another set of parameters.

Criteria for a reliable H/V curve

i) $f_0 > 10 / l_w$

and

ii) $n_c(f_0) > 200$

and

iii) $\sigma_A(f)<2$ for $0.5f_0<f<2f_0$ if $f0>0.5Hz$

or $\sigma_A(f)<3$ for $0.5f_0<f<2f_0$ if $f0<0.5Hz$

Criteria for a clear H/V peak

(at least 5 out of 6 criteria fulfilled)

i) $\exists f^- \in [f_0/4, f_0] \mid A_{H/V}(f^-) < A_0/2$

ii) $\exists f^+ \in [f_0, 4f_0] \mid A_{H/V}(f^+) < A_0/2$

iii) $A_0 > 2$

iv) $f_{peak}[A_{H/V}(f) \pm \sigma_A(f)] = f_0 \pm 5\%$

v) $\sigma_f < \varepsilon(f_0)$

vi) $\sigma_A(f_0) < \theta(f_0)$

- l_w = window length
- n_w = number of windows selected for the average H/V curve
- $n_c = l_w \cdot n_w$. f_0 = number of significant cycles
- f = current frequency
- f_{sensor} = sensor cut-off frequency
- f_0 = H/V peak frequency
- σ_f = standard deviation of H/V peak frequency ($f_0 \pm \sigma_f$)
- $\varepsilon(f_0)$ = threshold value for the stability condition $\sigma_f < \varepsilon(f_0)$
- A_0 = H/V peak amplitude at frequency f_0
- $A_{H/V}(f)$ = H/V curve amplitude at frequency f
- f^- = frequency between $f_0/4$ and f_0 for which $A_{H/V}(f^-) < A_0/2$
- f^+ = frequency between f_0 and $4f_0$ for which $A_{H/V}(f^+) < A_0/2$
- $\sigma_A(f)$ = "standard deviation" of $A_{H/V}(f)$, $\sigma_A(f)$ is the factor by which the mean $A_{H/V}(f)$ curve should be multiplied or divided
- $\sigma_{logH/V}(f)$ = standard deviation of the $\log A_{H/V}(f)$ curve, $\sigma_{logH/V}(f)$ is an absolute value which should be added to or subtracted from the mean $\log A_{H/V}(f)$ curve
- $\theta(f_0)$ = threshold value for the stability condition $\sigma_A(f) < \theta(f_0)$
- $V_{s,av}$ = average S-wave velocity of the total deposits
- $V_{s,surf}$ = S-wave velocity of the surface layer
- h = depth to bedrock
- h_{min} = lower-bound estimate of h

Threshold Values for σ_f and $\sigma_A(f_0)$

Frequency range [Hz]	< 0.2	0.2 – 0.5	0.5 – 1.0	1.0 – 2.0	> 2.0
$\varepsilon(f_0)$ [Hz]	0.25 f_0	0.20 f_0	0.15 f_0	0.10 f_0	0.05 f_0
$\theta(f_0)$ for $\sigma_A(f_0)$	3.0	2.5	2.0	1.78	1.58
$\log \theta(f_0)$ for $\sigma_{logH/V}(f_0)$	0.48	0.40	0.30	0.25	0.20

Figure 2.4. H/V spectral ratio criteria for reliable curves and clear peaks. Adapted from EC-RGD SESAME 2004.

2.2. Gravity Methodology:

Gravity profile measurements collected on landslides are typically used to model changes in the 3D shape of the slide from wasting events, to constrain the boundaries of the slide, to detect changes in the thickness of the slide laterally or over time, or to discover variations in density relative to the neighboring areas. For example, mass wasting features, such as those caused by volcanic upheaval on the Canary Islands, can be effectively imaged but gravimetric techniques can also be utilized for smaller slides requiring a more localized anomaly characterization (Carracedo 1996). A number of researchers have sampled and compiled data on limited and expansive sliding bodies. Makino performed a gravity survey on the Guinsaugon landslide. The Bouguer anomaly characteristics, field map with elevation, and a graphical cross section of the Guinsaugon landslide are displayed in Figure 2.5. Work performed by Makino on the Guinsaugon landslide along the Philippine Fault Zone shows that anomaly fluctuations across their profile lines equaling approximately ten milligals is sufficient in allowing for subsurface modeling and determination of the shape of the subsurface geometry (Makino 2007). Additionally, the boundaries of the landslide were relatively well defined by the variation in the Bouguer anomaly values measured across the profile line (Makino 2007). However, work by Brooke on the Alum Rock landslide in eastern San Jose claimed that his gravity survey failed to accurately locate the edges of the Alum Rock landslide (Brooke 1973). The difference between successful and failed gravimeter surveys on each of these sites could be explained by the scale of each location. Brooke employed gravimetrics with the goal of identifying the locations of a structural transitions from landslide to bedrock on a landslide of significantly smaller extent than that of the Guinsaugon landslide studied by Makino. Brooke recorded

anomalies with a 0.8 milligal range (Brooke 1973). The feature examined by Makino covered a much larger expanse that possessed a significantly thicker layer of mixed earth, across which the gravity signal for the material contrast between the slide within the graben and basement rock boundaries confining the slide would be more starkly apparent

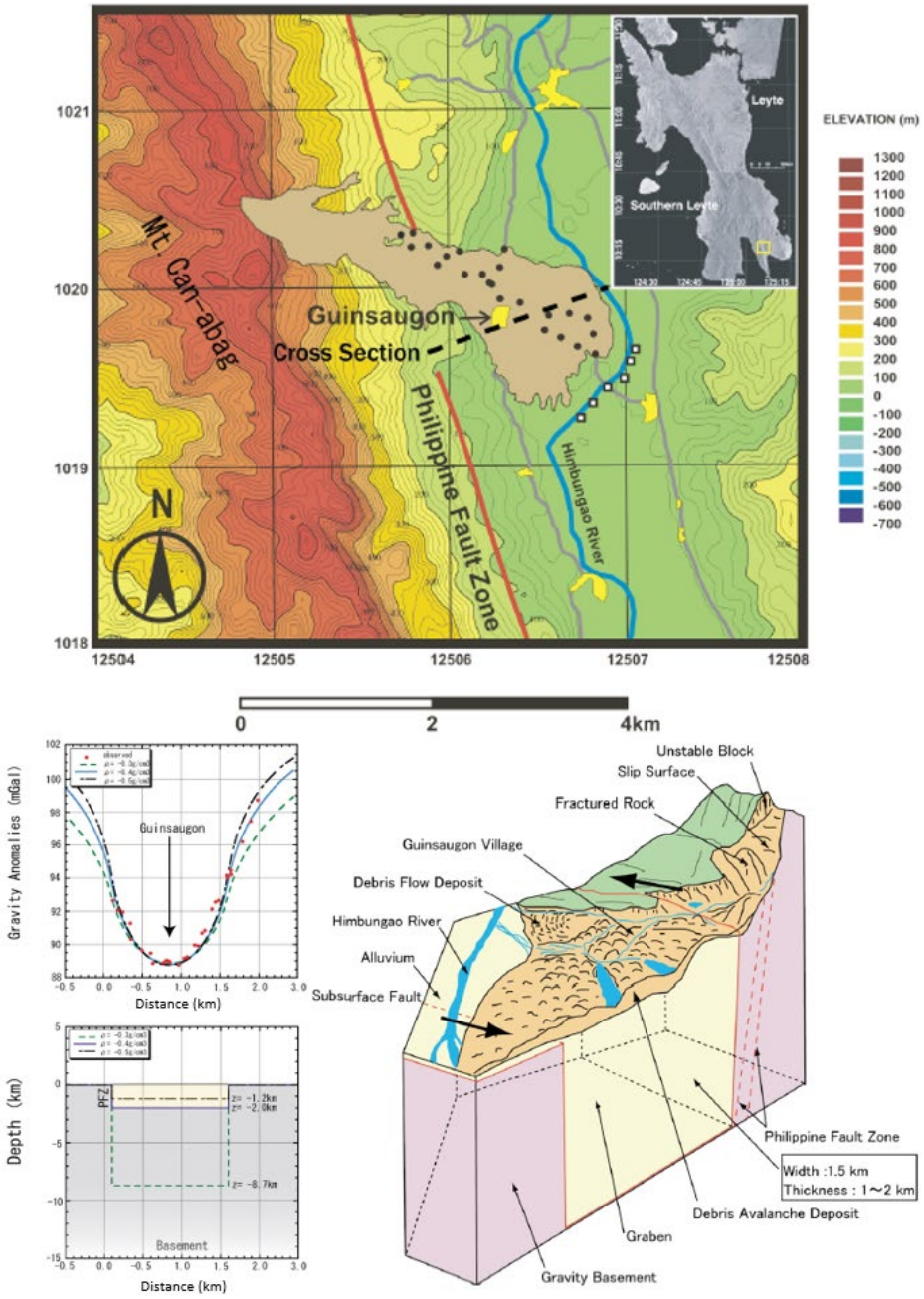

Figure 2.5. Field map, graphical cross section, and final Bouguer anomaly measurements across a profile spanning the southern section of the Guinsaugon landslide. The model uses the structural relationship between a graben and the basement rock to account for the recorded values. Modified from Makino 2007.

(Makino 2007). Alum Rock landslide Bouguer anomaly values for both profiles and a cross section of one of the profiles are displayed in Figure 2.6. Makino and Brooke saw Bouguer anomaly trends that run counter to the other. While Makino recorded a trend with low Bouguer trends in the center of the slide, Brooke noted an increase in Bouguer anomalies at the center of the slide relative to the edges. Although Bouguer anomaly analysis on data sets collected on the Canary Islands ultimately serves a different purpose

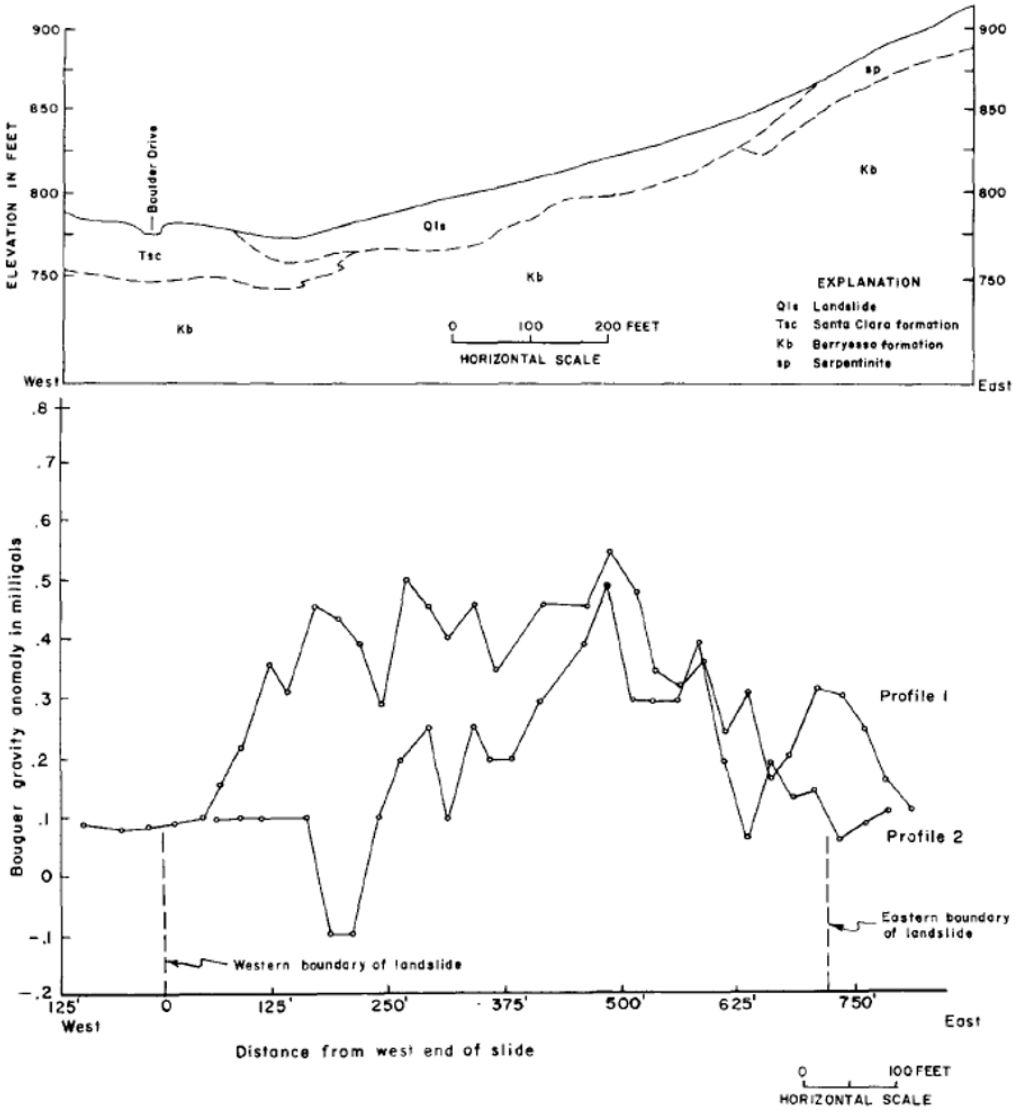

Figure 2.6. Cross section and Bouguer anomaly profiles taken along closely aligned profiles spanning the Alum Rock landslide. The cross section displayed is matched to Bouguer anomaly profile one. Gravitational highs were detected on the interior of the slide and returned to lower values at the estimated slide boundaries. Modified from Brooke 1973.

than in either of the previous two studies, the application of gravity traverses serves as a useful proxy for estimating possible subsurface material properties and shape of subsurface structures. Non-uniqueness of the gravity data does serve as a barrier to complete analysis, but when coupled with secondary data sets and surficial observations, modeling can be realistically constrained (Carracedo 1996). For example, Bouguer anomalies calculated from gravity data collected at the Canary Islands shows that there are differences in distribution of similar Bouguer values on structurally matured versus young volcanoes. By pairing this data with the maps of the archipelago, Carracedo is able to argue for the existence of and orientation of rift zones by identifying the shifts in gravitational acceleration when crossing these zones. This allows Carracedo to effectively explain the positioning of landslides throughout the Canary Islands while also providing a mechanism for slope failure and subsequent mass wasting. Gravimetric techniques can also be useful in detecting changes on landslides over time (Del Gaudio 2000). Del Gaudio found that by observing the Senerchia landslide in Southern Italy over the period of seven months, shifts in the slide's thickness, fissuring of weakened material in the subsurface, or the movement of fluids over time could be detected by gravity surveys (Del Gaudio 2000). By examining locations with higher anomaly values, it is possible to determine areas of potential water saturation, material contrast, or variable thickness, which can be used to provide insight on the characteristics of the slide, especially when measurements are recorded during multiple seasons (Brooke 1973). This is only true, however, with the assumption of constant volume in the system. When combining the data with satellite imagery of tension troughs, it could be possible to partially determine areas of localized collection or localized evacuation of fluid on or

along the sliding surface respectively. Although volcanic bodies could potentially be detected on the PBL with a gravimeter, the instrument was deployed with the intent of recording the Bouguer anomaly contrast between the edge and interior of the slide well as the signal closer to the slide scarp. Two gravity profile lines were planned; one line with an approximate length of 1000 meters was traversed across the southern section of the slide and the second line with an approximate length of 250 meters was oriented along the northern section of the slide. Deployment locations were spaced such that a point was collected every 50 meters on the southern line and every 23 meters on the northern line. All data points were shot with a total station for referential elevation data, since locations of monuments on the interior of the slide were unknown or the locations were known to be out of place. Detailed measurements of elevation differences are required to be able to carry out Free Air and Bouguer corrections on the gravity measurements. Handheld GPS data points were collected at each of the sampling locations. Tidal and instrumental drift corrections were performed on the dataset using a series of base station measurements acquired at the beginning of and at the end of the experiment. Latitudinal corrections were then applied to the dataset, followed by the application of a Free Air correction and Bouguer corrections to the data. Relative uniformity of terrain was assumed since line span was relatively short and the nearby hillslope topography, slope gradient, and material were observed to be generally homogenous and consistent across the entirety of both profiles. Closely proximal terrain might have influenced data collection on up to four data points, including the base station measurements. The corrected Bouguer anomaly gravity values were then plotted against their lateral positions on the profile line,

with the beginning of each line starting on the easternmost deployment position and ending on the westernmost position.

2.3. Ground Penetrating Radar Methodology:

GPR surveys are typically utilized in urban or shallow sedimentary settings to identify or confirm the location of shallow subsurface features such as buried piping and objects. GPR can also identify interfaces, a property that made it potentially relevant in this study. Ideally, GPR devices are ideally deployed on sites where the site's subsurface is clay-poor, relatively dry, exists as consolidated sediment or hard rock, where it is easy to consistently couple the GPR unit with the ground across the traverse, and where the features of interest reside within a relatively shallow range depth, depending on the frequency of the emitting antenna (Lissak 2015). An example of the possible detection of a hollow colluvium space as detected by GPR is presented in Figure 2.7 An example of the Cirque Des Graves in France landslide surveyed by GPR, as well as the processed GPR sections adapted from Lissak's work are presented in Figure 2.8. Additionally, GPR can be utilized to detect the presence or absence of landslide blocks, hollow colluvium spaces, and the boundary of landslides if the slides themselves are small or the contrast between the edge and interior of the slide is significant (Sass 2007). Ground penetrating radar

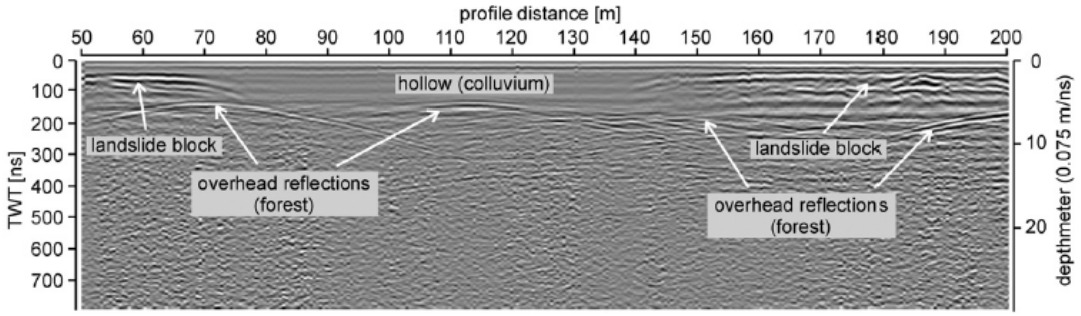

Figure 2.7. Processed section of the GPR data collected by Sass at the Öschingen landslide. Estimated locations of slide blocks, colluvium hollows are shown as well as the obfuscating signals of overhead reflections caused by trees or other canopy cover. Adapted from Sass 2007.

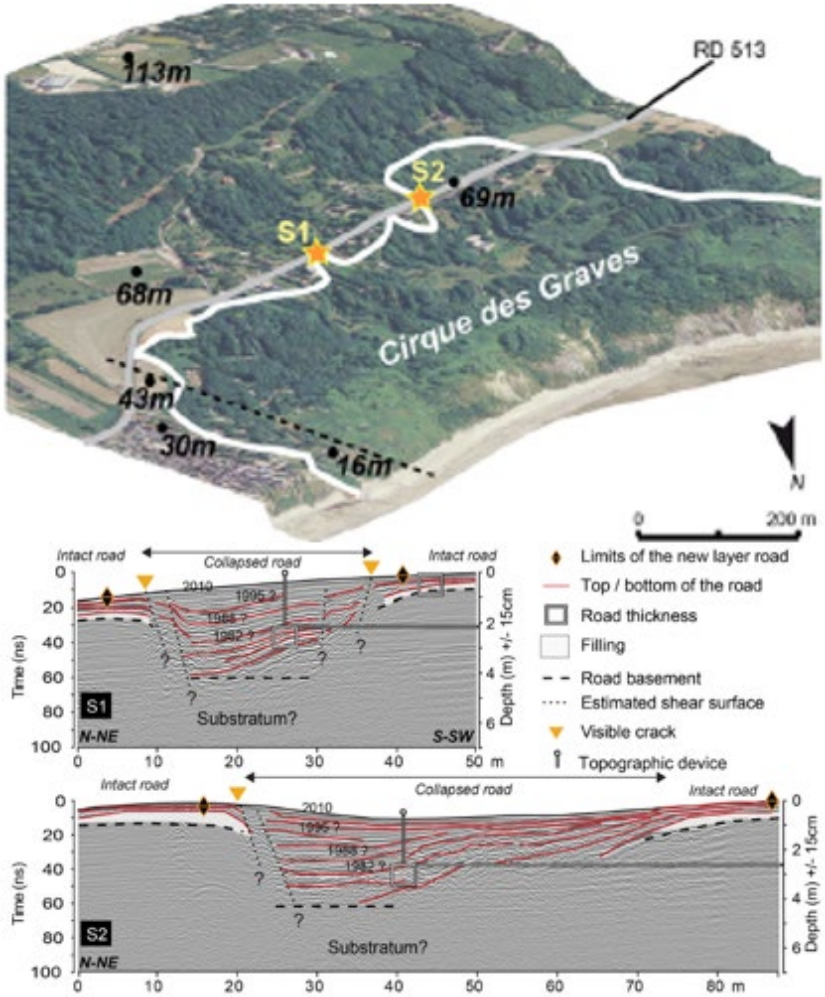

Figure 2.8. Map showcasing the location of the GPR survey and the processed GPR data collected along the road bordering the Cirque des Graves. Additional work was done to mark the boundaries of the landslide as well as the successive repaving events performed during road maintenance over time. The top profile is taken at S1 and bottom is taken at S2. Modified from Lissak 2015.

surveys were executed along several trails spanning the field site and on the supposed location of what used to be Ishibashi Lake. Calibration was performed for mixed alluvial sediments and a targeted depth range 5 to 15 meters. For all surveys, lateral calibration distance was approximately 25 meters. During data collection, several profiles were recorded and saved from each experiment. This was done explicitly to simplify data processing and analysis. Collected profile data were extracted from the GPR computer to another device, where it was then processed using RADAN software. Profile starting and ending locations were also recorded. Profiles were then compared against existing maps,

borehole data, and shallow cross sections. Ground penetrating radar as compared to other geophysical imaging techniques, is one of the fastest and easiest ways to image sedimentary layers, archaeological sites of interest, and to map and/or confirm the locations of shallowly positioned subsurface utilities and items. Because of these strengths, GPR was assumed to be an effective choice for imaging the sliding surface of the PBL because the sliding plane and the material below this plane would possess material characteristics substantially different from the overlying slide material.

2.4. Magnetometry Methodology:

Magnetic methods can be applied to detect susceptibility contrasts between bedrock and overlying sediment as well as depth to magnetic features. Although measurement of total magnetic intensity is not typically used to determine physical characteristics of landslides, magnetic methods are occasionally applied. Magnetic susceptibility surveys performed on the landslide deposits along the Tsurukawa Fault Zone revealed that magnetic surveys can reliably detect material contrasts and can be used in rudimentary subsurface modeling (Kosaka 2000). Magnetometer profiles were carried out on the PBL along the trails spanning the field site. In cases where metal culverts, pumps, piping, signage, or other metallic features were present close to the profile line, notes were made so that removal of anomalous data collected during time in proximity to those items could be undertaken. Although draft maps of magnetic data were created in the Oasis-Montaj software and in ArcMap, sampling limitations in the field did not allow for kriging, nearest neighbor sampling, or other raster interpolation methods to be performed with computer processing. Because the data could not be used to synthesize a contour map, individual profiles were generated from the raw data instead. The data were then plotted on a series

of charts comparing magnetic field strength along profile length. Each data point was recorded with a GPS quality and recording quality metric. Points defying the perfect score on both metrics were cut from the data set. Statistical metrics were calculated and used to determine quartile distributions for each respective profile. Major and minor outlier bounds were calculated from the median, upper and lower quartiles, and the interquartile range values. The outlier bounds were used to establish relative competence of the points contained in the data set but were not used to remove data points. Outlying points on each profile were compared to their geographic positions on the field site map to verify whether the anomalous field strength values observed could be attributed to either natural structures or man-made installations.

2.4.1. Magnetometer Limitations:

In magnetic surveying experiments it is typical to traverse the study area using a system of straight-line traverses with perpendicular connections or regular zipper patterns. This provides the experimenter with the opportunity to statistically interpolate between data points to create contour maps and raster maps. As part of the permitting process however, an agreement was reached between myself and the Palos Verdes Land Conservancy (PVPLC), the primary group in charge of maintaining the trails and enforcing safety regulations on the slide. Integral for permission to experiment on the slide was the agreement that experimentation would be limited only to marked trails. As important as the permitting restrictions was the morphology of the field site. The tension troughs and substantial vegetation make it difficult to traverse the trail-free sections of the slide with the magnetometer. Because of these factors, data collection was limited to the trails only. The lateral expanse between the data points was too great to statistically interpolate

between data points. Contour maps generated from the data show significant lateral striping that likely doesn't represent the natural characteristics of the landslide. Instead, locations of interest were broken down into subsequent profiles and then analyzed individually. Examining individual profiles limits the scope of the overall analysis. Signals that may have been statistically insignificant on a map appear pronounced on the limited profile. Additionally, any signals from relevant subsurface bodies on the slide interior may not be detected because of the physically limited sampling range enforced by the PVPLC. Additionally, contrasts in magnetic susceptibility between slide sediment and sedimentary rock are typically minor and are likely not apparent in the magnetic signal. Volcanic units have been mapped in nearby areas but were not mapped within the surveyed area.

3. RESULTS:

Data produced by the experiments were processed and tabulated using a variety of software and techniques. In some cases, observations were determined to be either reliable or not suitable for interpretation through a combined application of criteria, instrumental metrics, and statistical analysis. Final results were then catalogued in charts or used to generate maps. Data and results not included in the body of the text are available in Appendices A and B.

3.1. Spectral Ratio Results:

Ambient noise waveform data collected at numerous locations across the site and processed in Geopsy yielded spectral ratio curves. Final curves for all sites can be found in Appendix A. Figure 3.1 shows an example curve generated from ambient noise data. Data collection locations and peak frequencies as determined from the spectral ratio curves for each

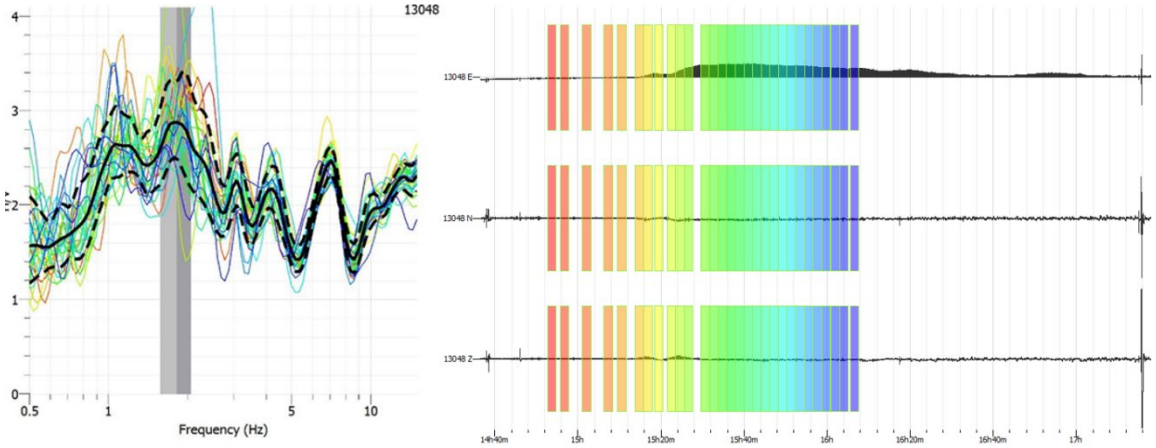

Figure 3.1. The spectral ratio curve and windows for each station displayed correspond to ID 1 in Figure 3.2. Window length used for processing was 125 seconds and the selected windows for the three components are shown in the right panel. Time elapsed is shown on the bottom axis. After checking the curve with the SESAME criteria, it was found that the curve was reliable and did possess a clear peak. The H/V ratio amplitude on the y-axis is plotted against the frequency on the x-axis. The grey bars show the upper and lower bounds of the standard deviation of the peak frequency and the center line between the two corresponds to the peak frequency. The dotted lines represent the standard deviation of the amplitude of the curve at each point along its extent. The colored lines track the H/V ratio amplitude at each frequency as recorded within selected time windows. Hotter colors represent data from time windows early during the deployment and cooler colors represent data collected later in the deployment.

recording site are displayed in Figure 3.2. The example curve provided exhibits a variety of notable features. Firstly, the spectral ratio curve contains multiple peaks. Although the

Figure 3.2. Map generated in Esri's ArcMap 10.6.1 software. HVSR peak frequencies determined for each station are displayed. Warmer colors represent higher peak frequencies while greener, cooler colors represent lower peak frequencies. The labels on each point are the station ID. PVDS marks Palos Verdes Drive South.

peak with the highest amplitude was selected, the other peaks could represent resonance with other subsurface boundaries presenting a lower acoustic impedance contrast. The curve is reliable according to the SESAME criteria: the peak frequency is sufficiently large compared to the length of the windows sampled from the seismic data, there is a substantial number of significant cycles as a function of the peak frequency, window length, and number of windows selected, and the standard deviation of the amplitude is small within a range of the peak frequency. The peak is clear according to the SESAME criteria: the amplitude for a frequency within a range less than the peak frequency is much less than the peak amplitude, the amplitude for a frequency within a range greater than the peak frequency is much less than the peak amplitude, the peak amplitude is significantly large, the peak should be reproducible within five percent correspondent to average plus or minus one standard deviation, the standard deviation of the peak frequency is less than a given threshold value for the applicable range within which the peak frequency falls, and that the standard deviation of the amplitude is lower than a given threshold value for the applicable range within which the peak frequency falls. Figure 3.3 displays two additional curves.

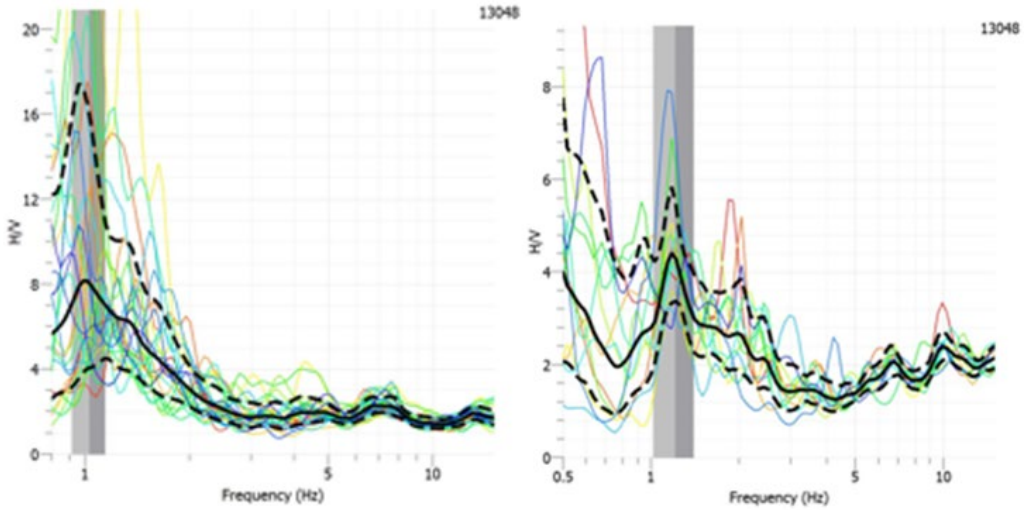

Figure 3.3. The curves depicted were gathered on 12/3/2018. The left curve corresponds to ID 5 and the right curve corresponds to ID 14. Both curves are reliable and possess clear peaks. Note that both amplitude and frequency scale vary.

Both curves were created from data recorded at the same location, but the data used for station five was recorded before the start of the rainy season and the curve for station fourteen was generated from data recorded after the onset of seasonal rains. The curves are reliable and possess clear peaks according to the SESAME criteria. The amplitude of the peak frequency determined at station five is greater than the amplitude of the peak frequency determined at station fourteen. Therefore, the results for data collected during dry and wet seasons on the field site did show variation, indicating either a change in shear wave velocities above the interface and/or a change in the depth to a significant change in material properties due to ponding of water above the slide plane.

Spectral ratio data were subjected to multiple criteria to determine the reliability of curves and clarity of peaks of the collected data. The criteria are important because they can be used to determine the reliability of our measurements. Essentially, a reliable curve is one that should be reproducible within a small margin of error at the sampling location. Simply put, a reliable curve accurately represents the site response characteristics of the sampled location at the time of the measurement and can be reliably used to make determinations about the sampled location. Determining whether a peak is clear or not is also important because its status reveals relevant information about the sampling site. It is important to note two things when testing a peak for clarity. Firstly, a clear peak that results from an unreliable curve is not useful for making inferences about site characteristics. Secondly, a peak that is unclear, or a curve that is generally flat, does not invalidate the spectral ratio curve. Rather it reveals information about the site such as: the lack of a strong resonance with an acoustic boundary, the subsurface boundary of interest might be broken up or steeply sloped at the sampled location, or the boundary of interest might be very close

to the surface at the sampling location. All of the curves passed the three reliability criteria, but five out of the seventeen total peaks failed more than one criterion for a clear peak. The peaks that failed more than one criterion for a clear peak were classified as unclear. One curve passed every criterion and eleven curves passed all but one criterion. The criterion results for each of the curves are detailed in Table 3.1. Figure 3.4 depicts a curve that exhibited a clear peak and reliable curve and a second, reliable curve with a clear peak and peak frequency pairs are plotted in Figures 3.5 and 3.6.

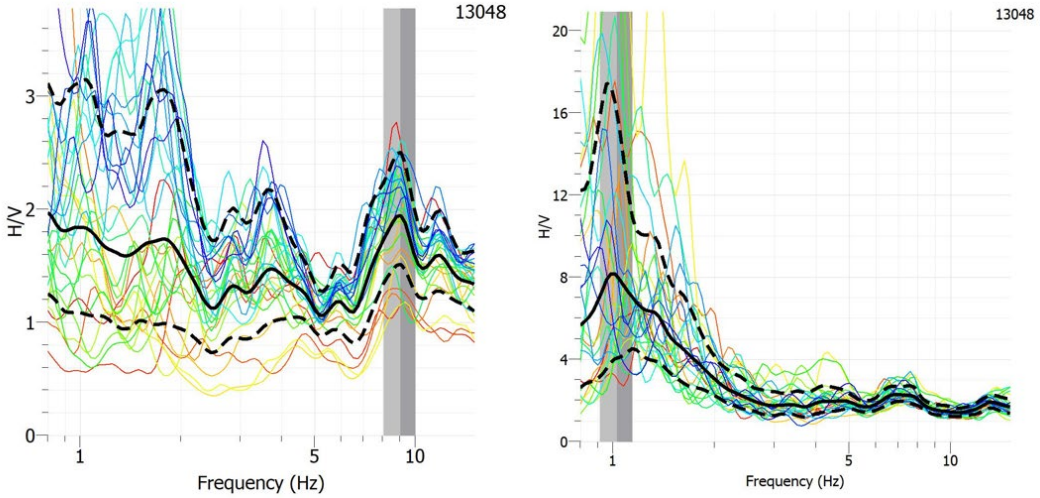

Figure 3.4. Spectral ratio curves 16 and 5 are shown on the left and right respectively. Curve 16 possesses a clear peak and is reliable while 5 possesses a clear peak and is reliable. Colors, lines, and bars as in Figure 3.1.

Peak frequencies across all stations ranged from 0.68 Hz to 13.5 Hz. Depth ranges determined through a simple quarter wavelength function as explained in section 2.1 indicate that the interface responsible for generating this peak, which we interpret here as the slide plane across this area exists at a range of approximately surficial exposure to 53 meters at depth. Wet season peak frequencies were generally higher than the dry season peak frequencies, but this was not always the case. Most of the data points collected exhibited a possible trend with the introduction of rainwater leading to a shift to a higher H/V spectral ratio peak frequency. Data pairings from sampled sites during times of rain

Table 3.1. Criteria results tabulated for each data point. Green boxes indicate passing and red boxes indicate failure. Curves fail the clarity test if they fail two or more criteria.

ID↓/Criteria →	Date_Collected	i	ii	iii	i	ii	iii	iv	v	vi	Reliable Curve (Y/N)	Clear Peak (Y/N)
1	10_17_2018	Y	Y	Y	N	Y	Y	Y	Y	Y	Y	Y
2	10_17_2018	Y	Y	Y	N	Y	Y	Y	Y	Y	Y	Y
3	10_18_2018	Y	Y	Y	Y	Y	Y	Y	N	Y	Y	Y
4	10_19_2018	Y	Y	Y	Y	Y	Y	Y	N	Y	Y	Y
5	10_19_2018	Y	Y	Y	N	Y	Y	Y	Y	Y	Y	Y
6	10_22_2018	Y	Y	Y	N	Y	Y	Y	N	Y	Y	N
7	10_22_2018	Y	Y	Y	N	Y	Y	Y	N	Y	Y	N
8	12_3_2018	Y	Y	Y	Y	Y	Y	Y	N	Y	Y	Y
9	12_3_2018	Y	Y	Y	Y	Y	Y	Y	Y	Y	Y	Y
10	12_9_2018	Y	Y	Y	Y	Y	Y	Y	N	Y	Y	Y
11	12_9_2018	Y	Y	Y	Y	Y	Y	Y	N	Y	Y	Y
12	12_10_2018	Y	Y	Y	Y	Y	Y	Y	N	Y	Y	Y
13	12_10_2018	Y	Y	Y	Y	Y	Y	Y	N	Y	Y	Y
14	12_2_2018	Y	Y	Y	N	Y	Y	N	Y	Y	Y	N
15	12_2_2018	Y	Y	Y	N	Y	Y	N	N	Y	Y	N
16	2_27_2019	Y	Y	Y	Y	Y	Y	Y	N	Y	Y	Y
17	2_27_2019	Y	Y	Y	N	N	Y	N	Y	Y	Y	N
Green Indicates Pass (Y)												
Red Indicates Fail (N)												

showed an increase in frequency which is typically indicative of a shallower depth at the sampling location but could also include other factors. Although drawing the simple conclusion that a change in depth occurred at the location after rain is likely inadequate, the data could suggest that an acoustic boundary has been imaged at a shallower depth. It is possible that water collected on the sliding surface could be responsible for this change. During the dry season, data collected represented the resonant frequency of the column of the landslide material above the sliding surface. With the introduction of water during the rainy season, the fluid generates a new acoustic barrier during the wet season. This could result in the shifting of the recorded peak frequency to a higher frequency and/or the recording of two substantial peaks where there would have previously been one. The addition of water to soils typically slows down the velocity of S-waves (Chen 2020), which would result in a lower measured peak frequency for a boundary at the same depth. Table 3.2 displays a variety of information pertaining to each data point and illustrates point pairs with color delineation as well as the frequencies that were plugged into the 1D quarter wavelength function, $H = V_s/4f_0$ where V_s chosen was 145 meters per second, H was the depth to the resonant boundary, and f_0 was the peak frequency. The justification for the use of this seismic velocity is explained in section 2.1. The curve generated from data collected

at point nine exhibits the potential emergence of a second peak in addition to the original peak after rainfall. The curve generated from wet season data for point eleven also

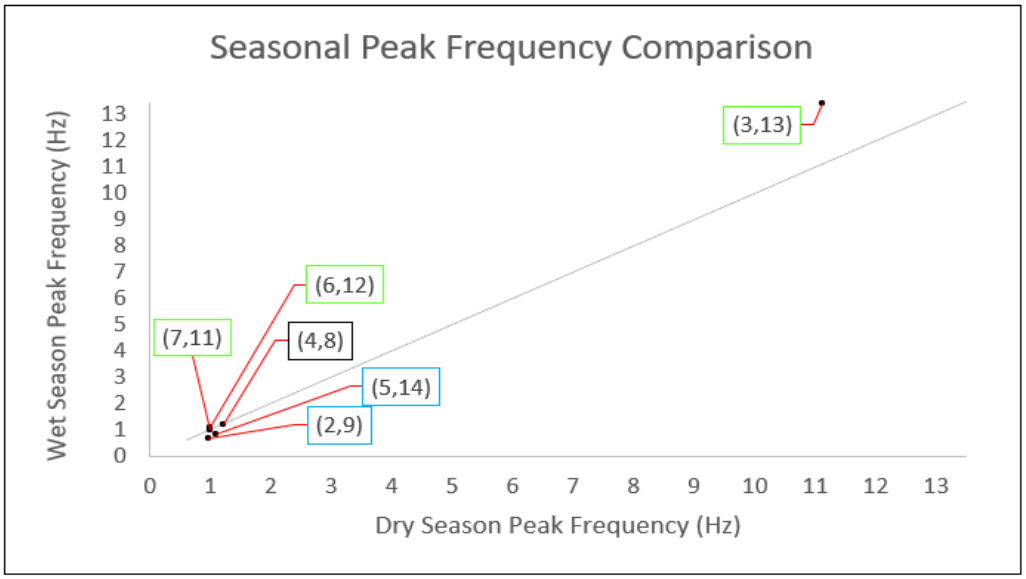

Figure 3.5. Wet season and dry season peak frequency pairs are plotted. Pairs with equal frequencies recorded during both seasons would plot on the line. Points are labeled with the station ID pairs that correspond to the seasonal frequencies collected. The first number in each pair corresponds to the dry season station and is linked to the x-axis value while the second number in each pair corresponds to the wet season station and is linked to the y-axis value. Green boxes represent pairs that plot with a higher wet season peak frequency. Blue boxes represent pairs that plot with a higher dry season peak frequency. Black boxes represent pairs that plot on the line.

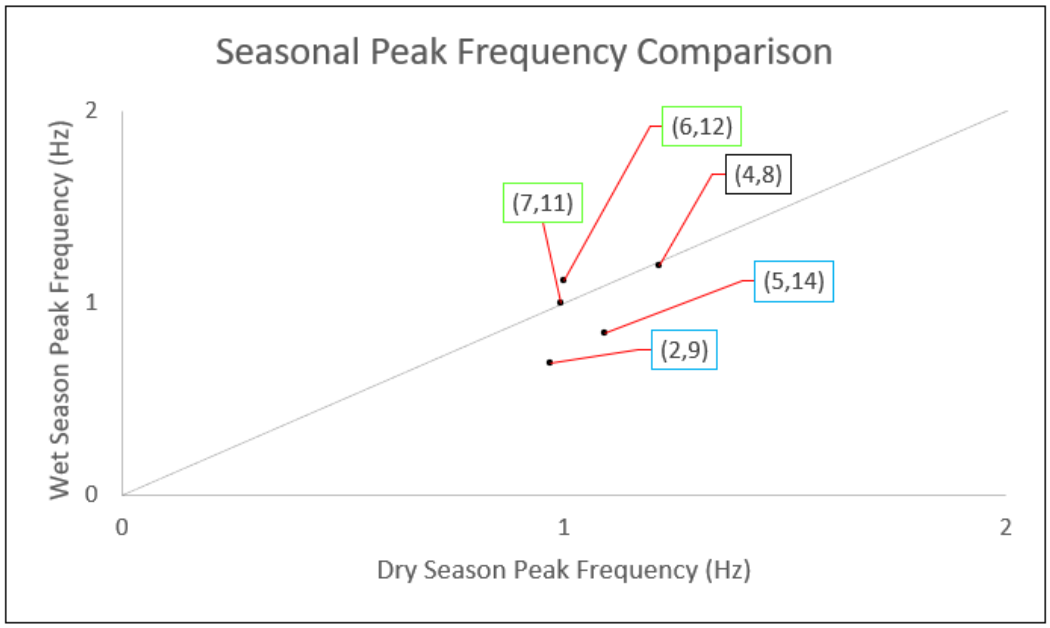

Figure 3.6. Zoomed version of Figure 3.5. Focus is on the cluster of points within the 0-2 Hz x and y coordinate range. The line and the colored boxes are representative of the same characteristics as described in the caption for Figure 3.5.

Table 3.2. Peak frequency, peak amplitude, and depth estimates as determined from the spectral ratio curves. Date collected, identification number (ID), latitude and longitude coordinate pairs in decimal degrees, peak frequency, approximate depths in meters and feet, and the peak amplitude of each curve are displayed. Points reflecting data sampled at the same location are color coded. IDs with grayscale are not paired to any point and represent solo observations.

Date Collected	ID	Latitude	Longitude	Peak Frequency (Hz)	Approximate Depth (m)	Approximate Depth Feet (ft)	Peak Amplitude (H/V)
10_17_2018	1	33.74071	-118.3599	1.82338	19.88066119	65.2085687	2.85
10_17_2018	2	33.74219	-118.35968	0.970059	37.36886107	122.5698643	3.39
10_18_2018	3	33.7428	-118.35986	11.1283	3.257460708	10.68447112	2.28
10_19_2018	4	33.7411	-118.3604	1.21547	29.82385415	97.8222416	3.51
10_19_2018	5	33.7412	-118.3621	1.09236	33.18503058	108.8469003	8.05
10_22_2018	6	33.742	-118.3598	1.00163	36.19100866	118.7065084	2.19
10_22_2018	7	33.74558	-118.36174	0.993722	36.47901526	119.65117	3.58
12_3_2018	8	33.741111	-118.36047	1.1952	30.32965194	99.48125837	2.92
12_3_2018	9	33.74218	-118.35962	0.682232	53.13441762	174.2808898	3.78
12_9_2018	10	33.74055	-118.3613	1.09364	33.1461907	108.7195055	3.19
12_9_2018	11	33.74552	-118.36173	1.00076	36.22247092	118.8097046	5.42
12_10_2018	12	33.74203	-118.35982	1.11774	32.43151359	106.3753646	2.11
12_10_2018	13	33.74288	-118.35965	13.4309	2.699000067	8.85272022	2.53
12_2_2018	14	33.74118	-118.362165	0.84523	42.8877347	140.6717698	7.94
12_2_2018	15	33.74147	-118.36215	1.04204	34.78753215	114.1031054	4.22
2_27_2019	16	33.74218	-118.36115	9.03103	4.013938609	13.16571864	2.01
2_27_2019	17	33.74143	-118.362343	13.5244	2.680340718	8.791517553	2

exhibited the strengthening of a secondary peak that was weakly present on the curve generated from the dry season data collected at point seven. The secondary peak increased in amplitude, but did not broaden significantly. This also partially corroborates the claims and observations by Ehlig in 1987, that the dewatering rate is slow at the sliding surface and thus contributes to the continued motion of the slump towards the sea. Ehlig's sampling of soil material indicates that substantial quantities of bentonite, a highly water-impermeable clay, are present on the sliding surface. Bentonite, a material often used in groundwater monitoring wells because of its ability to inhibit fluid flow, would create an effective seal causing water to flow along and above the bentonite interface and not within it. Although data collected is reasonably explained by the existence of a bentonite layer, the data point pairings of station two with nine and station five with fourteen, collected during the dry and rainy seasons respectively do not provide evidence supporting this case. Typically, the difference between the wet and dry season peak frequencies determined at most of the stations exhibit an increase in peak frequency after precipitation events. For example, the peak frequency determined at station three is lower during the dry season is lower than the peak frequency determined at station thirteen during the wet season.

However, the typically observed trend towards a higher peak frequency after rainfall on the site is contrary to the peak frequencies recorded at each of the aforementioned pairs. During the dry season, the frequency recorded at points two and five were higher than the recorded frequencies at points nine and fourteen for each pairing. The frequencies recorded at point pairs four and eight as well as seven and eleven were close to equal. However, we can conclude that we observed significant changes in the spectral ratio curves at most sites between observations before and after rainfall events, indicating that the presence of water in the subsurface has a measurable effect on the physical properties of the material above the slide plane.

3.2. Gravity Results:

Two gravity profiles collected at the north and south ends of the field site using a LaCoste and Romberg gravimeter were processed and the final Bouguer anomalies were plotted against profile length. Figure 3.7 shows a map detailing the locations of the gravity anomaly recording points. The Bouguer anomaly values for each point were generated by first determining instrumental drift present throughout the duration for each experiment. The overall experiment duration was recorded and time stamps collected for each point. The drift correction was applied to each point based on how much time had elapsed at the time of recording since recording initially at the base station. The drift modified values were then corrected further with a latitude correction, which was required because gravitational acceleration increases as a function of latitude from the equator to the poles. The relative elevation of each point was determined by finding the difference between the elevation recorded at each point and the elevation recorded at the base station of the gravity line, as measured by total station. These elevation differentials are the elevations relative

Figure 3.7. Map detailing the Bouguer anomalies plotted at the measurement sites. Warmer colors are indicative of greater Bouguer anomalies and cooler colors are indicative of lower Bouguer anomalies. PVDS marks Palos Verdes Drive South.

to the base stations and were used to calculate the Free Air anomalies for each point. These anomalies are relative, not absolute, values because only relative gravity and elevation measurements were collected. The final Bouguer anomaly values were then derived from the Free Air anomaly values using a density of 1.773 grams per cubic centimeter. Charts

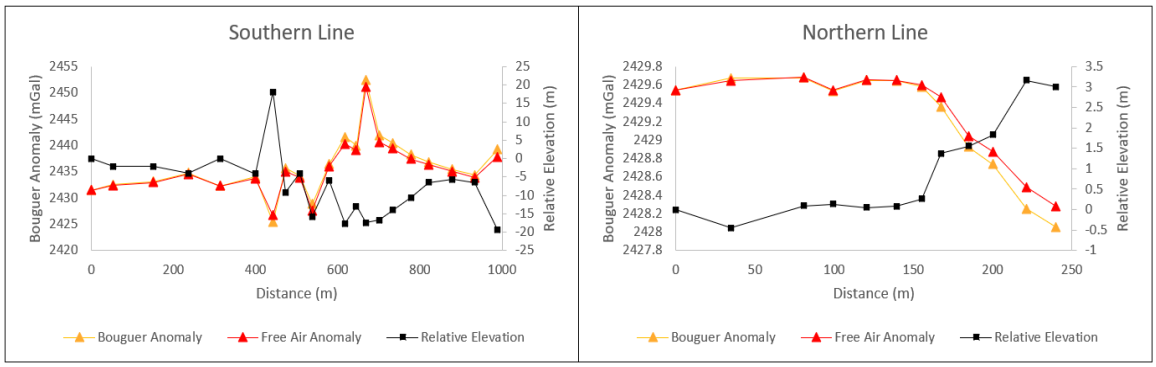

Figure 3.8. Profile graphs of the Bouguer anomalies, free air anomalies, and relative elevation measurements for the northern and southern lines. The Bouguer anomaly values are represented by the orange triangles and the free air anomaly values are represented by the red triangles. The relative elevation is represented by the black squares. Note the difference in y-axis scale.

of the profiles correspondent with Figure 3.7 are illustrated in Figure 3.8. The density value was selected with knowledge of local geology and approximates the density of sedimentary rocks that are found around the field site (Ehlig 1987). The values used for the generation of the map are detailed in Table 3.3. Distances between points were determined by using

Table 3.3. Table containing the calculated free air and Bouguer anomaly values as well as the relative elevation values for each survey point relative to the base station for each line.

ID	Latitude	Longitude	Bouguer Anomaly (mGal)	Distance (m)	Relative Elevation From Base (m)	Free_Air_Anomaly (mGal)	
1	33.7368	-118.3562	2431.479	0.0	0.00	2431.479	
2	33.7372	-118.3565	2432.503	53.7	-2.18	2432.341	
3	33.7379	-118.3571	2433.113	150.5	-2.21	2432.948	
4	33.7385	-118.3577	2434.789	235.8	-3.99	2434.492	
SL Base	33.7390	-118.3583	2432.291	313.9	0.00	2432.291	
5	33.7396	-118.3588	2433.983	400.2	-4.16	2433.674	S
6	33.7399	-118.3592	2425.360	442.7	18.15	2426.709	o
7	33.7400	-118.3595	2435.716	472.7	-9.14	2435.036	u
8	33.7400	-118.3598	2434.174	506.7	-4.07	2433.872	t
9	33.7401	-118.3602	2428.824	539.0	-15.80	2427.650	h
10	33.7402	-118.3606	2436.421	578.3	-5.83	2435.987	
11	33.7404	-118.3610	2441.556	617.1	-17.70	2440.240	L
12	33.7404	-118.3613	2439.993	645.0	-13.01	2439.025	i
13	33.7404	-118.3615	2452.496	668.0	-17.48	2451.197	n
14	33.7404	-118.3619	2441.910	701.5	-16.76	2440.665	e
15	33.7405	-118.3622	2440.413	733.7	-14.03	2439.370	
16	33.7405	-118.3627	2438.202	778.9	-10.57	2437.416	
17	33.7405	-118.3632	2436.812	822.1	-6.50	2436.329	
18	33.7406	-118.3638	2435.436	879.5	-5.74	2435.009	
19	33.7408	-118.3643	2434.320	933.1	-6.52	2433.835	
20	33.7407	-118.3649	2439.205	988.8	-19.38	2437.765	
NL Base	33.7445	-118.3596	2429.546	0.0	0.00	2429.546	
1	33.7447	-118.3599	2429.678	34.7	-0.44	2429.644	N
2	33.7450	-118.3603	2429.679	80.9	0.09	2429.686	o
3	33.7451	-118.3604	2429.531	99.3	0.13	2429.541	r
4	33.7452	-118.3606	2429.652	120.5	0.05	2429.655	t
5	33.7453	-118.3607	2429.646	139.7	0.09	2429.652	h
6	33.7454	-118.3609	2429.579	155.3	0.26	2429.598	
7	33.7455	-118.3610	2429.363	167.2	1.38	2429.465	L
8	33.7456	-118.3611	2428.928	184.7	1.56	2429.043	i
9	33.7456	-118.3613	2428.737	200.0	1.83	2428.873	n
10	33.7457	-118.3615	2428.252	221.3	3.16	2428.487	e
11	33.7457	-118.3617	2428.058	239.6	3.00	2428.281	

the latitude and longitude measurements, collected at each point with a GPS unit, as a coordinate pair and then determining the length of the hypotenuse connecting each

consecutive pair with the Pythagorean Theorem. Bouguer anomaly values observed on the north profile average exhibited a range of approximately 1.62 milligals and the Bouguer anomaly values observed on the southern line exhibited a range of 27.13 milligals. Greater variation in Bouguer anomaly values was observed across the substantially longer southern line than the northern line. Additionally, a strong spike in anomaly values and a trend of increasing variability in anomaly was recorded after crossing the sixth point which coincides with the boundary of the slide as mapped by other researchers. This reveals a potential edge effect similar to those observed by experimenters such as Brooke and Makino on the Alum Rock and Guinsaugon landslides respectively. The initial drop in anomaly value observed on the southern line could be attributed to an increase of the thickness of the sliding material while the substantial jump in the observed anomaly could be explained by the multiple layers of asphalt from regular road resurfacing projects at that location on Palos Verdes Drive South.

3.3. GPR Results:

All GPR profiles showed thin layering of churned material with minor dielectric permittivity differences. A map of the profiles is displayed in Figure 3.9. An unmarked version of an example profile section with a detected feature of interest and marked version of the same section is displayed in Figure 3.10. An example profile representative of the majority of data collected is exhibited in Figures 3.11. Images of all profiles can be found in Appendix B. A total of 1,300 meters of profile length were surveyed across eighteen profiles over two days. No profiles show clear detection of the sliding surface or subsurface water. In some cases, small morphological features such as recently filled paleo-stream channels were surveyed. It is unlikely that reflections from vegetation or other above-

ground items were detected as trees and shrubs were sparse along the survey lines. These features exist closer to the middle of the field site. No significant signals were observed with one exception. The survey of profile line R-R' showed a dielectric permittivity contrast that descended to a greater depth along the profile line. The feature was detected

Figure 3.9. Map generated in Esri's ArcMap 10.6.1 software. GPR profiles and paths are displayed as well as their respective start and end points. Profiles were recorded with alphabetical designation. PVDS marks Palos Verdes Drive South.

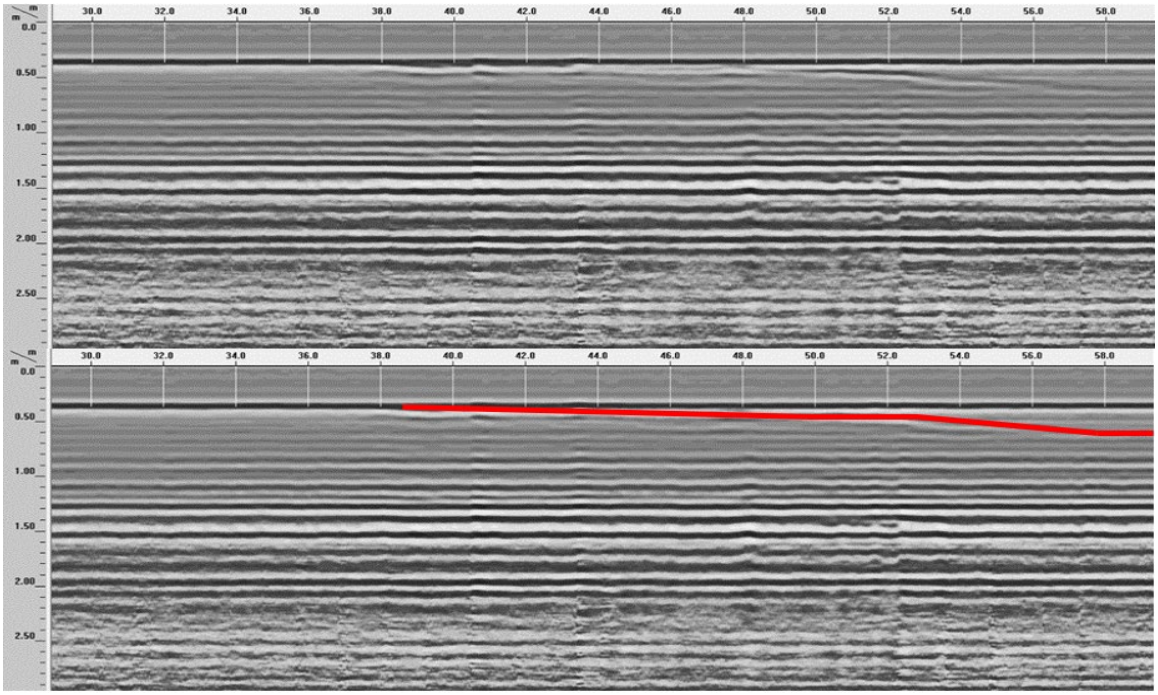

Figure 3.10. GPR profile section collected during the survey of the rumored location of Ishibashi Lake along profile R-R'. The horizontal axis of each profile is the distance of the track in meters. The vertical axis indicates the depth of the imaged features in meters. Typically, the vertical axis is displayed in nanoseconds, and depth is derived from the time difference between the emission of the radar pulse from one antenna and the receiving of the reflected signal at another antenna. Stronger reflectors are typically denoted by darker lines, but in the case seen here many of the reflections are poorly resolved with significant static. A feature of interest was detected starting approximately at the thirty-eighth meter along the traverse and descends to a depth of just over half of a meter and is demarcated from the rest of the reflections by a red line. The feature may be an old stream rill created during a prior precipitation event. The feature is undetected along the rest of the profile.

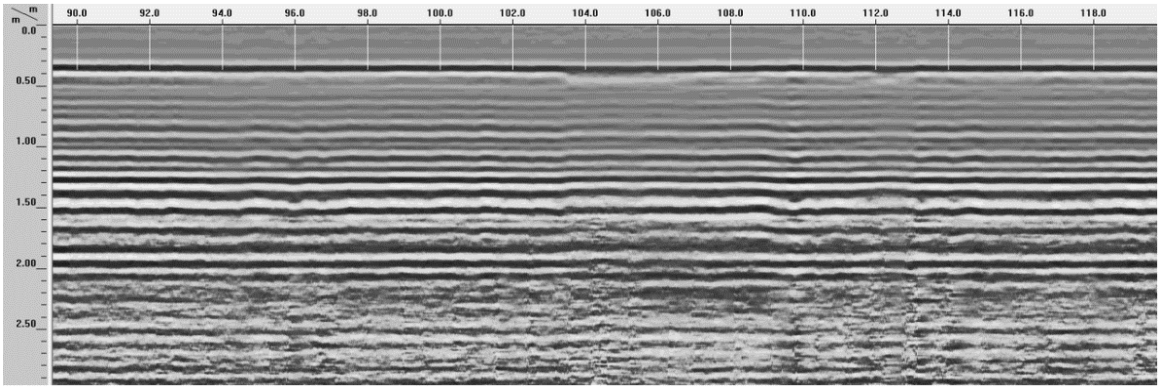

Figure 3.11. The ending section of profile R-R' is shown. The data displayed here is representative of the majority of the data collected. Very few, if any, features of interest were detected. Strong signal attenuation occurred at shallow depths while sampling all of the profiles. Coupling of the GPR unit with the ground was difficult to maintain during the experiment due to the profuse cobbles present and the undulatory nature of the coupling surface across the field area.

roughly a quarter into the traverse. Data revealed that the feature extended from closely proximal to the surface to just over half a meter in depth at its maximum.

3.4. Magnetometer Results:

Thirteen profiles were surveyed using a GEM Systems Overhauser magnetometer. The location of the profiles can be viewed in Figure 3.12. Basic quartile analysis performed

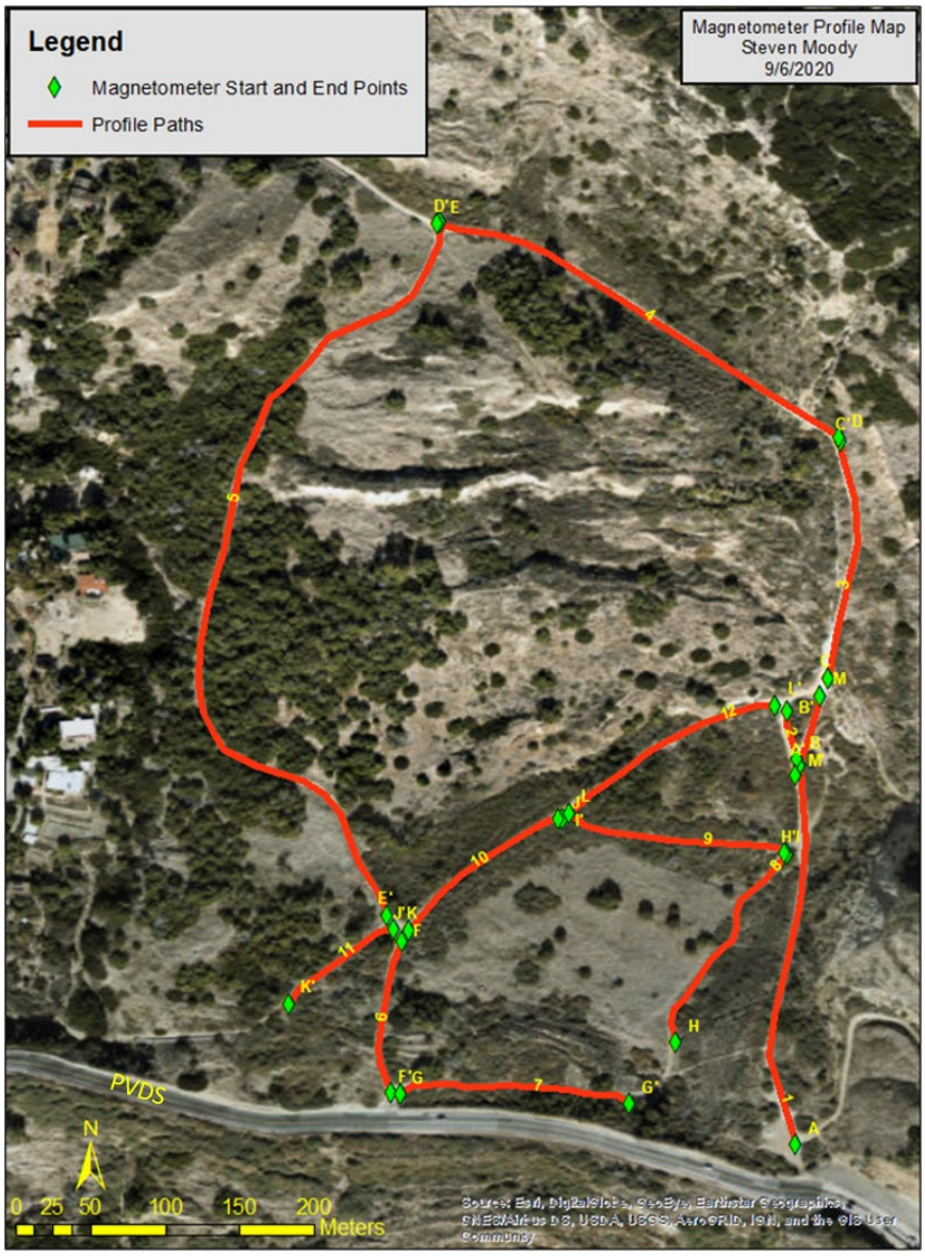

Figure 3.12. Magnetic survey profiles are numerically labeled and their starting and ending locations are marked alphabetically. PVDS marks Palos Verdes Drive South.

on each profile showed that substantial spikes exhibited in five of the thirteen profiles are statistical outliers, while eleven out of the thirteen profiles contained data points that were minor outliers. An example profile with quartile bounds is shown in Figure 3.13. Most data points did fall outside of the quartile bounds. Some points with poor quality values were

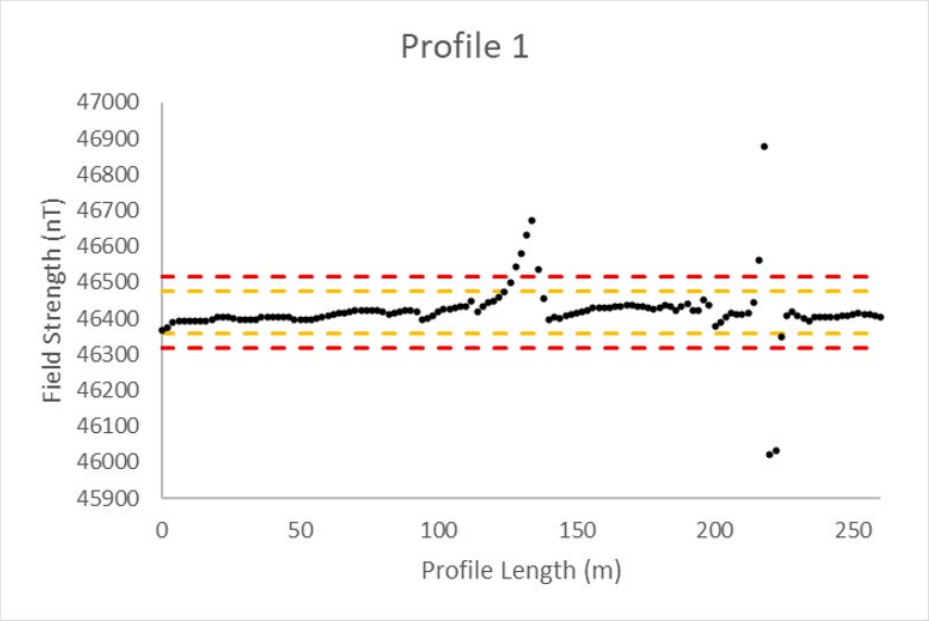

Figure 3.13. Example magnetic profile before magnetometer quality metrics were used to remove certain points. Quartile ranges for the data set are indicated by the yellow and red lines. Points falling outside both lines are major outliers while those falling in between the red and yellow lines are minor outliers.

flagged in the data and subsequently removed. Profiles generally exhibited ranges of field strength values that were typically 100 to 300 nanoteslas on the short lines with values ranging from approximately 1000 to 2500 nanoteslas on the longer lines. Field strength values generally showed minimal change over each of the profiles. The profiles after cuts were made are displayed in Figure 3.14, 3.15, and 3.16. The first profile displayed a minor drop in field strength values across the entire length. Two potentially anomalous sections exhibit significant shifts in numeric magnitude. These shifts are not the result of a numerical artifact or a single anomalous data point but are instead composed of multiple points.

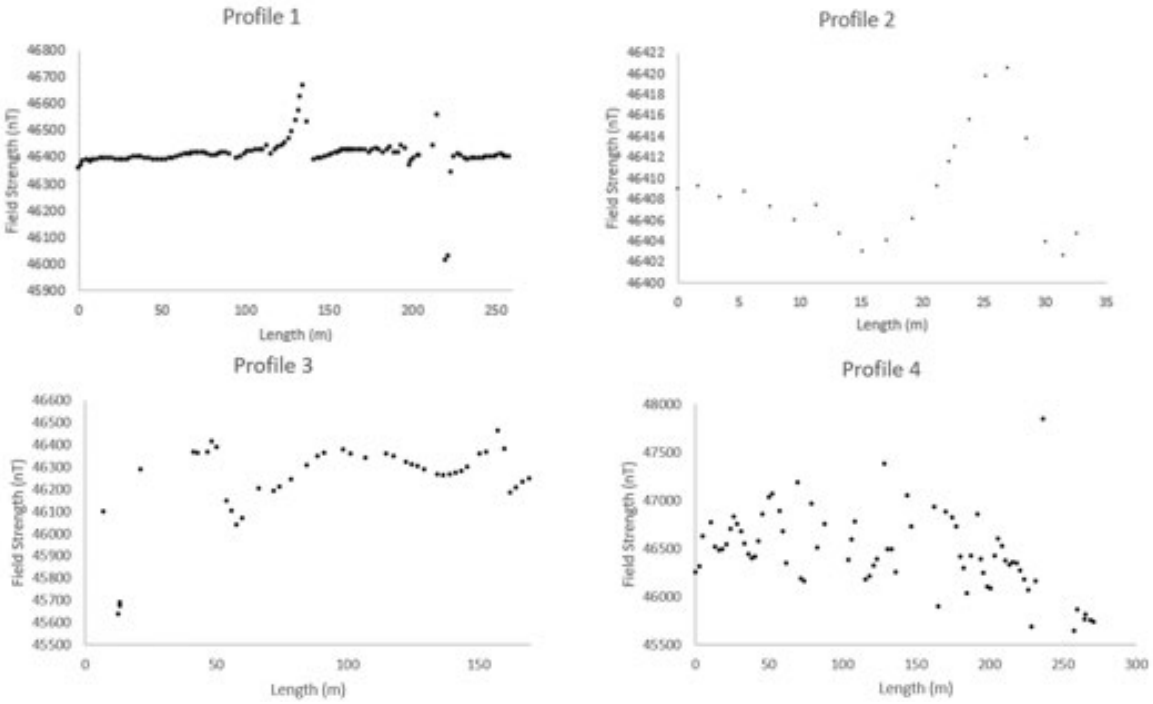

Figure 3.14. Magnetometer profiles 1-4. Profile lengths are tracked on the bottom axis. Measured magnetic field strength values are tracked on the side axis. Field strength values were measured in nanotesla. Note variation in vertical and horizontal scales.

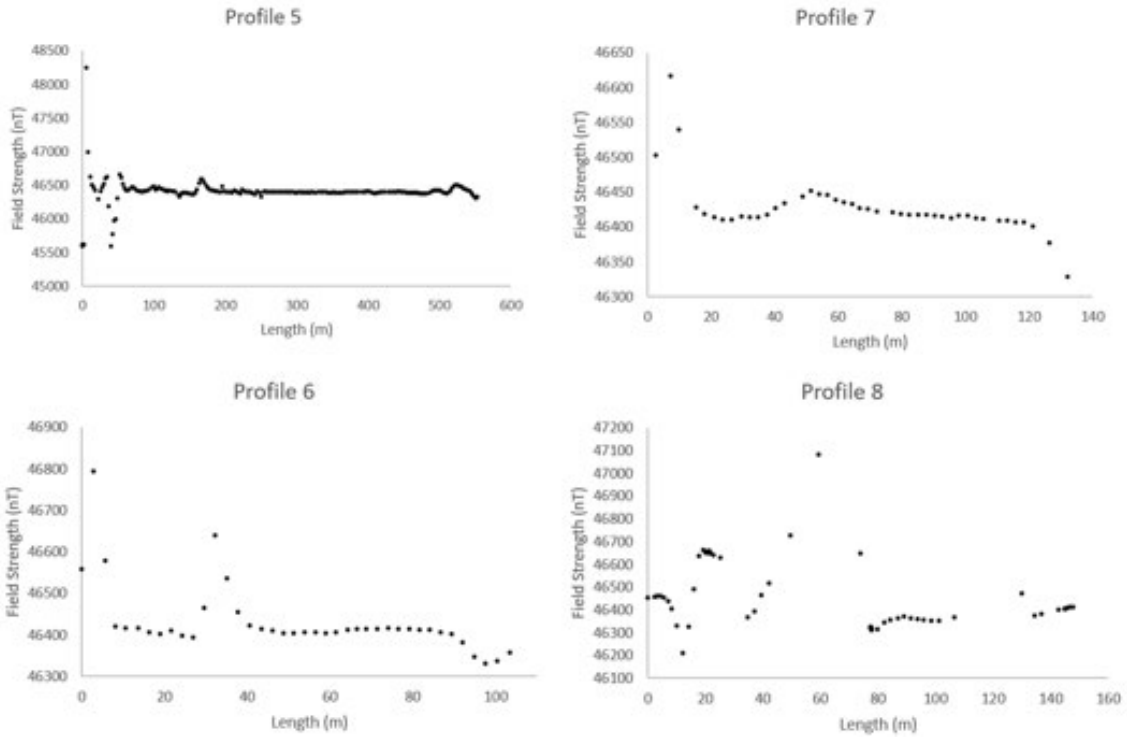

Figure 3.15. Magnetometer profiles 5-8. Profile lengths are tracked on the bottom axis. Measured magnetic field strength values are tracked on the side axis. Field strength values were measured in nanotesla. Note variation in vertical and horizontal scales.

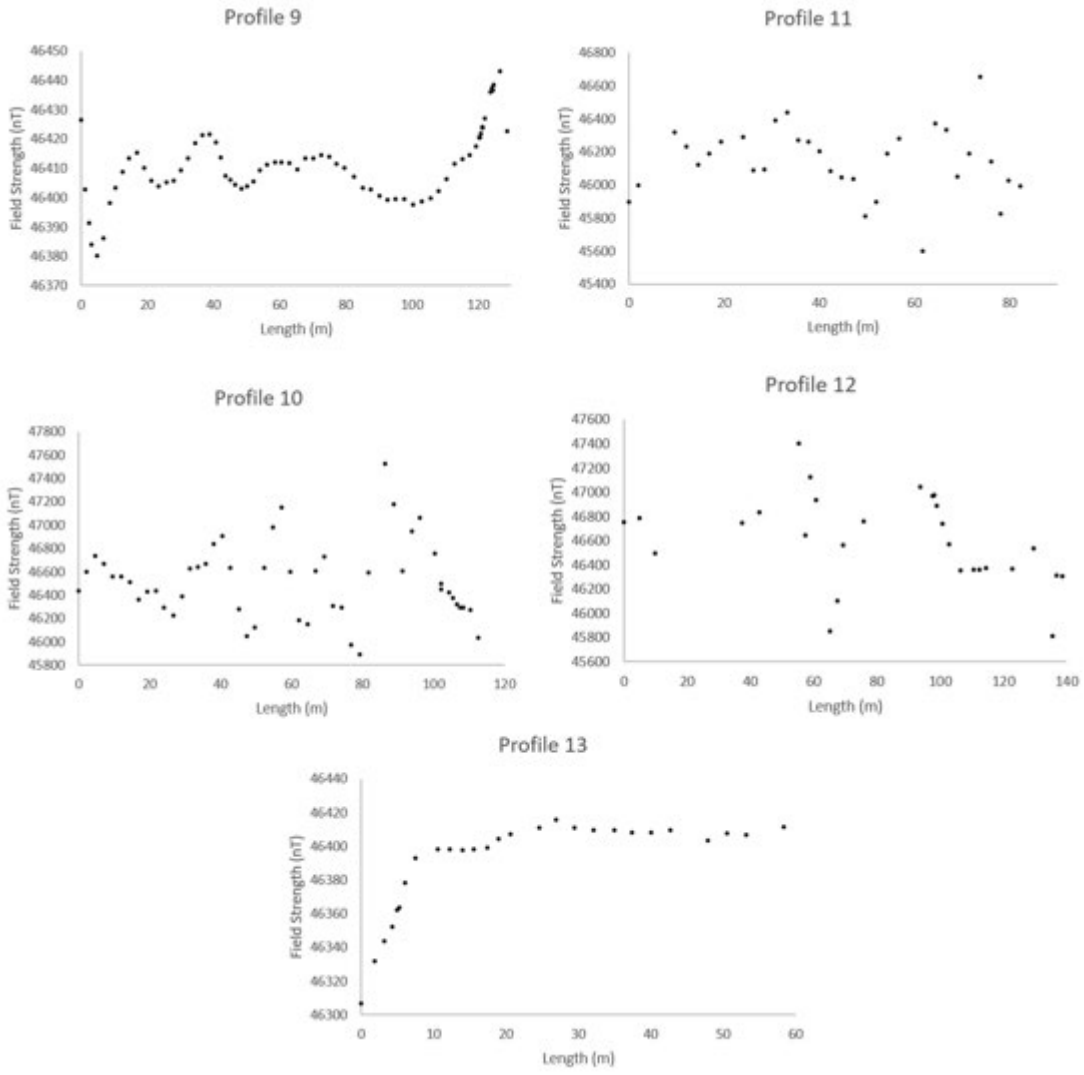

Figure 3.16. Magnetometer profiles 9-13. Profile lengths are tracked on the bottom axis. Measured magnetic field strength values are tracked on the side axis. Field strength values were measured in nanotesla. Note variation in vertical and horizontal scales.

Profile two shows minor changes in the field strength value. The trend matches the values collected along the previous profile in terms of magnitude. Profile three exhibited an 800 nanotesla shift across the first 50 meters of the profile. The values then return to an approximate magnitude of 46250 nanoteslas. Profile four shows significant variance for the sampled data points across the entire length of the survey line. There is a general trend of a drop in 500 nanoteslas across the length of the line. This trend is overshadowed by the significant variance of the individual data points. Profile five is the longest of the

sampled lines. The vast majority of the values ranged from 46300 to 46500 nanoteslas. Some anomalous variance exists at the start of the line as a result of two measurements. The sixth profile ranges from a maximum of approximately 48000 nanoteslas to a minimum of approximately 46350 nanoteslas. The spike to 48000 nanoteslas is composed of three highly variable data points. Midway through the line a spike to 46450 nanoteslas was observed. This non-anomalous spike is composed of multiple data points rather than the three points observed in the highly variable spike at the start of the line. Data points collected along profile seven show a consistent trend of 46400 to 46450 nanoteslas. A three-point anomalous spike at the beginning of the line punctuates the first 20 meters of the profile. Profile eight exhibits a range of collected values from 46200 to 47100 nanoteslas. Recorded signals across the profile are highly variable and poorly constrained by data points. Zones with minimal variance are well constrained by significant numbers of recorded measurements. The signals sampled along profile nine range from approximately 46450 to 46380 nanotesla. Shifts in the signal are well constrained by multiple observations across the entirety of the sampled line. Plotted data collected along the ninth profile display a range of values from around 46450 to 46380 nanoteslas. Peaks and troughs in field strength are composed of a large number of data points. A trend of increasing field strength is displayed along the sampling line. Data recorded along profile 10 exhibited a range of field strength values from 47530 to 45830 nanoteslas. Field strength values oscillate around a relatively even 46500 nanotesla trend. Peaks and troughs in measured field strength values are poorly constrained by a small number of observations. Points plotted from profile 11 range in field strength value from 46655 to 45600 nanoteslas. Maximum and minimum values are poorly constrained by a small

number of points. Troughs and peaks vary from moderately to poorly constrained across the profile. Field strength values follow a minor rise and fall across the length of the profile. The quality of data points collected on the first 55 meters was low and fluctuations in field strength wherein were not well-constrained as evidenced by the small number of observations. Maximum and minimum values on the profile ranged from 47400 to 45810 nanoteslas. Profile thirteen, the last and second shortest in terms of lateral expanse, exhibited at first a marked and then a gradual increase in field strength value. Maximum and minimum values ranged from 46415 to 46306 nanoteslas. The maximum and minimum values as well as the troughs and peaks of the profile are likely not affected by subsurface igneous bodies because they were not mapped on the field site, and there exists a substantial amount of metal debris and litter around the field site both buried and exposed on the surface that would affect the experimental data.

4. DISCUSSION:

All methods yielded useful data to help characterize the properties of the slide, but the spectral ratio method produced the most pertinent data with observations that proved most valuable. Overall, results were mixed. With that being stated, the three methods other than HVSR showed potential for use on this landslide and others. In this particular case, the GPR, gravity, and magnetic methods still produced workable data that, when paired with the HVSR collected during this study and the borehole data collected by other researchers, provided valuable insight pertaining to the subsurface. To a substantial degree, the more time-intensive methods produced better data than the faster methods with shorter deployment times and durations. For example, GPR methods were exceptionally easy to execute on the field site but ultimately poorly suited to survey the site under standard conditions.

4.1. Spectral Ratio Discussion:

Sliding surface geometry across the majority of the slide plane could be highly undulatory, as suggested by the variable peak frequency values recorded across the site. Congruent to work done by previous researchers at other locations, the H/V spectral ratio experiment revealed that the depth of the soil column to the sliding surface could be reasonably estimated from the peak frequency data using a velocity value of 145 meters per second for S-waves in churned alluvial material (Xia et al. 1999). Depth to the sliding surface was compatible at multiple point locations to those previously mapped by borehole studies. A map of the depth values is displayed in Figure 4.1. Cross sections of the slide from scarp to toe show similar depth values as those determined through the passive seismic surveying. Figure 4.2 compares sampled points to the interpolated sections.

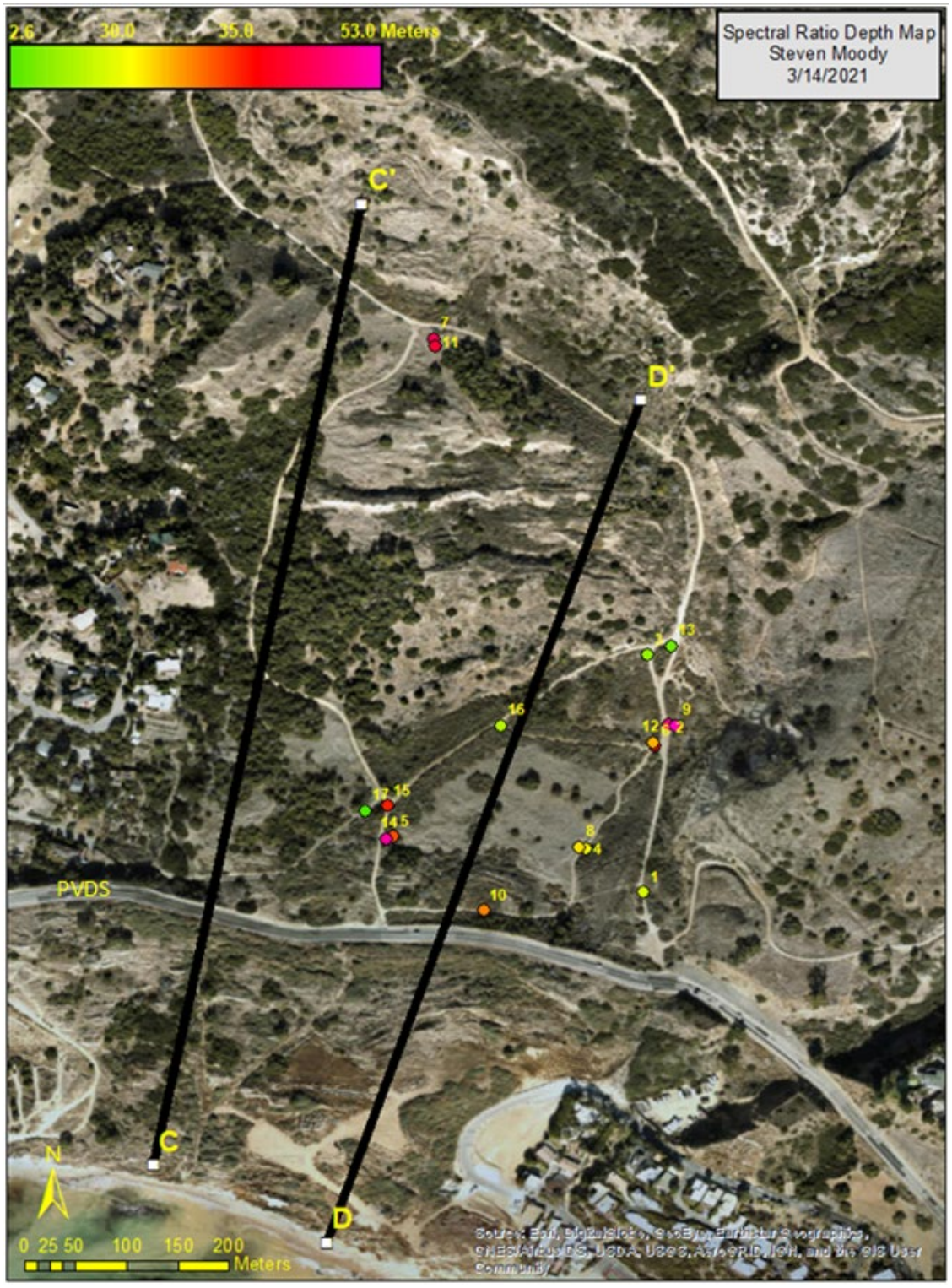

Figure 4.1. Map created in ArcMap 10.6.1 with cross section lines and HV survey points. The color-coded points are related to the colored scale in the top left corner. Depths are given in meters. PVDS marks Palos Verdes Drive South.

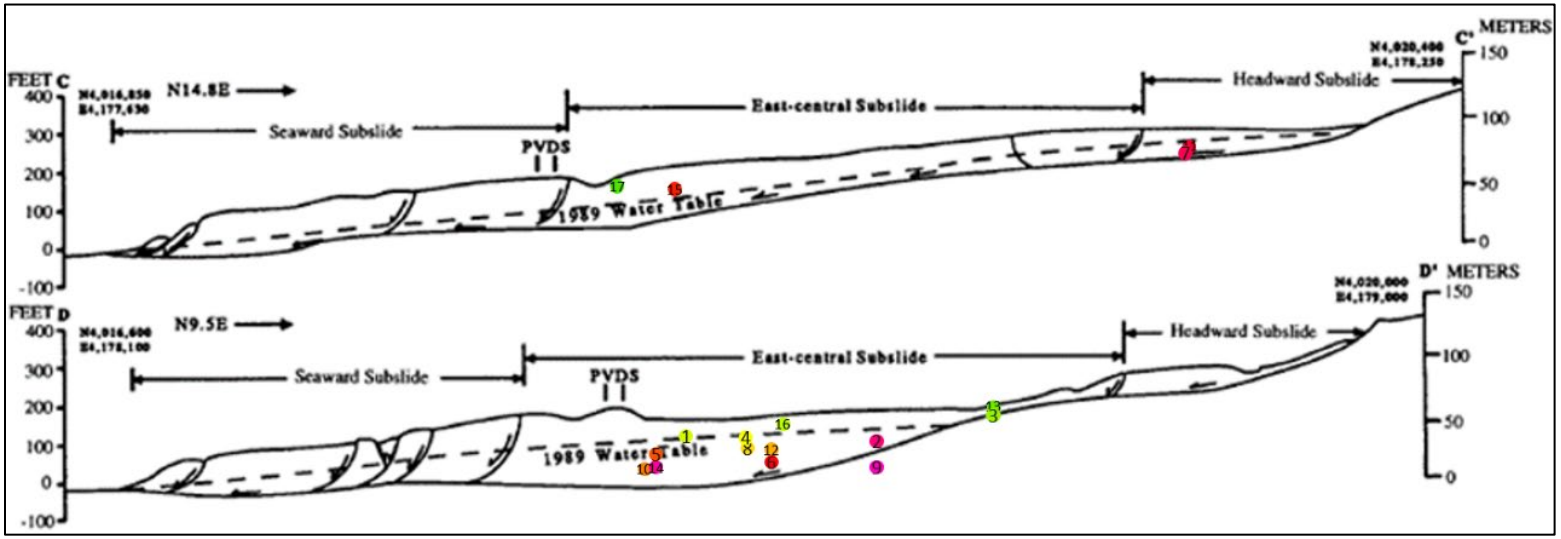

Figure 4.2. Cross sections C-C' and D-D' from Ehlig. The sliding surface displayed in the sections is nonuniform. The cross sections were produced through interpolation of borehole data alongside outcrop mapping. Depth points were placed onto the closest cross section. Points are labeled according to their station ID as seen on the map in Figure 4.1. Hotter colors represent greater measured sediment thicknesses while cooler colors represent lesser sediment thicknesses. Modified from Watry and Ehlig 1995.

Surveying done after rain revealed differences to the depth values calculated from the peak frequencies of the spectral ratio curves at the same points surveyed during the drought before the onset of the winter rains. Figure 4.3 compares dry and wet season depths. In

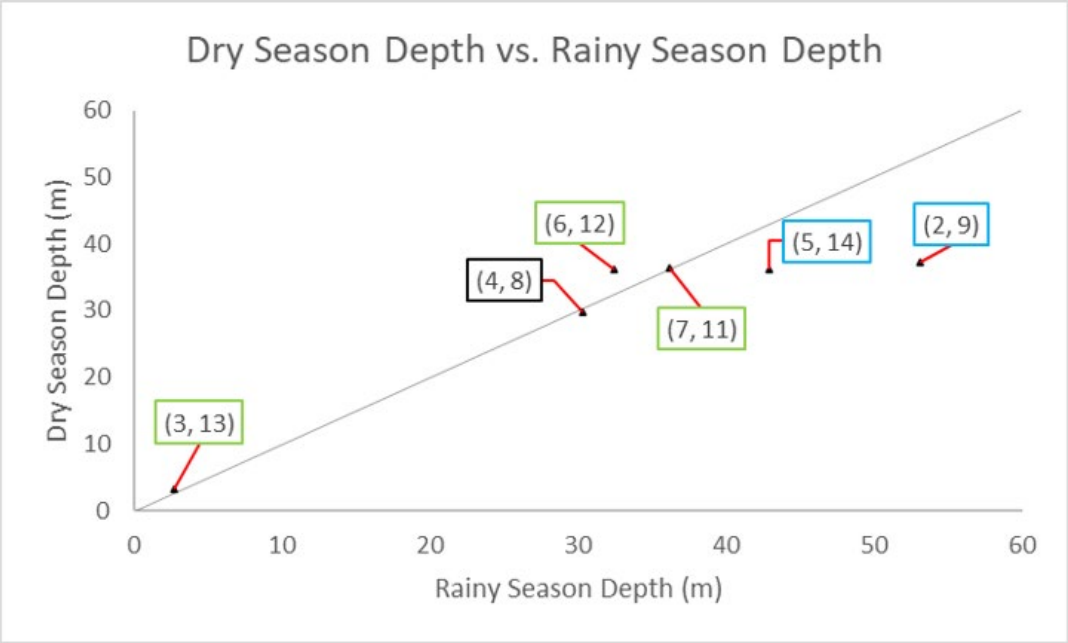

Figure 4.3. Comparison of the dry and rainy season depths derived from the seismic spectral ratio curves is displayed. Depths on the axes are given in meters. Each point is labeled with the corresponding paired station IDs. Depths determined from the dry season data correspond to the first number in each pair and are linked to the y-axis value, while the depths determined from the wet season data at the same geographic location correspond to the second number in each pair and are linked to the x-axis depth value. Green boxes highlight pairs with greater dry season depth, blue boxes highlight pairs with greater wet season depth, and the black box highlights a pair with minimal to no change observed.

most cases, a shift in peak frequency was observed, suggesting that the presence of seasonal water in the subsurface caused a variance in peak frequency observed at the same site at different times. Interpolated depth values from Ehlig's interpolated cross sections and interpolated contour map were used as the baseline to which points were compared. Comparisons of calculated depth to the interpolated depths are shown in Figure 4.4. Because of this, there is uncertainty regarding the accuracy of Ehlig's sediment thickness determinations and water table heights used for the construction of each of his four cross

sections. This coincides with Ehlig's observations that the slide plane is a relatively impermeable layer, which would slow the drainage of water out of the slide and allow for

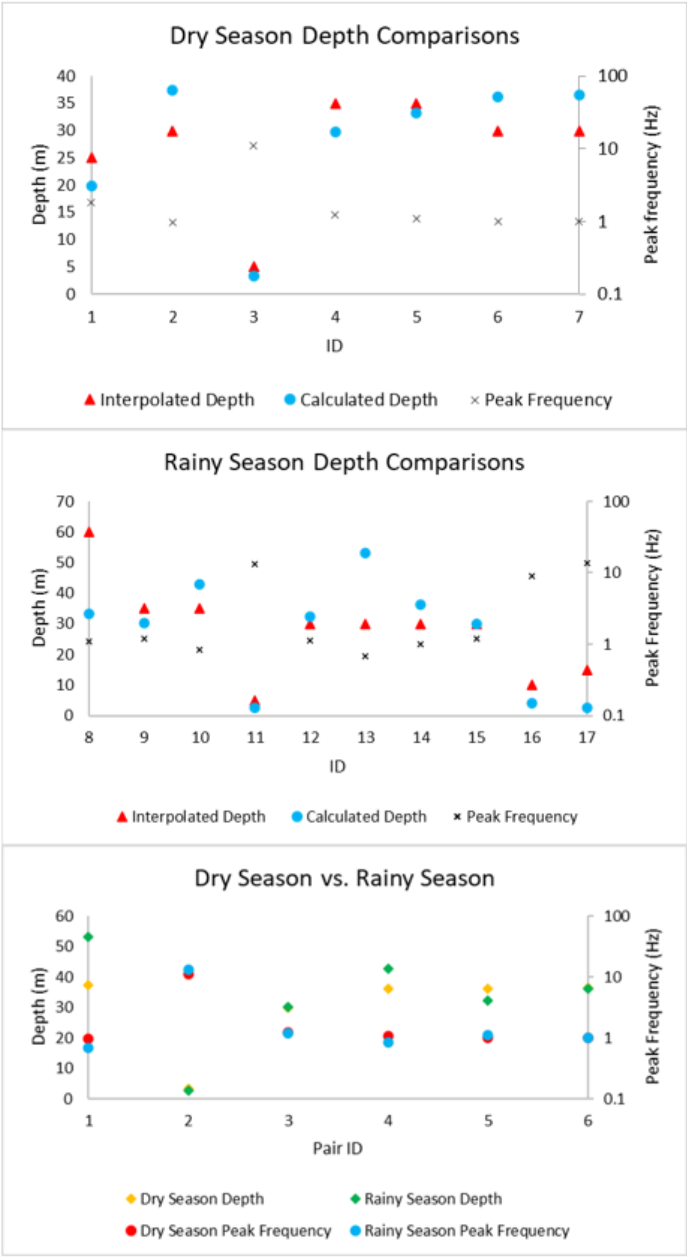

Figure 4.4. Comparison of Ehlig's determined depth, or the interpolated depth at each point, and the calculated depth determined with the quarter wavelength equation during both the dry and rainy seasons are displayed in the first two plots. Dry and rainy season calculated depths as well their respective peak frequencies are compared against each other in the bottom plot. Interpolated depths were determined via reference to the interpolated contour map generated by Ehlig and referred to in this document as Figure 1.6. Pair ID 1 consist of points 2 and 9, Pair ID 2 of points 3 and 13, Pair ID 3 of points 4 and 8, Pair ID 4 of points 5 and 14, Pair ID 5 of points 6 and 12, and Pair ID 6 of points 7 and 11.

detection of that acoustic boundary for longer periods after rainfall. Along with the physical properties of the Altamira Shale member, the susceptibility of the tuffaceous rocks and their subsequent breakdown into bentonite clay, the previously observed and slow dewatering rate of the slide, and the observed shift in peak frequency indicates that water could be ponding on the sliding surface thus producing a shift upward in peak frequency. Most data points surveyed showed the previously mentioned trends or did not change significantly after precipitation with the exception of four points. These points are shown in Figure 4.5. In this instance, the reversal of the general trend of the processed data could be the product of a variety of factors. It is possible that the seismometer was sampling a location with different soil column depths to the sliding surface, detecting a difference in the overlying slide material, detecting the influence of groundwater movement, or was sampling a location where the sliding interface was broken up. All of these factors could produce variable results. Given the proximity of sampling for these pairs however, different soil column depths seem unlikely. A small number of explanations exist that might adequately explain this discrepancy. One potential cause of the discrepancy is poor sampling conditions. It is possible that during data collection on either one or both of the days, a non-ideal sampling environment might have prevailed. Non-ideal sampling environmental conditions that could have obscured the ambient seismic signal include substantial amounts of pedestrian, horseback, or vehicle traffic, or substantial wind. However, extensive periods of windy weather were not prevalent on the field site during the duration of testing at these sampling locations. Influence of pedestrian events were removed during processing by removing the segments of data containing pedestrian events. It is also possible that the sampling environment at points two, nine, five, and fourteen was

poor for testing due to the presence of surficial vegetation and/or anomalous sliding surface conditions such as a cracked or structurally compromised plane or a steeply dipping

Figure 4.5. Map created in ArcMap 10.6.1. The other HV survey points have been omitted. Two data pair locations are displayed. The first pair consisting of data points two and nine and the second pair consisting of points five and fourteen recorded data trends that ran counter to the seasonal trend detected at the other data point pairing locations. The larger number in each pair represents the recording taken after rainfall and the smaller number in each pair represents the recording taken during the dry season. The frequency range for the four points, measured in hertz, is color coded according to the scale in the top left corner.

bedrock surface. It is unlikely that vegetation is an impactful cause for data inconsistency between observations at this location because the field site is heavily vegetated during both wet and dry seasons. As such, all data collected from the seismic experiments is likely affected in some way by the presence of vegetation. This makes it unlikely that the four anomalous curves generated were a consequence of relatively close proximity of the deployment sites to vegetation. A seismic event likely did not impact the results because Geopsy removes windows with impulsive signals such as those that would be generated by seismic events. USGS records corroborate this claim. This leaves either the possibility of anomalous or unexpected subsurface structure, an unforeseen potential influence of water in the soil column, or statistical error. Water percolating through the soil column could slow down S-wave transmission through the subsurface by reducing interparticle coupling caused by the increase in pore pressure, subsequent reduction in confining pressure, and increase in volume relative to the dry soil at the same location. A phenomenon similar to this was observed in sediments of the Nankai Trough in Japan, but on a much more significant scale. It was shown that exposing samples of saturated material to increasing magnitudes of confining pressure would result in increasing S-wave velocity. Additionally, small magnitudes of pressure change can result in significant changes in S-wave velocity (Schumann 2014). This could manifest in the HVSR data as a lower peak frequency and subsequently greater calculated thickness of overlying sediment, when in reality the sediment thickness is the same as was previously calculated at that location and the true S-wave velocity is slower at the resampled location after rainfall instead. This is possible, but the pressure change in the soil after precipitation would need to be recorded and analyzed to make a more concrete determination. Excluding these four points, the introduction of

rainwater into the soil column could manifest in the data as multiple peaks where they might have previously been one, a shift in observed peak frequencies to a higher frequency from a lower one, or the broadening of the seismic spectral ratio curve. Curves typically displayed a shift in peak frequency from lower to higher, potentially as a result of rainwater ponding on the sliding surface. Additionally, calculated depths were generally found to be shallower than the interpolated depths, suggesting that the overlying sediment layer might be thinner than previously expected. Resampling of all locations with a dense spacing of measurements near the sites would be beneficial, but there is no strong evidence that indicates that the current processed data does not represent the site's physical properties.

4.2. Gravity Discussion:

Gravity surveying revealed differences in gravitational acceleration along profile lines that can likely be attributed to the presence of subsurface water as well as variance in depth to the sliding surface along surveyed sections. Changes in gravitational acceleration were of relatively small magnitude and the values generally changed gradually, not rapidly, along both profile lines. Although gravity methods provide valuable insight on the physical properties of a location, modeling efforts are negatively impacted by non-uniqueness issues. Examination of the Bouguer anomaly profile lines indicate that there is a variation up to a maximum of approximately 27 milligals across the southern line and a little more than 1.6 milligal across the northern line. Figures 3.6 and 3.7 in the previous chapter contain a map of the survey lines and display the observed anomaly trends respectively. Makino's Bouguer anomaly trends on the Guinsaugon landslide in the Philippines showed a pronounced gravitational low approximately centered in the slide body with highs on each edge. Makino sought to explain the observed trends by providing a model of a churned

alluvium sliding material sitting enclosed in a graben within the Philippine Fault Zone. (Makino 2007). This is different from what was observed on the PBL. The active PBL is not faulted in the same way as the Guinsaugon landslide, but it is flowing inside a syncline spawned from a narrow graben structure south of Crest Road toward the ocean (Merriam 1960). It has been established by previous researchers that igneous bodies have intruded into the Altamira Shale up until the end of coastal volcanism approximately 24 Mya (Merriam 1960). These bodies will produce spikes in the gravity profile line, whereas deep mixed slide material will produce a much smaller Bouguer anomaly. These trends have been observed both in the Canary Islands on expansive landslides and on slides similar in size to the active PBL. It is unlikely that mafic bodies were present along the survey line since their presence was not mapped in the field area. Although mafic bodies could be present in the subsurface along the field line, additional surveying, coupled with modeling to determine the potential gravitational signature of such a body, would have to be performed before making a more concrete determination. It is possible that an area of increased sediment thickness was detected when immediately crossing into the slide, as is evidenced by the drop in Bouguer anomaly. The marked spike upward in anomaly magnitude further along the line could be the result of the layers of asphalt left over from prior road resurfacing projects. The continued failure of the road as a result of constant slide movement would prompt continual repaving by the city, creating a localized high-density zone close to the surface. On the northern line, the gradual decrease in Bouguer anomaly is potentially due to the gradual thickening of sliding material which is correspondent with a moderate increase in elevation along the profile. Simply put, slide material is shallow closer to the scarp at the start of the northern line where minimal

variation in Bouguer anomaly was detected and sliding material is thicker further from the scarp and where lower magnitudes of Bouguer anomaly were recorded. Additionally, it is possible that the minimal variation at the start of the southern line and the increase in variation closer to the middle and end of the line could be the result of crossing the landslide edge with the survey line.

4.3. GPR Discussion:

GPR surveys were conducted along the field site trails using a 400 MHz antenna. The field area is displayed in Figure 3.8 in the previous chapter. The maximum depth detectable by the GPR antenna should be close to 12 meters under good site conditions. This assumption would hold as long as the bottom of the GPR unit could be consistently coupled with the ground and assuming that, for any surveys collected prior to rainfall, the water in the subsurface would not be collected on the surface, or at shallow depths such that the radar signal would be significantly impeded from penetrating to and imaging the targeted feature in the subsurface. The surveys performed were both poor in terms of quality and imaging depth. Figure 3.10 represents the majority of the data and is a good example of poor quality and imaging depth. This was largely due to poor coupling of the GPR to the ground surface because of the multitudinous presence of multiple, cobble-sized rock pieces scattering the survey area. It is also possible that the saline spray from the ocean combined with the attenuating properties of the clay in the surveyed medium could have exacerbated signal attenuation problems. During the surveying of what supposedly used to be the location of Ishibashi Lake, poor sampling conditions continued to prevail and the resultant data was poor and mostly devoid of significant useful information. A dipping subsurface interface was detected along one of the profiles, but at such a shallow depth as

to exclude the possibility that the slide plane itself had been successfully imaged. Instead, the boundary detected was likely evidence of an old rill created during a previous rain or the shallow end of a tension trough. The GPR data could only be used to confirm the very basic assumption that the structural feature of interest was very likely below a depth of ten meters along the survey lines. We can therefore conclude that GPR surveys with antennas of this frequency may be of limited use in imaging the interior of the PBL. Any further experiments should explore the use of more powerful antennas that might be able to image to greater depth and suffer less attenuation.

4.4. Magnetometer Discussion:

Magnetometer experiments are typically used to identify the lateral contrast between materially distinct geologic bodies or units, such as iron bearing mafic intrusions that may possess strong remanent magnetization relative to the overlying sediment or surrounding bedrock. In this case, use of the magnetometer was performed with dual purpose; to determine the location of subterranean igneous bodies or objects with remanent magnetization and to examine any possible correlation between magnetic intensity and the relative depth to the sliding surface on the landslide. A map of each data point can be viewed in Figure 4.6. Magnetic methods showed significant variation across the field site even after anomalous points were removed, but interpretation of the variation detected and whether it resulted from the presence of subsurface igneous bodies, the sliding surface at various depths, or from buried detritus such as metal litter, stakes, or sectioned culverts requires more advanced analysis than can be performed for this examination. There are small differences between the magnetic susceptibility of underlying rock and overlying

sediments (Burger et al. 2006). If these differences are substantial, detection of the sliding

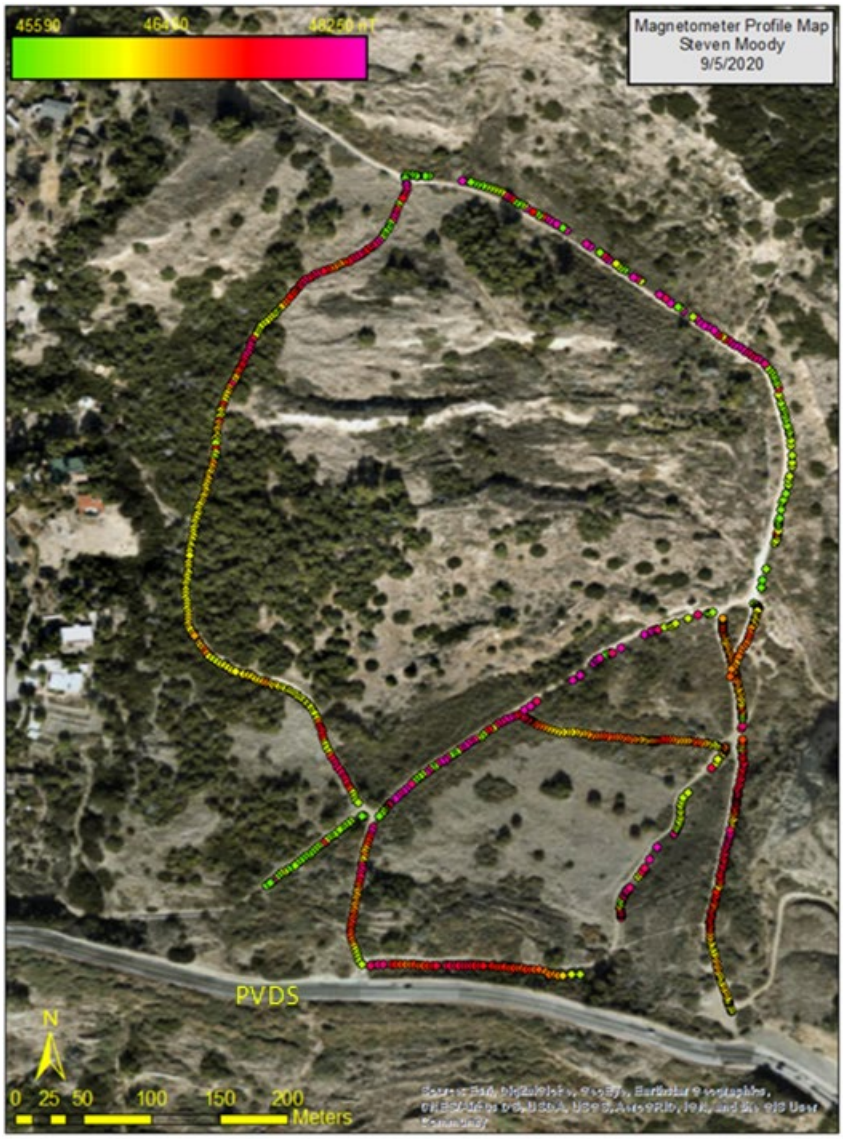

Figure 4.6. Map of the magnetometer data points. The data displayed shows a broad range of magnetic field strength values recorded across field site. Metal detritus, loose waste, and significant amounts of metal piping, iron stakes, and metal staples for drainage pipe are prolific across the expanse of the field site, likely obscuring the magnetic signal of subsurface features of interest.

surface could be possible. However, the signal produced by the minor differences in susceptibility can be obscured in the signal if there is significant metal detritus or other magnetic fields such as those created by power lines interfering with the data collection. It is important to note that all data was collected on the same time to avoid the need to correct for diurnal variation of Earth's magnetic field. On analyzing the thirteen profiles produced

with the acquired magnetic data, it is unclear whether any subsurface geologic bodies, such as mafic intrusions, or the slide plane were detected. In all cases metal detritus, such as loose rebar, iron pylons, culvert piping, metal cans, and staples for rubber drainage pipe, littered the field site. The fifth profile was run in some part with telephone lines within 25 meters of the line. For example, charting of the data surveyed along the fourth profile displayed substantial variance in field strength value across the entirety of the profile line, but the general trend shows a shift from a stronger magnetic signal to a weaker signal. Although it is not feasible to determine a numerical depth to the slide plane with this information, it may be possible to infer a relative shallowing or deepening of slump material overlying the sliding surface. Employing this assumption, it is possible to discuss the other profiles in a similar light while coupled with the four cross sections developed by Ehlig. Using the approximate depths to the slide plane from the figure and the alignment of the magnetic survey lines with the cross-section lines, we may hypothesize as to the relative deepening or shallowing of the sliding surface with the magnetometer data. The first profile collected followed a gentle descent along a trail into the field site. The data collected exhibits a smooth, typically uninterrupted trend. When coupled with Ehlig's D-D' cross section, it can be observed that there is a moderate deepening to the sliding surface when traversing from south to north along D-D'. This measured increase in magnetism is correlative to the progressive shallowing of the slumping material following the survey line. In summary, there does seem to be a correlation between the magnetic field strength recorded and the hypothesized depth to the sliding surface on the field site, but the interference produced by the metal detritus present in many locations in the study area significantly decreases the reliability of the data and therefore impedes its interpretation.

Determination of an absolute depth to the sliding surface is not possible with the current data, so comparison to other data sets is paramount. Like many of the other methods, opportunity exists for the collection of more information.

5. CONCLUSIONS:

The PBL is a significant geomorphological feature with a prominent status in the eyes of the local populace and serves as a protected habitat for flora and fauna. Continued development of the understanding of the slide helps address a significant public safety and financial hazard that relentlessly damages private property and public infrastructure. As such, the application of cost-effective and non-invasive methods that allow researchers to adequately characterize the subsurface and physical parameters of the landslide is critical to preparation for and mitigation of the potential damages incurred from slide activity. The conclusions that can be derived from this study are as follows. Firstly, the application of multiple geophysical techniques can certainly be viable in determining critical subsurface properties of landslides. During this study, the spectral ratio method was the most successful in detecting the subsurface feature of interest as well as providing an insight into the physical properties of the PBL. Sediment thicknesses determined through HVSR were typically shallower than the interpolated thicknesses determined by other researchers.

Secondly, there is a measurable change in the spectral ratio curves sampling locations before and after precipitation. From this, it appears that the introduction of rain produces a notable change in the material properties above the sliding surface, possibly as a result of water ponding on the sliding interface. Gravity surveys detected differing anomaly trends for lines proximal to and far away from the landslide scarp, respectively. Minor variance in observed Bouguer anomaly marked by a sudden increase in variance was detected along the southern line furthest from the scarp. This was likely due to the variation in sliding material thickness close to the edge of the slide, where a dip in Bouguer anomaly was observed as well as the spike upward in anomaly value due to the detection of multiple

pavement layers recorded closer to the middle of and end of the profile line. GPR methods did not image down to sufficient depth and suffered from severe signal attenuation. Magnetic methods are not likely to detect a consistent variation in magnetic field on this site. This is due in large part to the significant amount of metal debris on the site obscuring the subtle differences in magnetic signal that the minor susceptibility contrasts between the bedrock and overlying slide material would produce. Surveying with a grid pattern would likely minimize these effects as the metal debris is primarily distributed alongside the trails. Ultimately, the research goals were met, but with significant room for continued study in the future.

6. FUTURE WORK:

A continuation of the work performed during this study would be very useful for constraining the subsurface geometry of the slide plane. More complete coverage of the trails, and of locations off of the trails, would be suggested for seismometer deployment. A longer duration for deployment of seismometers at the field site would be beneficial to reduce errors in the analysis. Electrical resistivity surveys across the slide body and perpendicular to the slide scarp could be employed along with the seismometers to examine both seasonal variation and model the physical properties of the subsurface above and along the sliding surface. Magnetometry performed without location restrictions on the field site might also reveal more insights on the subsurface geology, especially since this would enable a more complete 2D picture but based on this study as well as previous work on other slides, spectral ratio and electrical resistivity are the more successful experimental methods. For all of these future experiments, acquiring the permission and the assistance of the PVPLC via vigilant and frequent communication would be instrumental in improving ease of access and interagency communication to protect experimenters in the field from outside interference from law enforcement agencies, community activists, and community residents, while also protecting the pedestrians traveling on the site. All of the previously mentioned factors interfere with the data collection for all of the methods and in the case of electrical resistivity, might even present a clear danger to uneducated interactors with the equipment such as hikers, bikers, and horseback riders.

7. WORKS CITED:

Atwater, T., 1970, Implications of Plate Tectonics for the Cenozoic Tectonic Evolution of Western North America: Geological Society of America Bulletin, v. 81, p. 3513-3536.

Bouali, E. H., Oommen, T., and Escobar-Wolf, R., 2019, Evidence of Instability in Previously-Mapped Landslides as Measured Using GPS, Optical, and SAR Data between 2007 and 2017: A Case Study in the Portuguese Bend Landslide Complex, California: Remote Sensing, v. 11, p. 937, doi:10.3390/rs11080937.

Brooke, J.P., 1973, Geophysical investigations of a landslide near San Jose, California: Geoexploration, v. 11, p. 61-73, https://doi.org/10.1016/0016-7142(73)90049-5.

Bryant, M.E., 1987, Emergent marine terraces and quaternary tectonics, Palos Verdes Peninsula, California: Geology of the Palos Verdes Peninsula and San Pedro Bay SEPM (Society for Sedimentary Geology).

Burger, H.R., Sheehan, A.F., Jones, C.H., 2006, Introduction to Applied Geophysics: Exploring the Shallow Subsurface: W.W. Norton and Company, Inc., 554 p.

Carracedo, J.C., 1996, A simple model for the genesis of large gravitational landslide hazards in the Canary Islands: Geological Society, London, Special Publications, v. 110, p. 125-135, https://doi.org/10.1144/GSL.SP.1996.110.01.10.

Calabro, M. D., Schmidt, D. A., and Roering, J. J., 2010, An examination of seasonal deformation at the Portuguese Bend landslide, southern California, using radar interferometry: Journal of Geophysical Research, v. 115, F02020, doi:10.1029/2009JF001314.

Chen, Y., Irfan, M., Uchimura, T., Meng, Q., 2020, Relationship between water content, shear deformation, and elastic wave velocity through unsaturated soil slope: Bulletin of Engineering Geology and the Environment, v. 79, https://doi.org/10.1007/s10064-020-01841-8.

Conrad, C. L., and Ehlig, P. L., 1987, The Monterey Formation of the Palos Verdes Peninsula, California – An Example of Sedimentation in a Tectonically Active Basin Within the California Continental Borderland: http://archives.datapages.com/data/pac_sepm/071/071001/pdfs/17.htm.

Del Gaudio, V., 2000, Gravimetric study of a retrogressive landslide in southern Italy: Surveys in Geophysics, v. 21, p. 391-406.

Del Gaudio, V., 2013, New developments in ambient noise analysis to characterise the seismic response of landslide-prone slopes: Natural Hazards and Earth System Sciences, v. 13, p. 2075-2087, doi:10.5194/nhess-13-2075-2013.

Dibblee, T.W., 2011, Geologic map of the Palos Verdes Peninsula and vicinity, Redondo Beach, Torrance, and San Pedro Quadrangles, Los Angeles County, California: Dibblee Geology Center, scale 1:24,000

Ehlig, P. L., 1987, Portuguese Bend landslide complex, southern California: Geological Society of America Centennial Field Guide-Cordilleran Section, p. 179-184.

Ehlig, P. L., 1987, The Portuguese Bend landslide Stabilization Project: http://archives.datapages.com/data/pac_sepm/071/071001/pdfs/217.htm (accessed March 2020).

ESRI, 2018, ArcMap 10.6.1: Software package that enables processing of point data, map creation, and access to satellite imagery for scientific purposes: Environmental Systems Research Institute, https://www.esri.com/en-us/home.

European Commission – Research General Directorate, 2004, SESAME: Guidelines for the implementation of the H/V spectral ratio technique on ambient vibrations measurements, processing and interpretation.

Haydon, W. D., 2007, Landslide Inventory Map of the PALOS VERDES PENINSULA Los Angleles County, California: California Geological Survey, scale 1:24,000.

Imposa. S., 2017, Geophysical surveys to study a landslide body (north-eastern Sicily): Natural Hazards, v. 86, p. 327-343, doi:10.1007/s11069-016-2544-1.

Jennings, C.W., 1962, Geologic map of California, Long Beach sheet: California Division of Mines and Geology, scale 1:250,000

Kosaka, K., 2000, Evaluating landslide deposits along the Tsurukawa fault zone, Japan, using magnetic susceptibility: Bulletin of Engineering Geology and the Environment, v. 58, p. 179-182.

Linden, K. V., 1989, The Portuguese Bend Landslide: Engineering Geology, Elsevier, 27 (1-4), p. 301-373.

Ling, C., Xu, Q., Zhang, Q., Ran, J., Lv, H., 2016, Application of electrical resistivity tomography for investigating the internal structure of a translational landslide and characterizing its groundwater circulation (Kualiangzi landslide, Southwest China): Journal of Applied Geophysics, v. 131, p. 154-162.

Lissak, C., Maquaire, O., Malet, J. P., Lavigne, F., Virmoux, C., Gomez, C., and Davidson, R., 2015, Ground-penetrating radar observations for estimating the vertical displacement of rotational landslides: Natural Hazards Earth System Science Discussion, 15, p. 1399-1406.

Makino, M., Mandanas, A. A., and Catane, S. G., 2007, Gravity basement of the Guinsaugon landslide along the Philippine Fault Zone: The Society of Geomagnetism and Earth, Planetary and Space Sciences, v. 59, p. 1067-1071.

McGee Surveying and Consulting, 2013, Portuguese Bend Landslide Monitoring Survey: City of Rancho Palos Verdes.

Meric, O., Garambois, S., Malet, J., Cadet, H., Gueguen, P., Jongmans, D., 2007, Seismic noise-based methods for soft-rock landslide characterization: Bulletin Societe Geologique de France, 178 (2), pp.137-148.

Merriam, R., 1960, Portuguese Bend Landslide, Palos Verdes Hills, California: University of Chicago Press.

Reiter, M., 1984, The Palos Verdes Peninsula: A Geologic Guide and More: Kendall/Hunt Publishing Company, 61 p.

Sass, O., Bell, R., Glade, T., Comparison of GPR, 2D-resistivity and traditional techniques for the subsurface exploration of the Öschingen landslide, Swabian Alb (Germany): Geomorphology, 93, p. 89-103.

Schumann, K., Stipp, M., Behrmann, J. H., Klaeschen, D., and Schulte-Kortnack, D., 2014, P and S wave velocity measurements of water-rich sediments from the Nankai Trough, Japan: Journal of Geophysical Research: Solid Earth.

Wathelet, M., Chatelain, J.-L., Cornou, C., Di Giulio, G., Guillier, B., Ohrnberger, M. and Savvaidis, A. (2020). GEOPSY: A User-Friendly Open-Source Tool Set for Ambient Vibration Processing. Seismological Research Letters, 91(3), 1878--1889, doi: 10.1785/0220190360.

Watry, S. M., and Ehlig, P. L., 1995, Effect of test method and procedure on measurements of residual shear strength of bentonite from the Portuguese Bend Landslide: Reviews in Engineering Geology, v. 10, p. 13-38.

Xia, J., Miller, R.D., Park, C. B., 1999, Estimation of near-surface shear-wave velocity by inversion of Rayleigh waves: Geophysics, v. 64, p. 659-992.

8. APPENDICES:

APPENDIX A: HVSR CURVES

A variety of HVSR curves were calculated using Geopsy, a free software designed to enable a number of processing techniques for seismic data. Default settings were used with the exception of windows and frequency bounds. Although a directional input tool existed for use in the Geopsy software suite, its use and the inclusion of processed items would only be carried out upon complete failure of SESAME criteria. Since this did not occur for any of the collected data points, a need to ascertain a potential reason for failure was nonexistent. As such, this appendix simply contains the processed curves used for analysis.

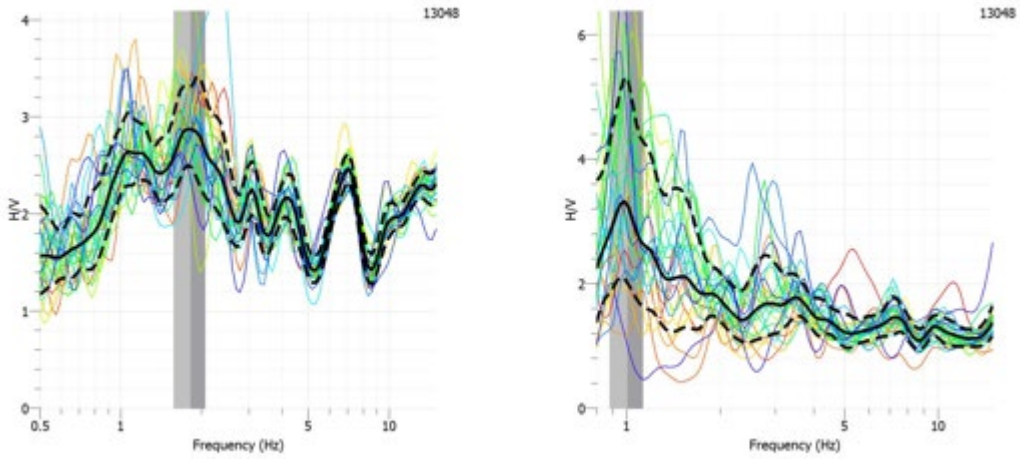

Figure A.1. HVSR curves collected on 10/17/2018. Curves were generated using Geopsy. Grey bars indicate peak frequency and the corresponding standard deviation. The solid black line represents the average curve while the dashed lines represent the standard deviation of that curve.

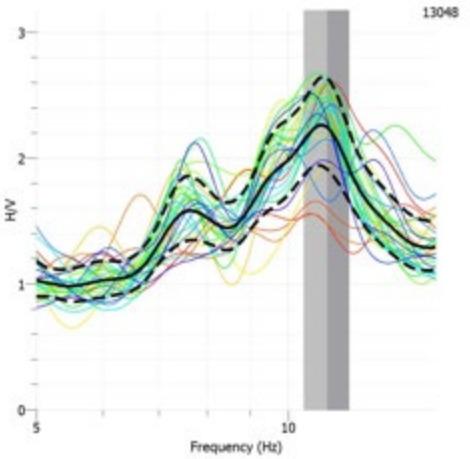

Figure A.2. HVSR curve collected on 10/18/2018. Curves were generated using Geopsy. Grey bars indicate peak frequency and the corresponding standard deviation. The solid black line represents the average curve while the dashed lines represent the standard deviation of that curve.

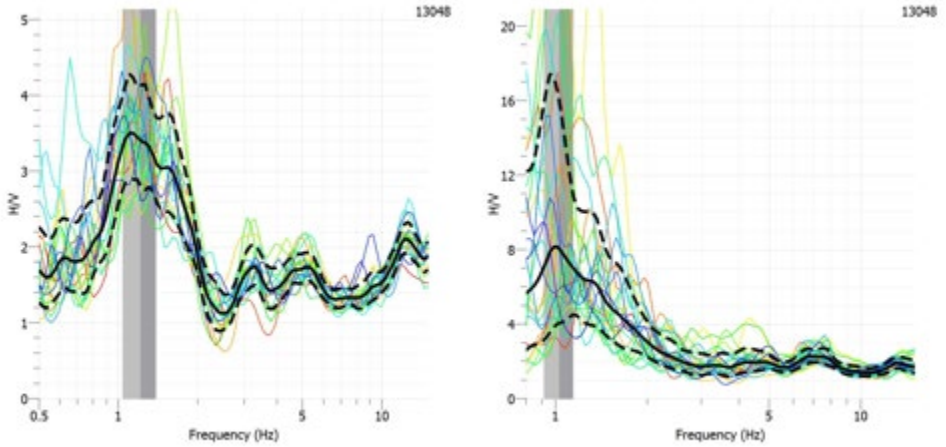

Figure A.3. HVSR curves collected on 10/19/2018. Curves were generated using Geopsy. Grey bars indicate peak frequency and the corresponding standard deviation. The solid black line represents the average curve while the dashed lines represent the standard deviation of that curve.

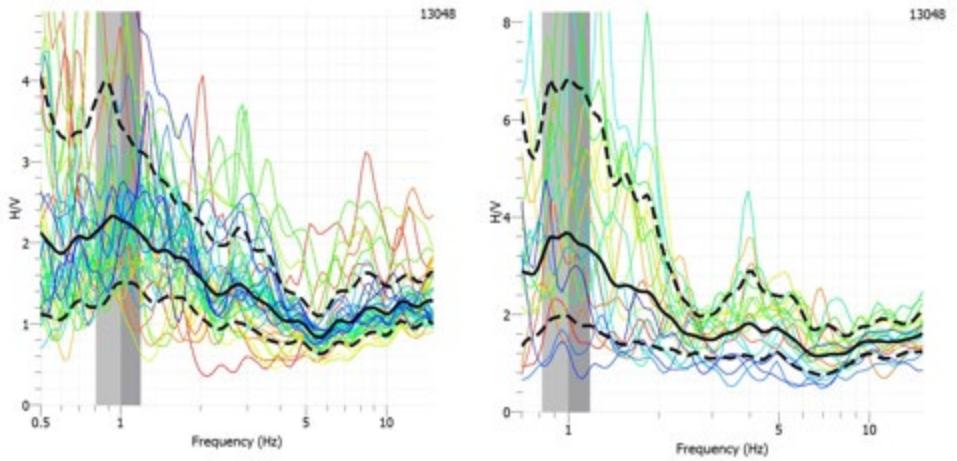

Figure A.4. HVSR curves collected on 10/22/2018. Curves were generated using Geopsy. Grey bars indicate peak frequency and the corresponding standard deviation. The solid black line represents the average curve while the dashed lines represent the standard deviation of that curve.

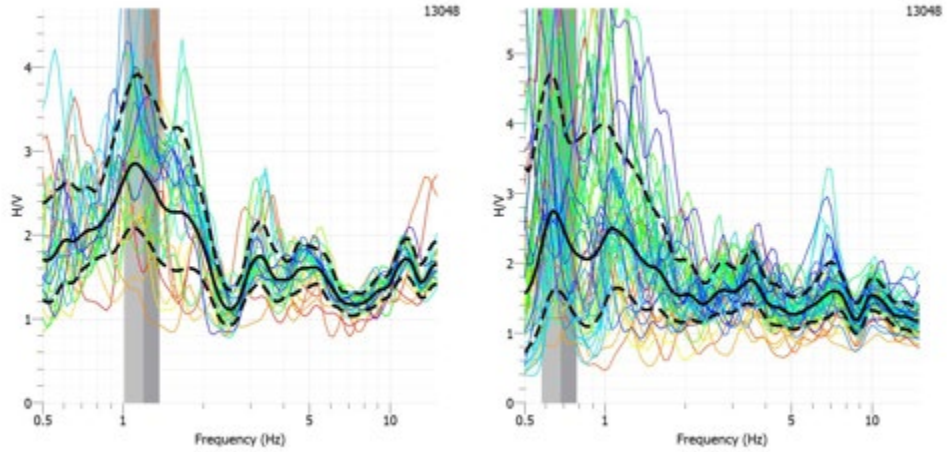

Figure A.5. HVSR curves collected on 12/3/2018. Curves were generated using Geopsy. Grey bars indicate peak frequency and the corresponding standard deviation. The solid black line represents the average curve while the dashed lines represent the standard deviation of that curve.

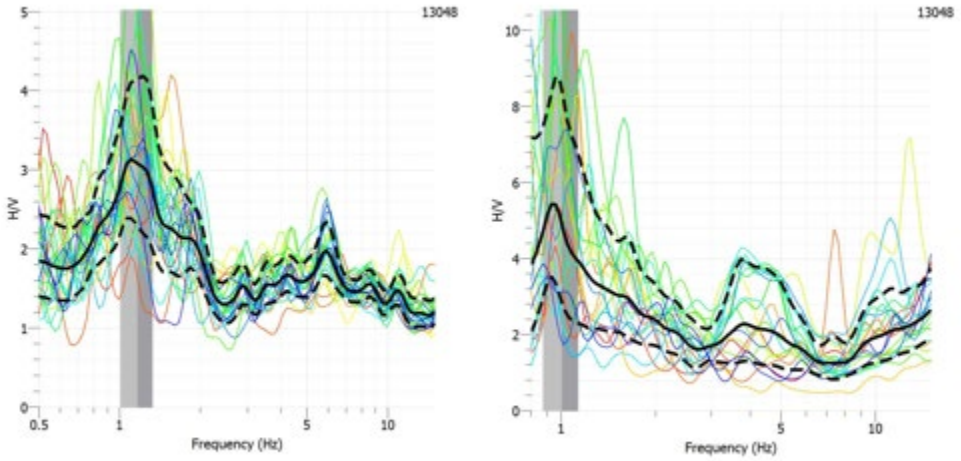

Figure A.6. HVSR curves collected on 12/9/2018. Curves were generated using Geopsy. Grey bars indicate peak frequency and the corresponding standard deviation. The solid black line represents the average curve while the dashed lines represent the standard deviation of that curve.

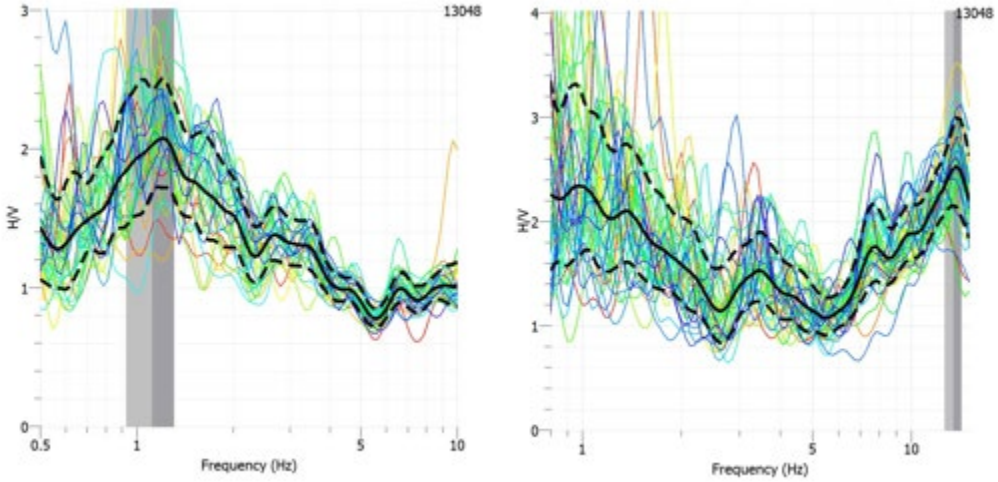

Figure A.7. HVSR curves collected on 12/10/2018. Curves were generated using Geopsy. Grey bars indicate peak frequency and the corresponding standard deviation. The solid black line represents the average curve while the dashed lines represent the standard deviation of that curve.

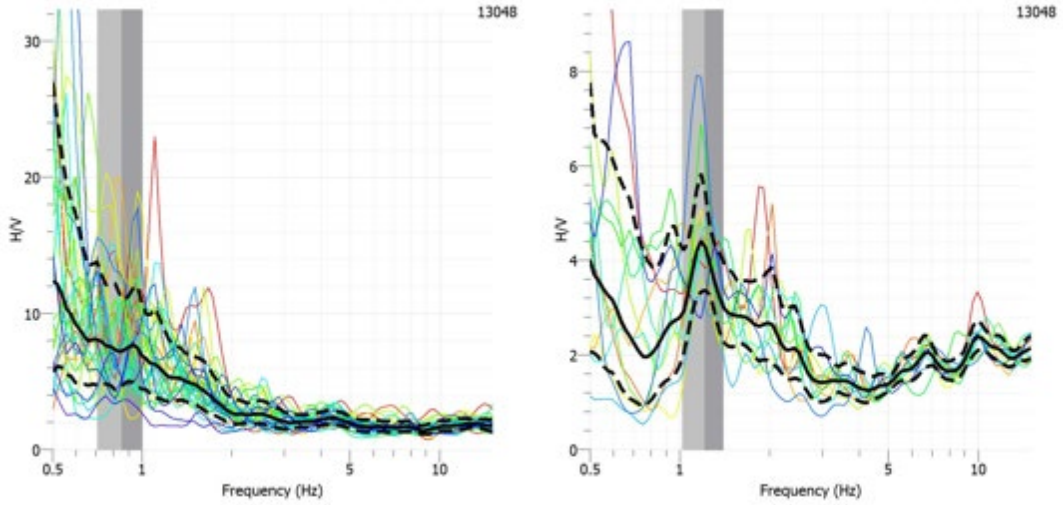

Figure A.8. HVSR curves collected on 12/2/2018. Curves were generated using Geopsy. Grey bars indicate peak frequency and the corresponding standard deviation. The solid black line represents the average curve while the dashed lines represent the standard deviation of that curve.

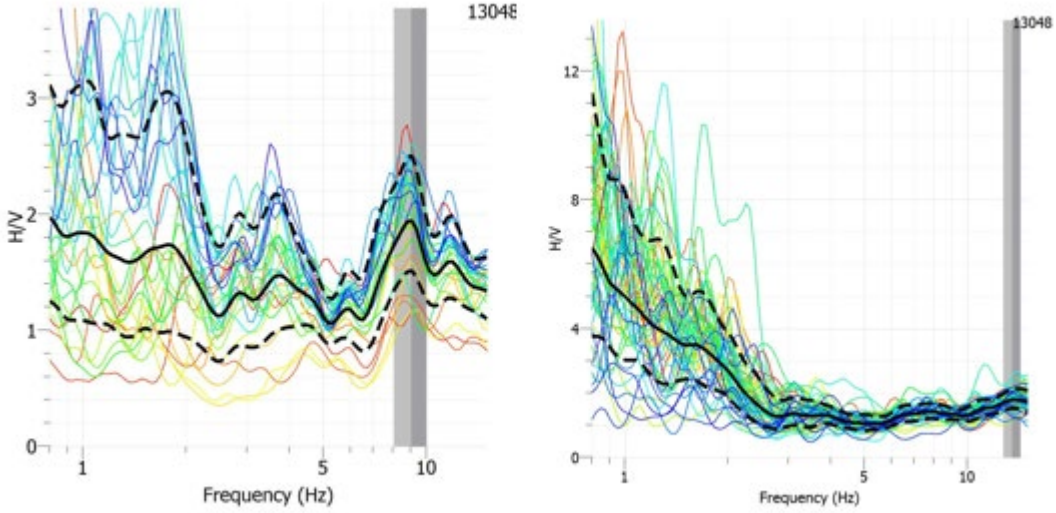

Figure A.9. HVSR curves collected on 2/27/2019. Curves were generated using Geopsy. Grey bars indicate peak frequency and the corresponding standard deviation. The solid black line represents the average curve while the dashed lines represent the standard deviation of that curve.

APPENDIX B: GPR PROFILES

Although the GPR method was not effective in making useful determinations about the subsurface properties relevant to this study the raw data is provided below. Profile length required the cutting of the profiles into multiple pieces for easier viewing. Sections are stacked in groups to save space while single or odd sections are captioned and provided below on their own. Profiles were viewed and extracted in RADAN.

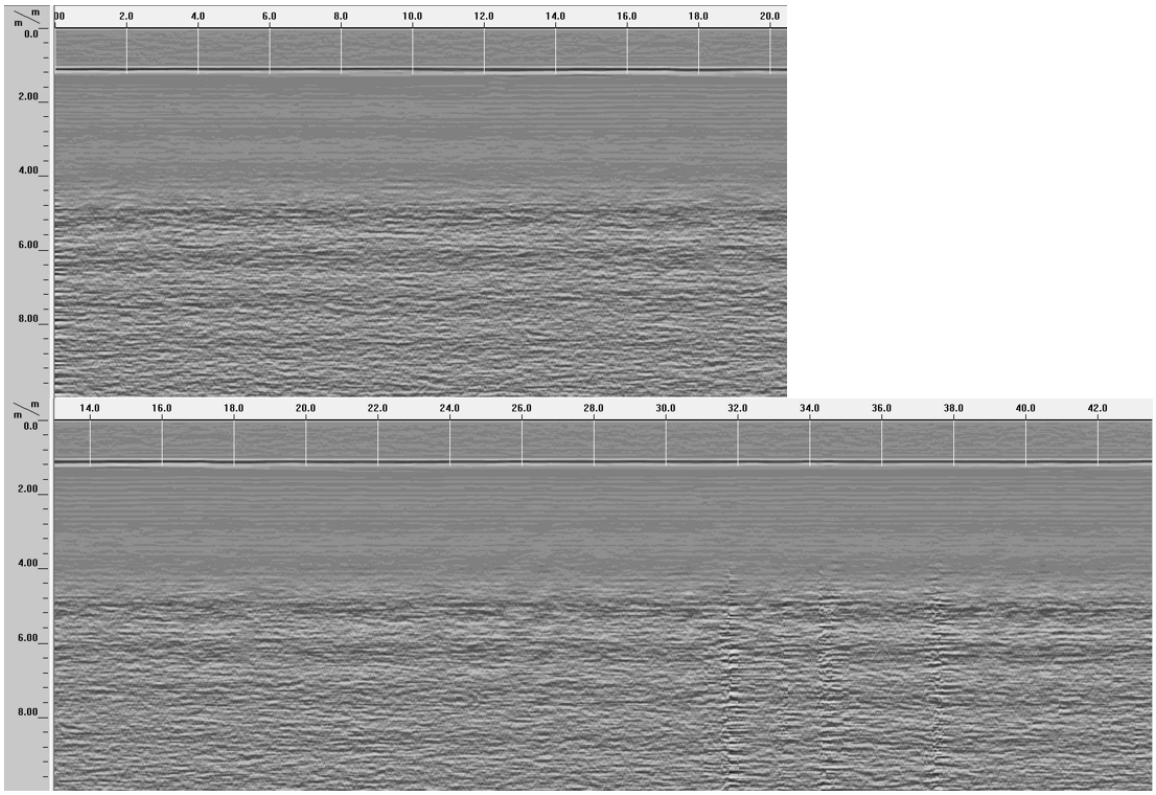

Figure B.1. Combined snippets of one of 18 GPR profiles. Lateral distance displayed is overlapped within each snippet. The entire line in one piece is not shown due to line length and resolution in document. A to A' is shown above.

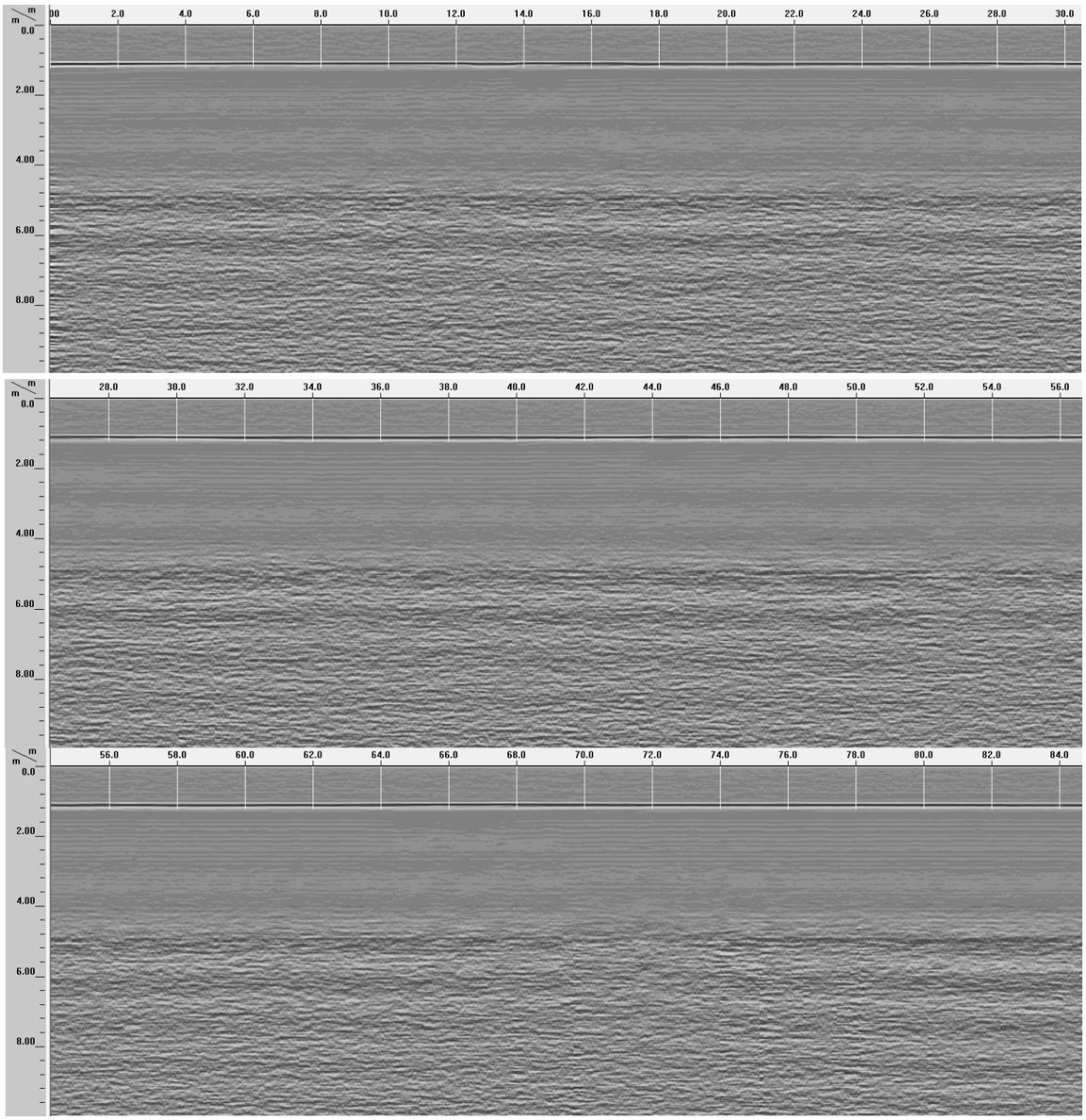

Figure B.2. Combined snippets of one of 18 GPR profiles. Lateral distance displayed is overlapped within each snippet. The entire line in one piece is not shown due to line length and resolution in document. Sections of B to B' are shown above.

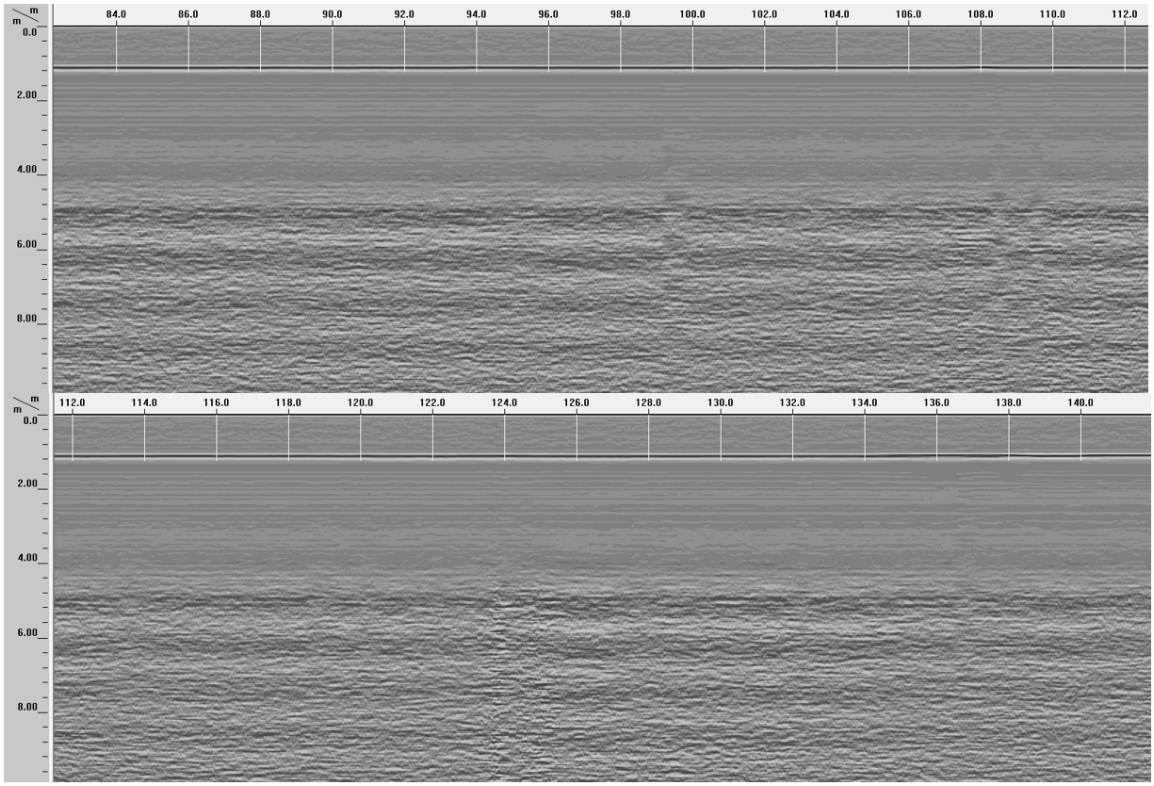

Figure B.3. Combined snippets of one of 18 GPR profiles. Lateral distance displayed is overlapped within each snippet. The entire line in one piece is not shown due to line length and resolution in document. Sections of B to B' are shown above.

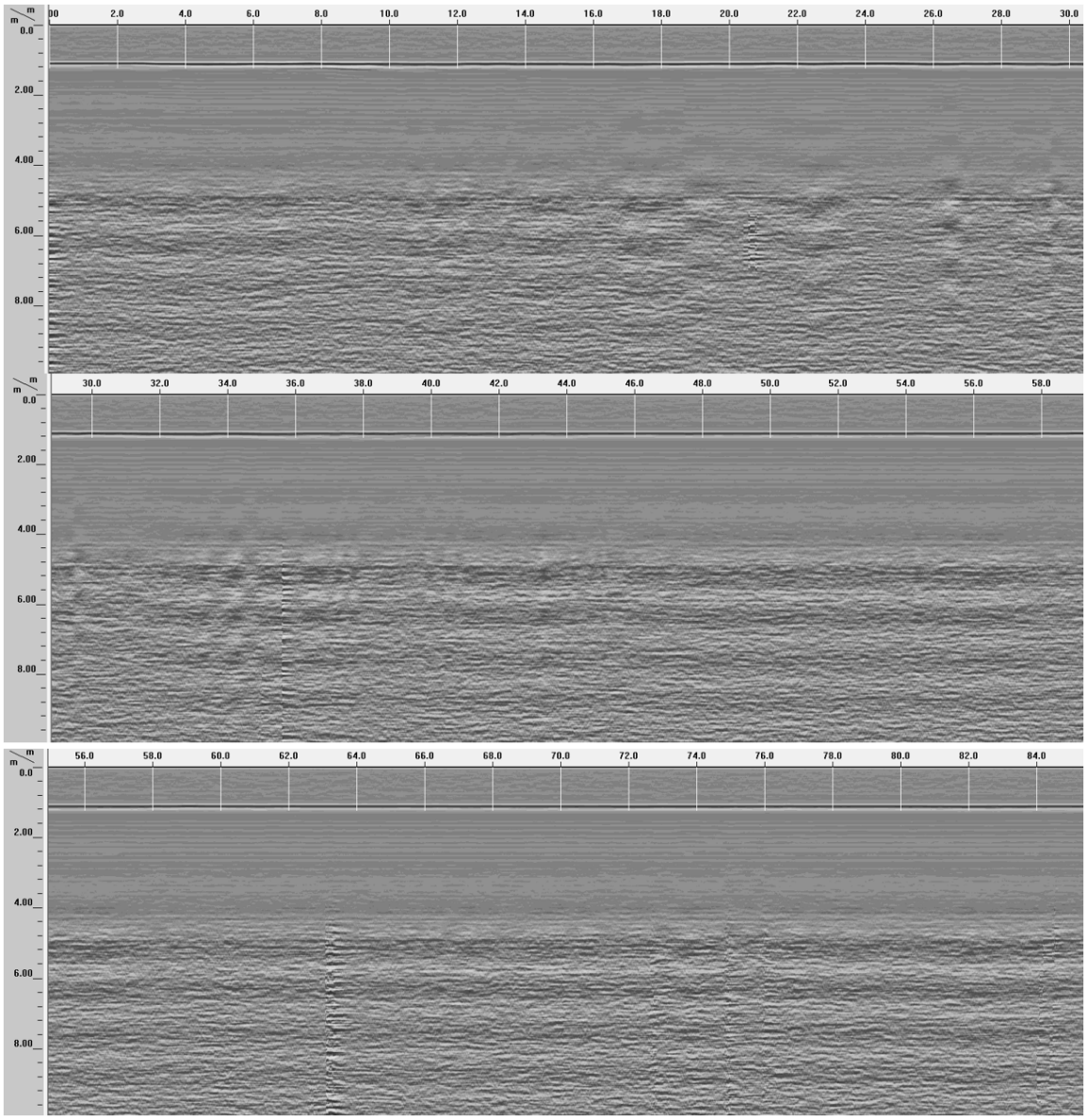

Figure B.4. Combined snippets of one of 18 GPR profiles. Lateral distance displayed is overlapped within each snippet. The entire line in one piece is not shown due to line length and resolution in document. Sections of C to C' are shown above.

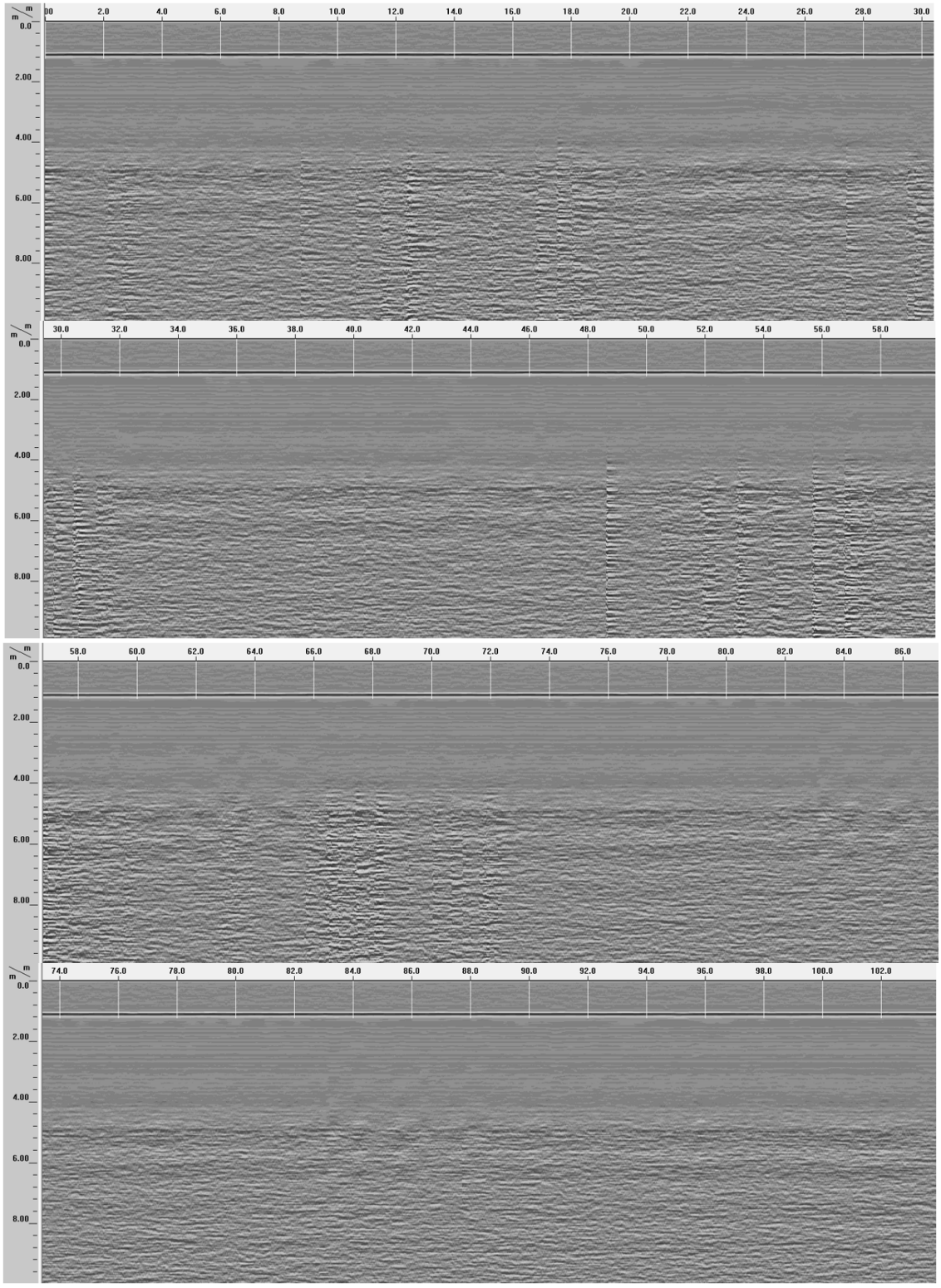

Figure B.5. Combined snippets of one of 18 GPR profiles. Lateral distance displayed is overlapped within each snippet. The entire line in one piece is not shown due to line length and resolution in document. Sections of D to D' are shown above.

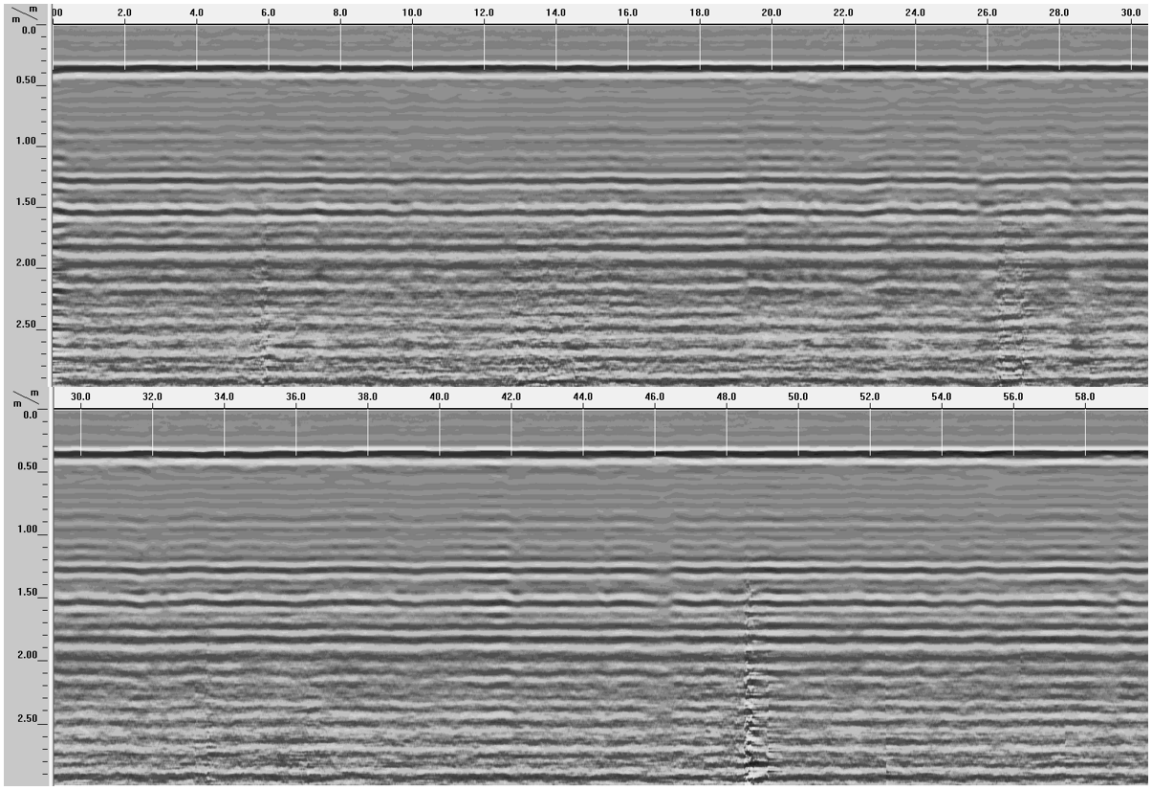

Figure B.6 Combined snippets of one of 18 GPR profiles. Lateral distance displayed is overlapped within each snippet. The entire line in one piece is not shown due to line length and resolution in document. Sections of E to E' are shown above.

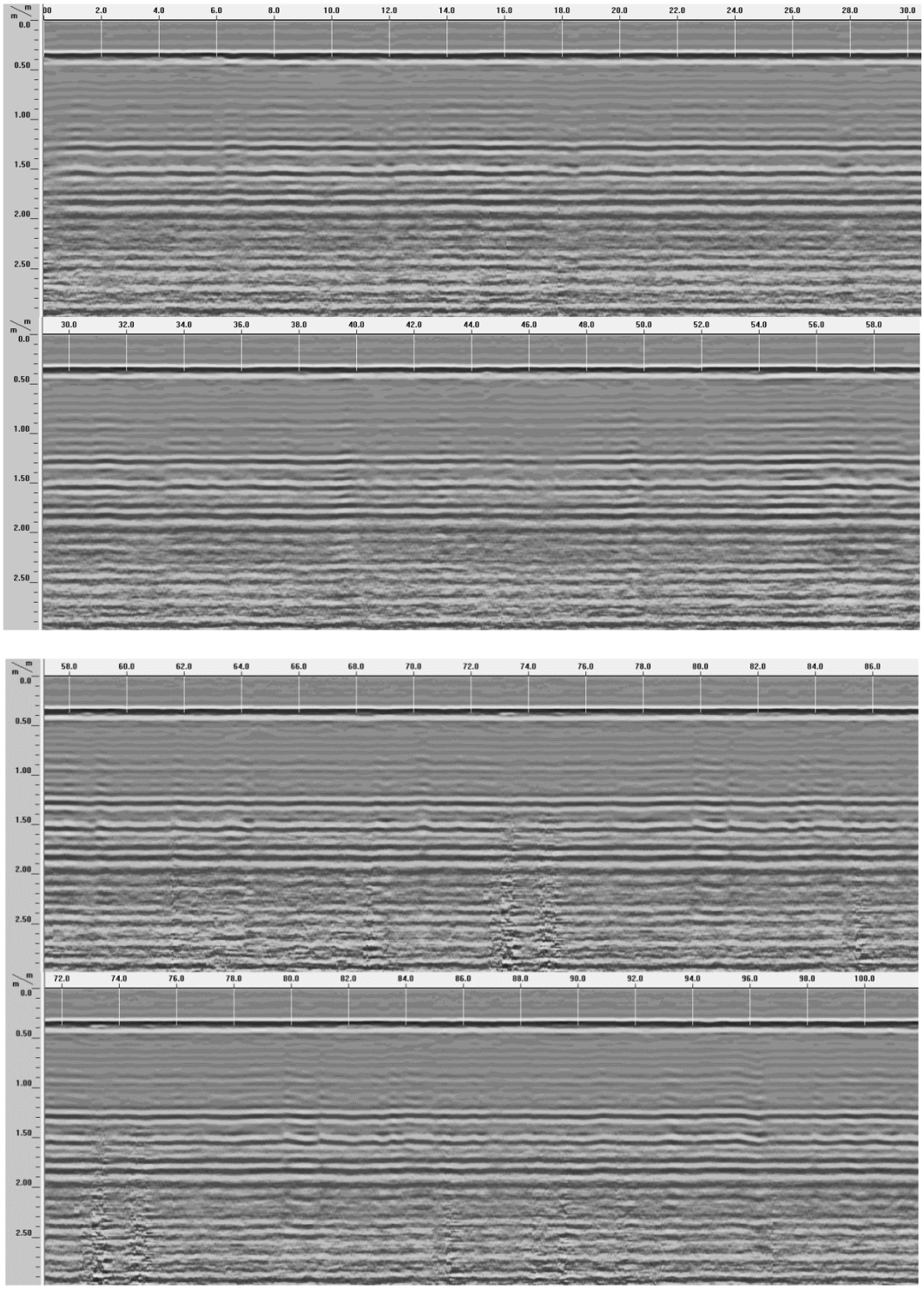

Figure B.7 Combined snippets of one of 18 GPR profiles. Lateral distance displayed is overlapped within each snippet. The entire line in one piece is not shown due to line length and resolution in document. Sections of F to F' are shown above.

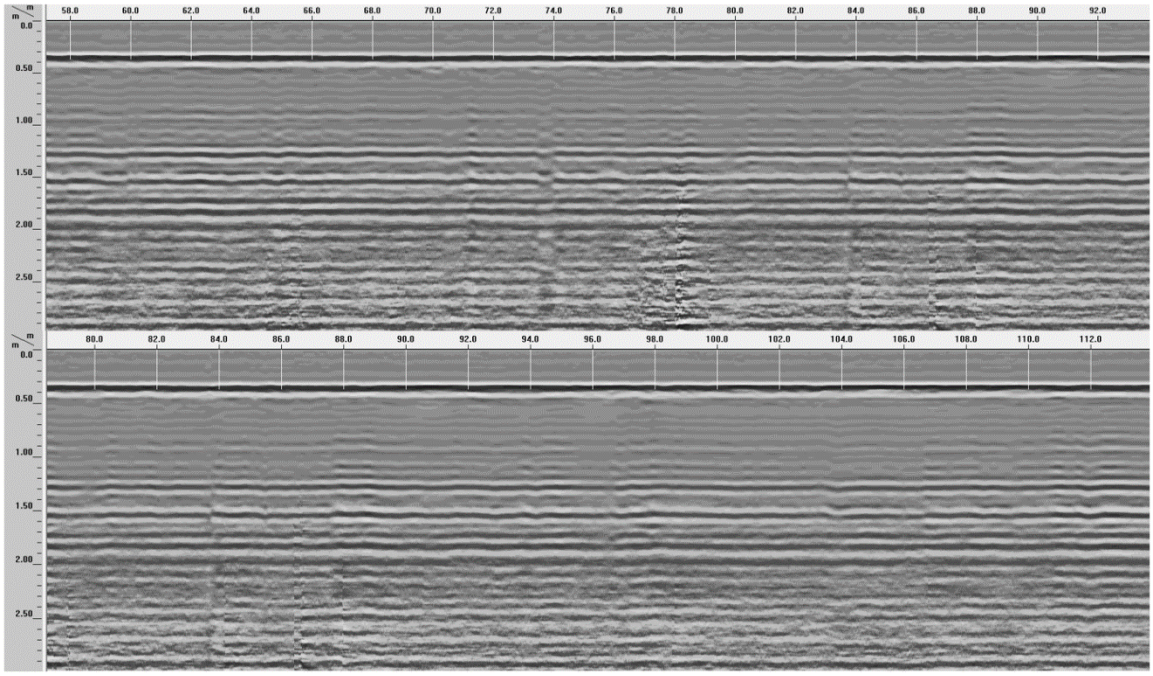

Figure B.8. Combined snippets of one of 18 GPR profiles. Lateral distance displayed is overlapped within each snippet. The entire line in one piece is not shown due to line length and resolution in document. Sections of F to F' are shown above.

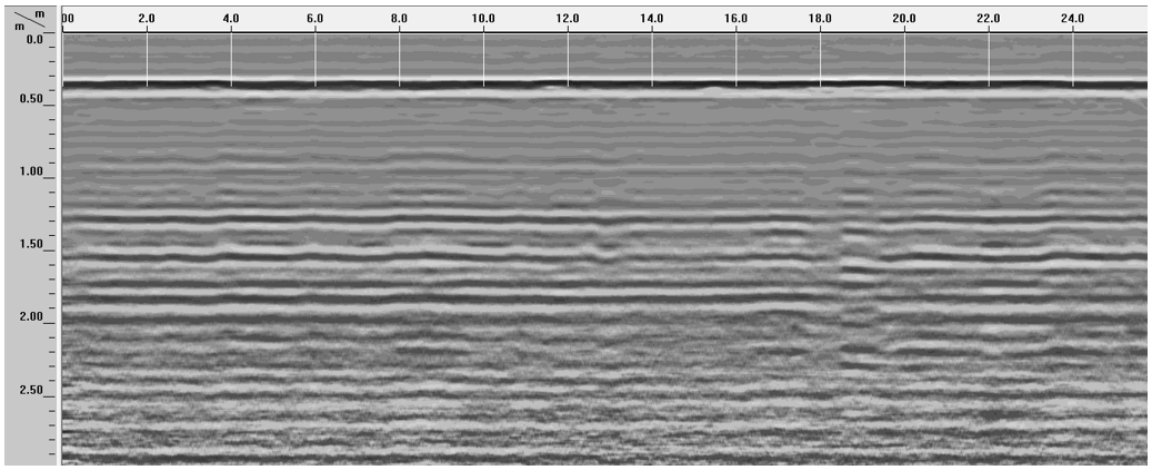

Figure B.9. Combined snippets of one of 18 GPR profiles. Lateral distance displayed is overlapped within each snippet. G-G' is shown above.

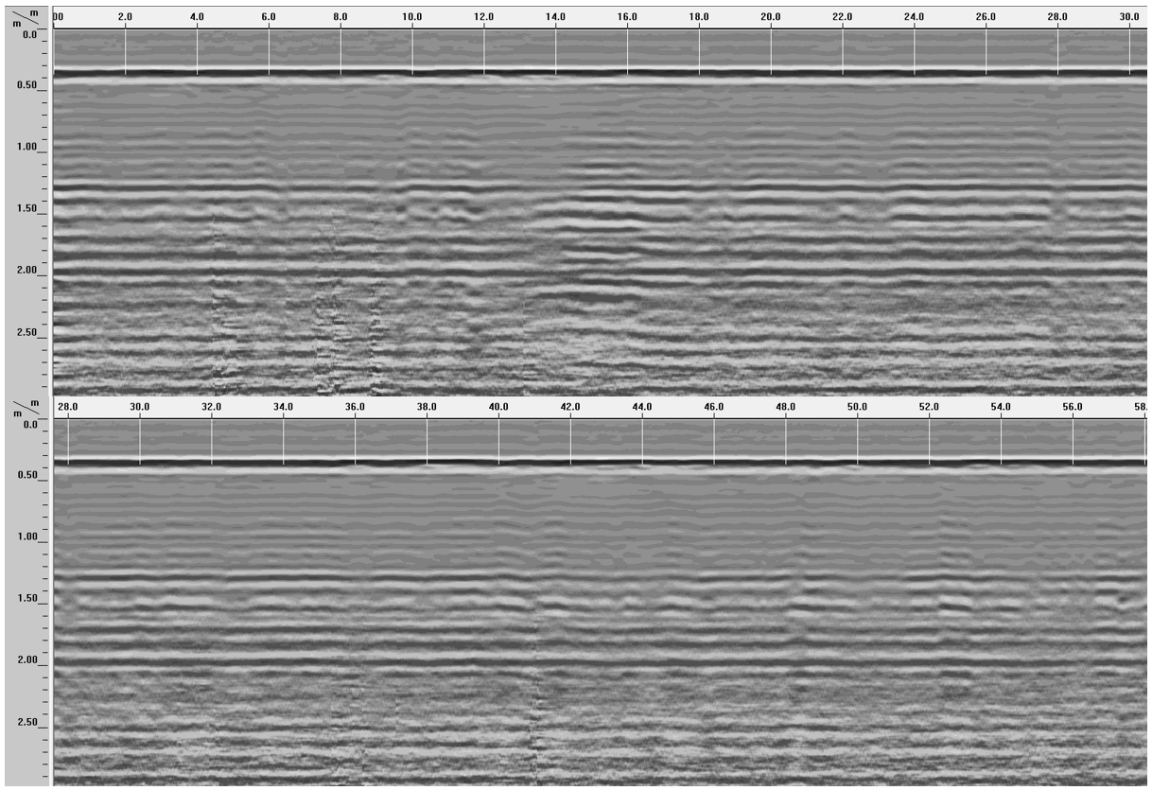

Figure B.10. Combined snippets of one of 18 GPR profiles. Lateral distance displayed is overlapped within each snippet. H to H' is shown above.

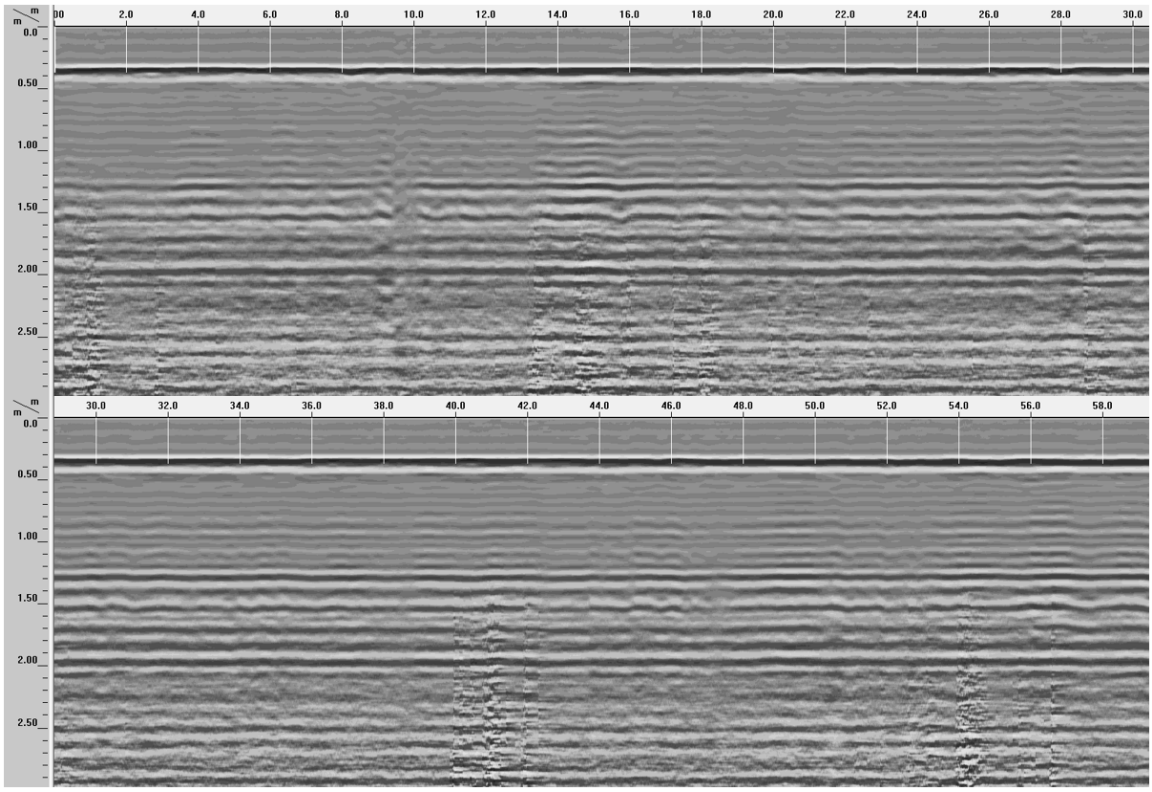

Figure B.11. Combined snippets of one of 18 GPR profiles. Lateral distance displayed is overlapped within each snippet. I to I' is shown above.

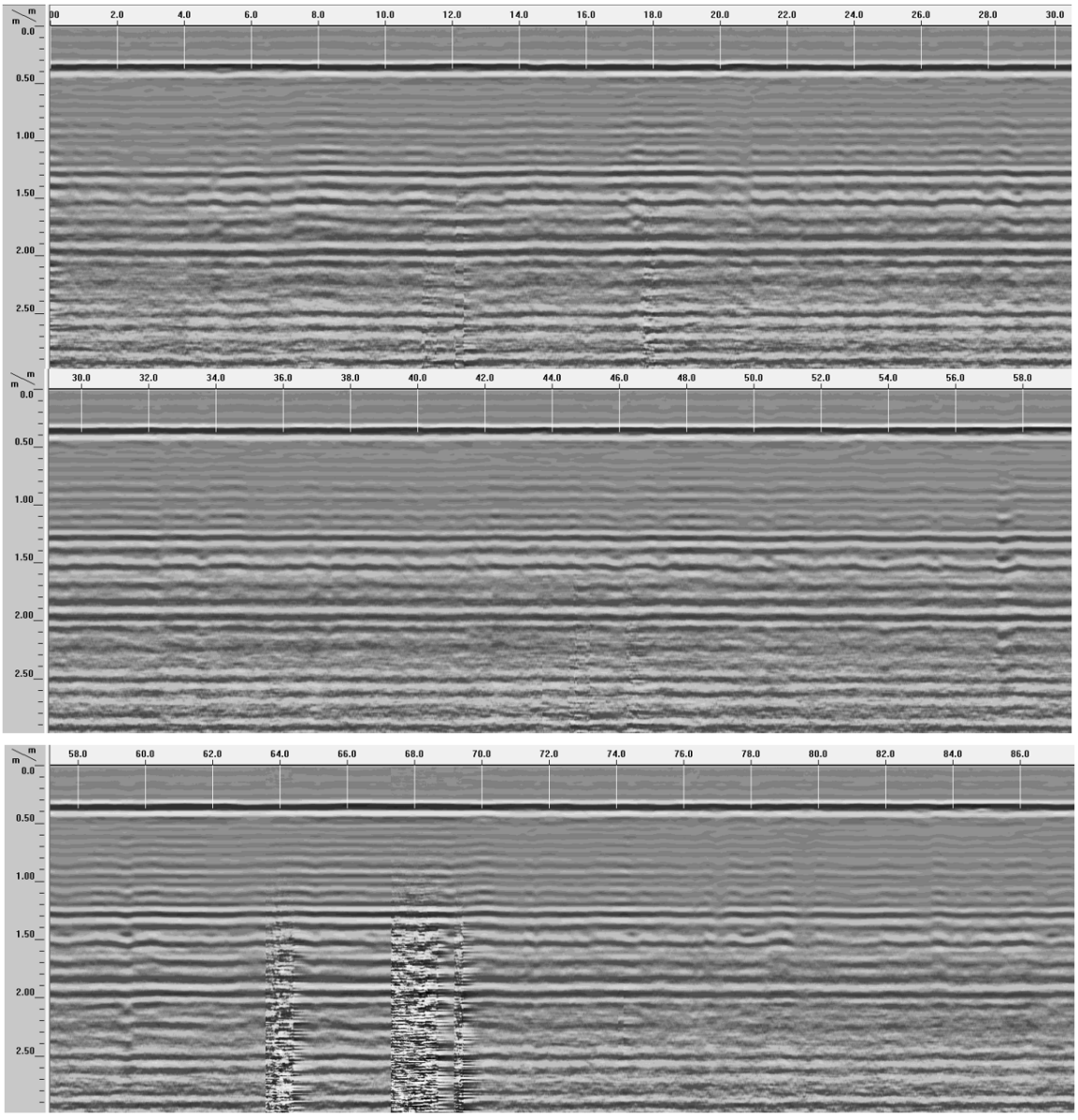

Figure B.12. Combined snippets of one of 18 GPR profiles. Lateral distance displayed is overlapped within each snippet. The entire line in one piece is not shown due to line length and resolution in document. A Section of J to J' is shown above.

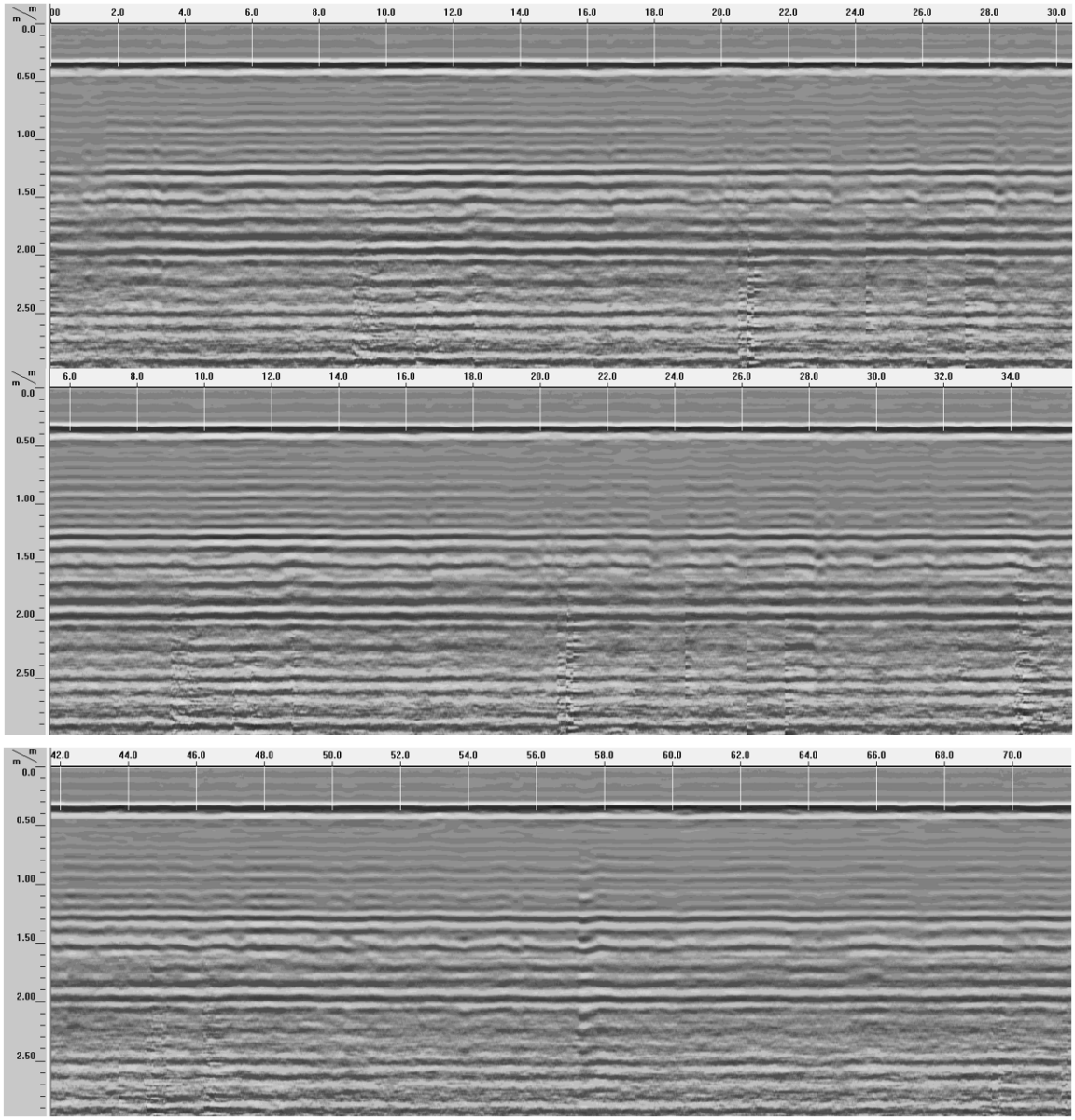

Figure B.13. Combined snippets of one of 18 GPR profiles. Lateral distance displayed is overlapped within each snippet. The entire line in one piece is not shown due to line length and resolution in document. A section of K to K' is shown above.

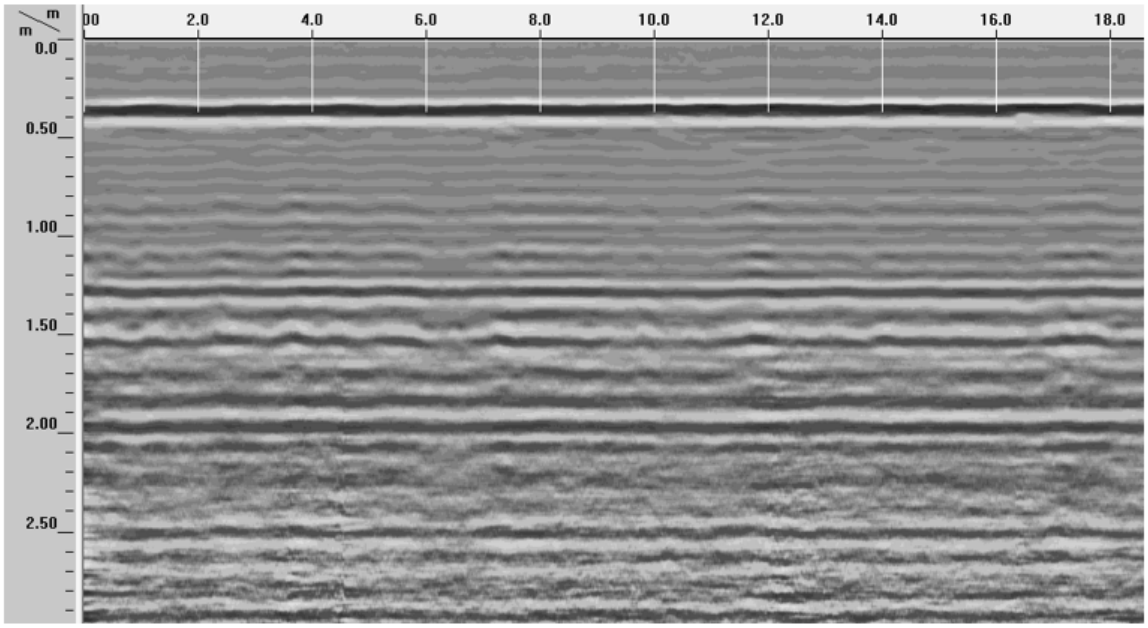

Figure B.14. Snippet of one of the 18 GPR profiles. L to L' is shown above.

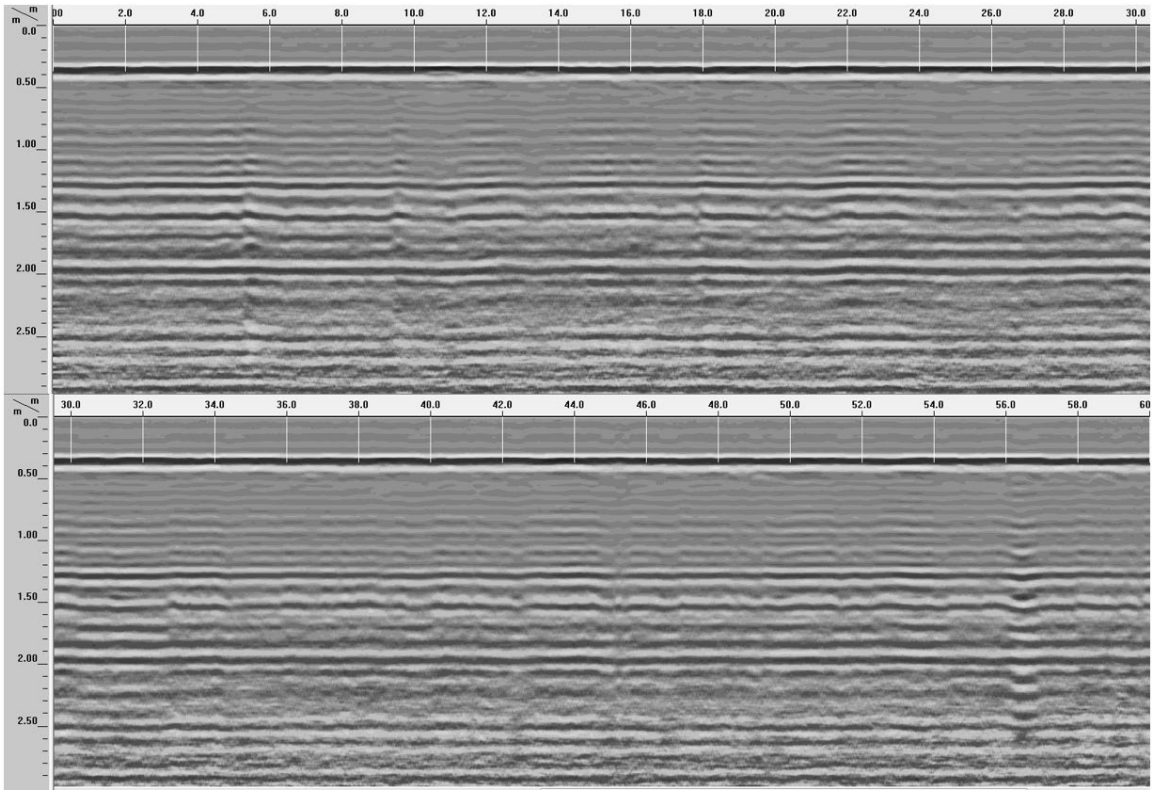

Figure B.15. Combined snippets of one of 18 GPR profiles. Lateral distance displayed is overlapped within each snippet. The entire line in one piece is not shown due to line length and resolution in document. Sections of M to M' are shown above.

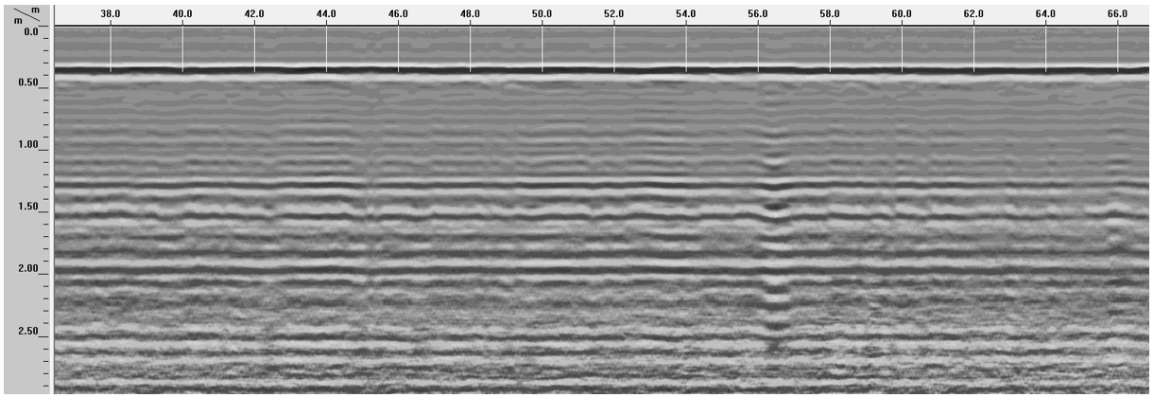

Figure B.16. Combined snippets of one of 18 GPR profiles. Lateral distance displayed is overlapped within each snippet. The entire line in one piece is not shown due to line length and resolution in document. A section of M to M' is shown above.

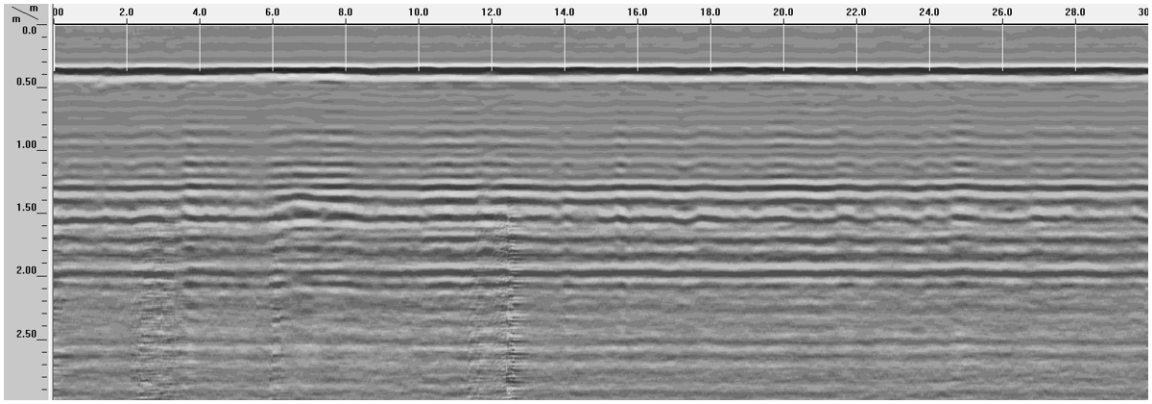

Figure B.17. Combined snippets of one of 18 GPR profiles. Lateral distance displayed is overlapped within each snippet. The entire line in one piece is not shown due to line length and resolution in document. A section of N to N' is shown above.

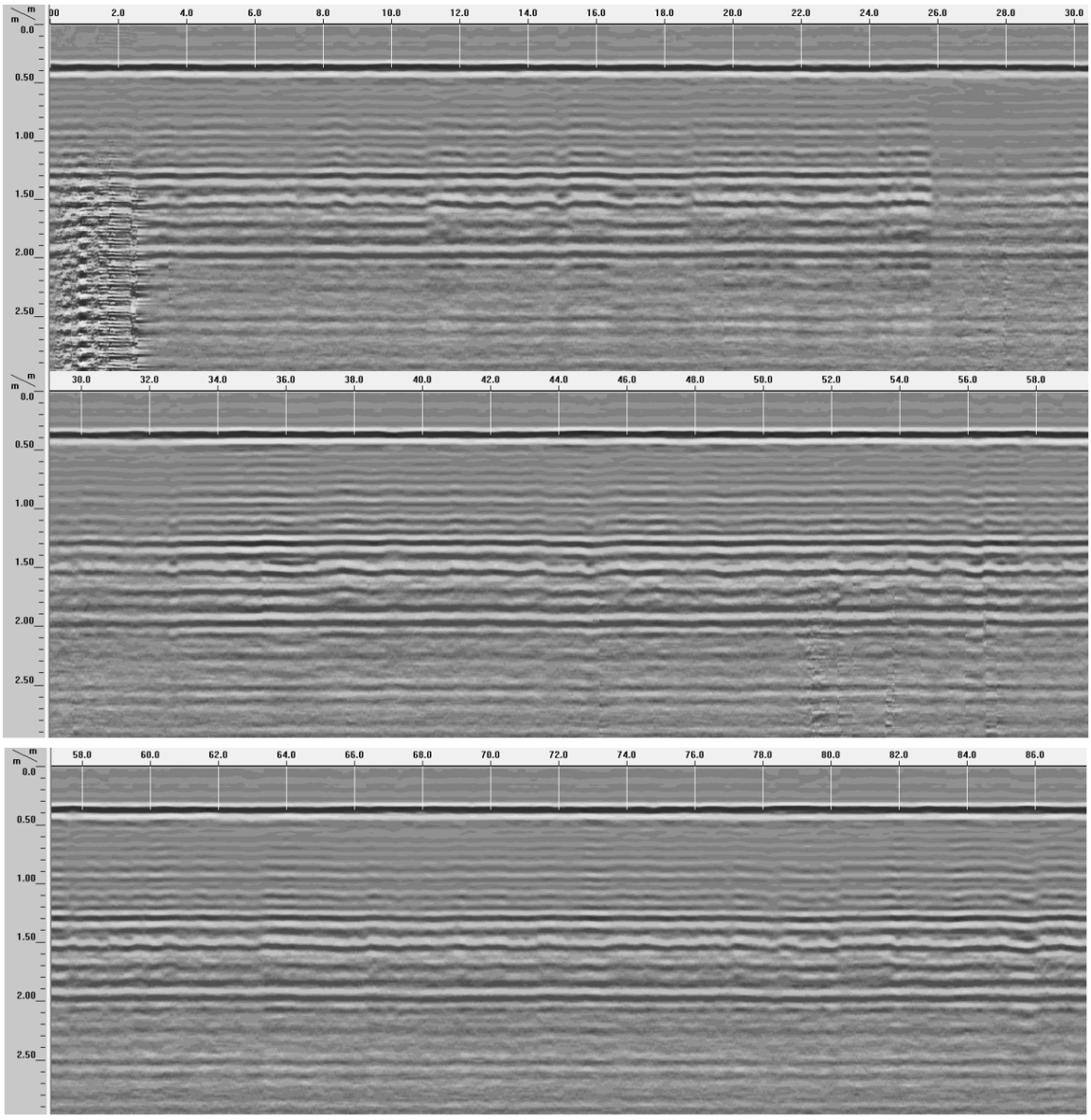

Figure B.18. Combined snippets of one of 18 GPR profiles. Lateral distance displayed is overlapped within each snippet. The entire line in one piece is not shown due to line length and resolution in document. A section of O to O' is shown above.

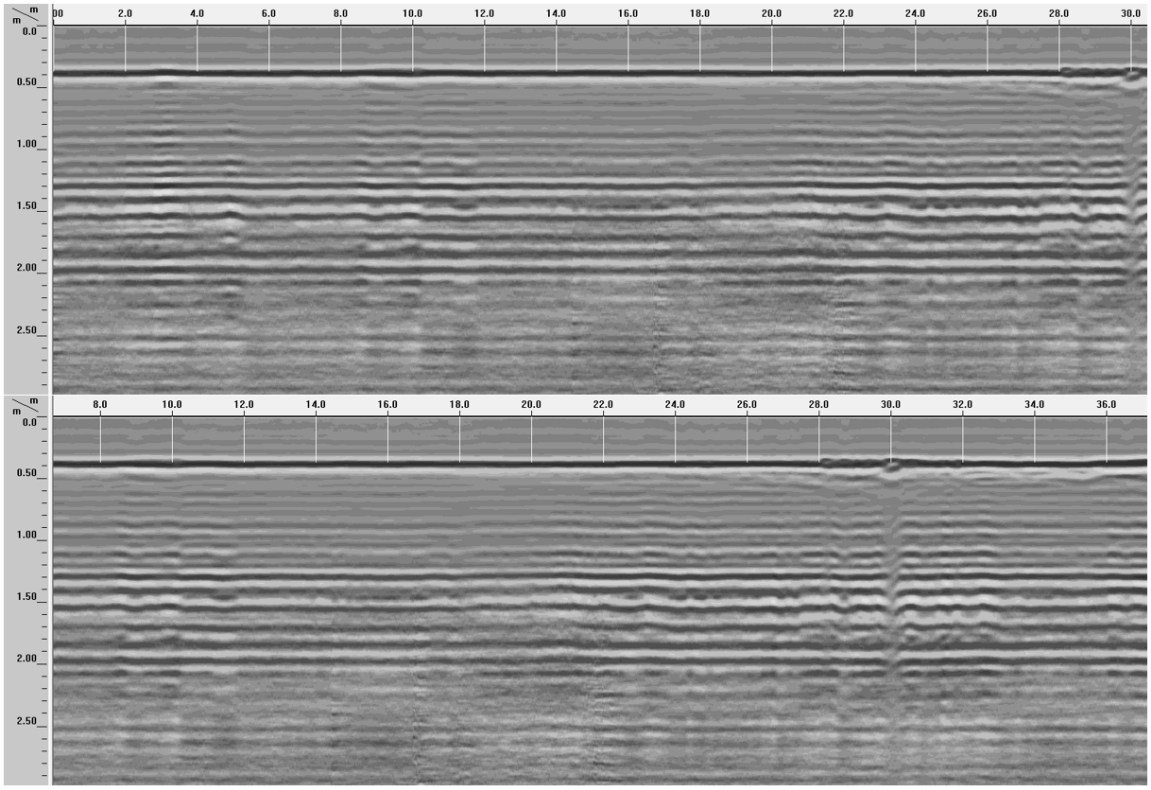

Figure B.19. Combined snippets of one of 18 GPR profiles. Lateral distance displayed is overlapped within each snippet. The entire line in one piece is not shown due to line length and resolution in document. Sections of P to P' are shown above.

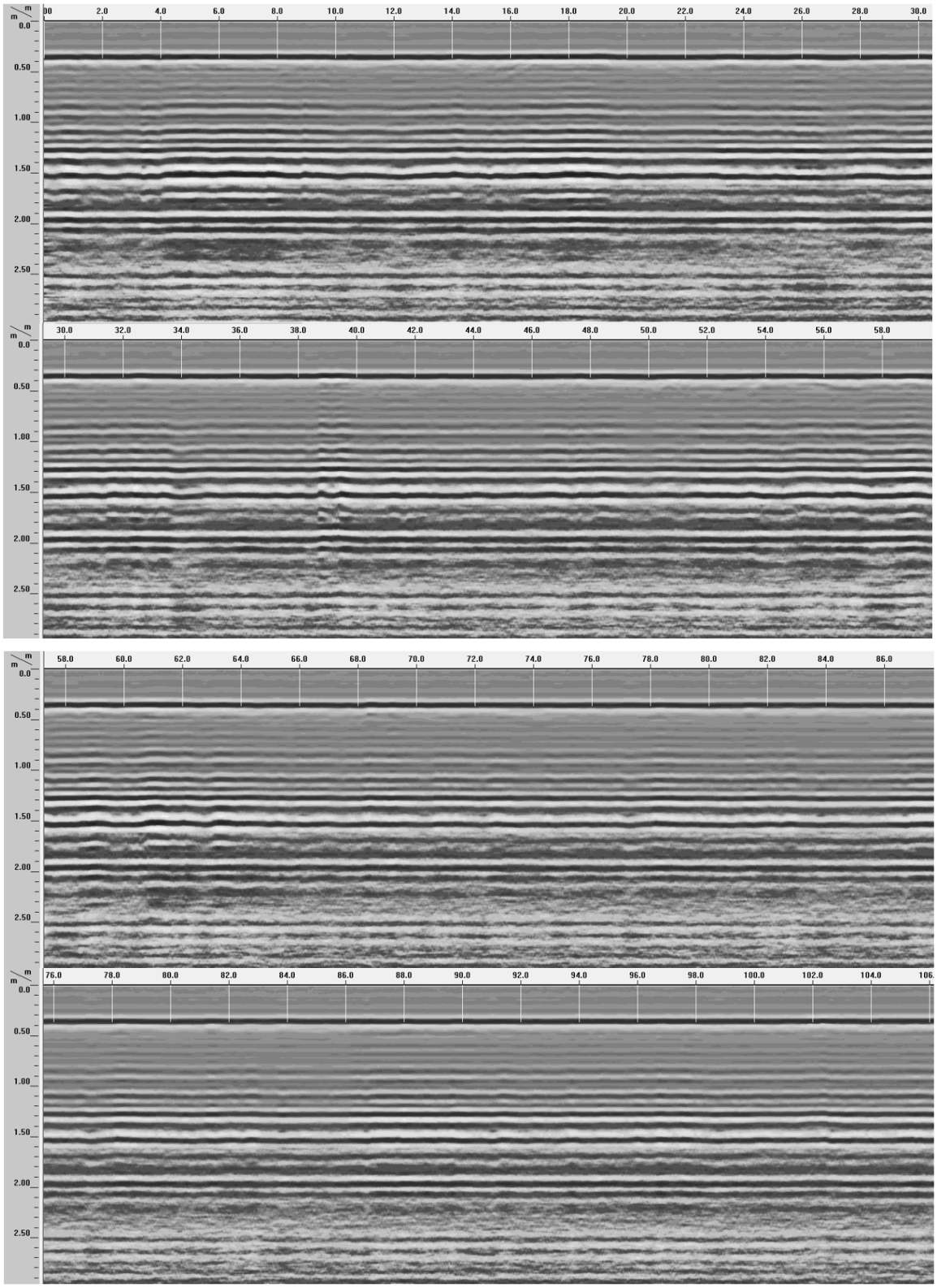

Figure B.20. Combined snippets of one of 18 GPR profiles. Lateral distance displayed is overlapped within each snippet. The entire line in one piece is not shown due to line length and resolution in document. Sections of Q to Q' are shown above.

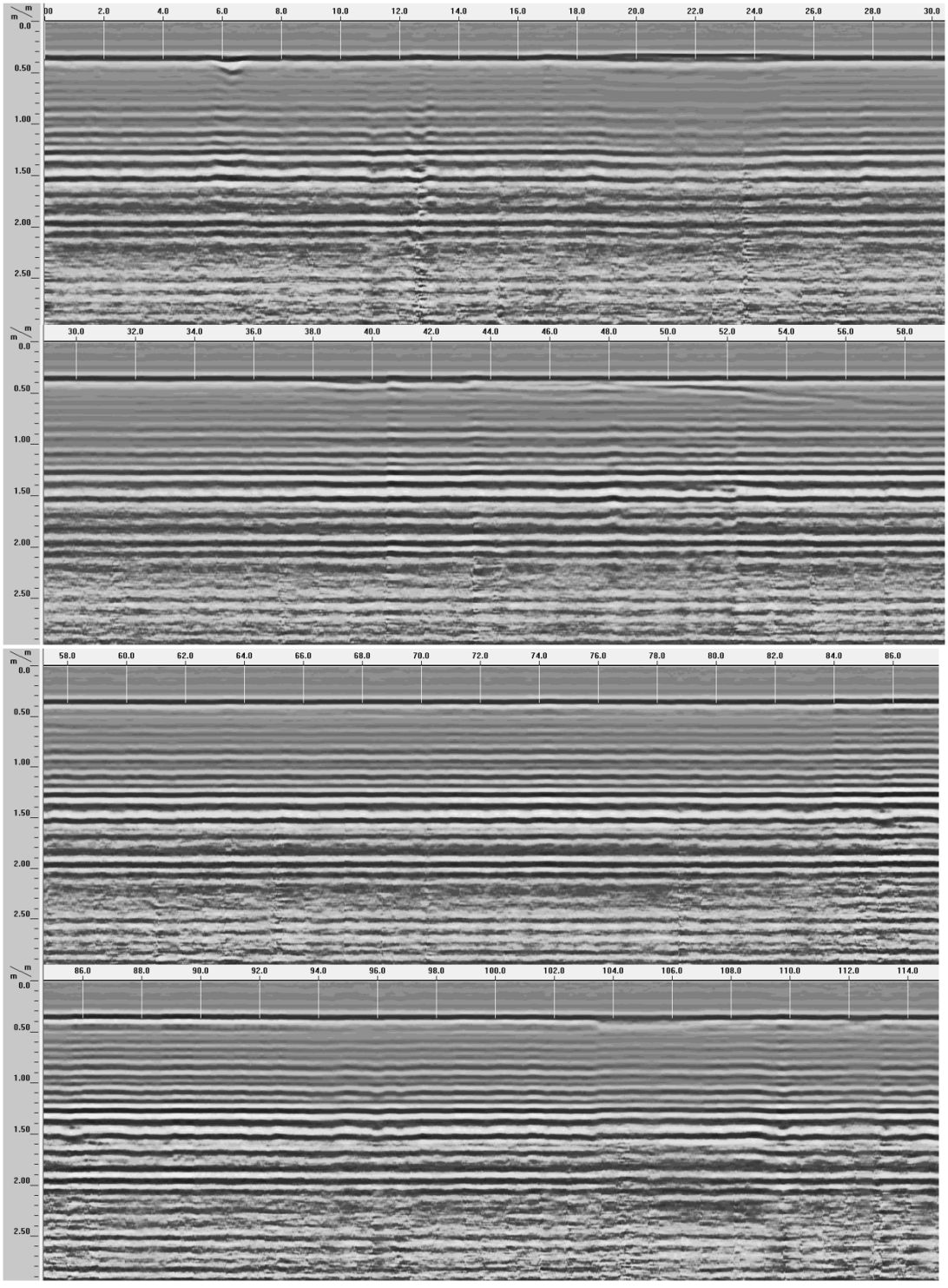

Figure B.21. Combined snippets of one of 18 GPR profiles. Lateral distance displayed is overlapped within each snippet. The entire line in one piece is not shown due to line length and resolution in document. Sections of R to R' are shown above.

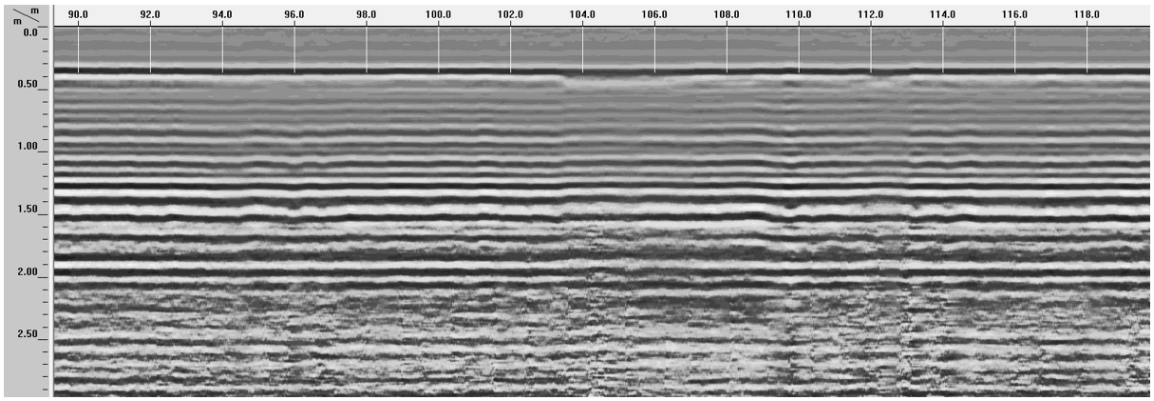

Figure B.22. Combined snippets of one of 18 GPR profiles. Lateral distance displayed is overlapped within each snippet. The entire line in one piece is not shown due to line length and resolution in document. A section of R to R' is shown above.